

Anna-Maija Kärkkäinen

MEMS based voltage references

VTT PUBLICATIONS 613

MEMS based voltage references

Anna-Maija Kärkkäinen

Dissertation for the degree of Doctor of Philosophy to be presented with due permission of the Department of Electrical and Communications Engineering for public examination and debate in the Large Seminar Hall of Micronova (Tietotie 3) at Helsinki University of Technology (Espoo, Finland) on the 3rd of November, 2006, at 12 o'clock noon.



ISBN 951-38-6859-1 (soft back ed.)

ISSN 1235-0621 (soft back ed.)

ISBN 951-38-6860-5 (URL: <http://www.vtt.fi/inf/pdf/>)

ISSN 1455-0849 (URL: <http://www.vtt.fi/inf/pdf/>)

Copyright © VTT Technical Research Centre of Finland 2006

JULKAISIJA – UTGIVARE – PUBLISHER

VTT, Vuorimiehentie 3, PL 1000, 02044 VTT
puh. vaihde 020 722 111, faksi 020 722 4374

VTT, Bergsmansvägen 3, PB 1000, 02044 VTT
tel. växel 020 722 111, fax 020 722 4374

VTT Technical Research Centre of Finland, Vuorimiehentie 3, P.O. Box 1000, FI-02044 VTT, Finland
phone internat. +358 20 722 111, fax +358 20 722 4374

VTT, Tietotie 3, PL 1000, 02044 VTT
puh. vaihde 020 722 111, faksi 020 722 7012

VTT, Datavägen 3, PB 1000, 02044 VTT
tel. växel 020 722 111, fax 020 722 7012

VTT Technical Research Centre of Finland, Tietotie 3, P.O. Box 1000, FI-02044 VTT, Finland
phone internat. +358 20 722 111, fax +358 20 722 7012

Technical editing Maini Manninen

Editia Prima Oy, Helsinki 2006

Kärkkäinen, Anna-Maija. MEMS based voltage references [MEMSiin perustuvat jännite-referenssit]. Espoo 2006. VTT Publications 613. 109 p. + app. 42 p.

Keywords MEMS, micro electromechanical systems, DC voltage reference, AC voltage reference, electrostatic charging, pull-in voltage, long-term stability, micromachining

Abstract

Voltage references are fundamental building blocks in many instruments like data logging systems, digital multimeters, and calibrators. State-of-the-art DC voltage references are large and expensive Josephson voltage standards, operated at cryogenic temperatures. On the other hand, small and affordable Zener diodes are noisy and require temperature compensation, so there is a gap to be filled between these devices. The situation regarding AC voltage references is even worse. There are no references fundamentally based on AC, beside the AC Josephson voltage standard. Usually AC references are based on generating an AC voltage from DC, and respectively, an AC voltage is measured by converting it to DC. Hence, a small and affordable MEMS based AC voltage reference would be a very unique device.

The excellent mechanical properties of silicon microelectromechanical systems (MEMS) have been demonstrated in many commercial applications. Currently the performance of the components is limited by electrostatic instability phenomena and mechanical stress effects arising from component mounting and packaging. However, when these problems are solved, new application areas open up for micromechanical components, for example, in voltage metrology. The stability of a MEMS based voltage reference is ultimately based on mechanical properties of one of the most stable materials: single crystal silicon.

This dissertation reports a DC voltage reference and an AC voltage reference based on the pull-in voltage, a characteristic property of an electrostatic MEMS component. First a brief introduction to voltage metrology and MEMS is given, then methods available for making MEMS based voltage references are discussed, and finally results are presented. The results are divided into three Sections: design and manufacturing of the components, readout electronics, and measurement results of the reference long-term stability.

The stability of the reference voltage is of major importance in metrological applications and it is studied both theoretically and experimentally in this work. A detailed analysis of the electromechanical coupling of MEMS components is presented. Due to the lack of an appropriate text book, a majority of the formulas are derived from the basic equations by the author, including also those presented in the Methods Section. Component manufacturing, design and materials choices are also discussed focusing on the stability issue.

In the experimental part of this work a DC voltage reference and an AC voltage reference were designed, manufactured and characterized. Also two MEMS moving plate capacitors were designed: one optimised for use as a DC reference and the other optimised for use as an AC reference. The capacitor electrodes required metallizing which could not be manufactured using the existing processes. Hence a new silicon-on-insulator (SOI) manufacturing process utilising low temperature fusion bonding was developed.

The stability of the AC voltage reference presented in this dissertation is at ppm-level (10^{-6}). This level of performance is sufficient for several applications and outstanding compared to results published earlier for MEMS based voltage references. In the beginning of this work, a slow electrostatic charging effect of the MEMS component was the major factor limiting the device stability. The charging was significantly reduced by using AC voltage (instead of DC) to actuate the component to the pull-in point. However, even in the absence of an external DC voltage, there is an internal DC voltage due to the component built-in voltage. AC voltage actuation together with built-in voltage compensation removed the charging effect in the first order and reduced the drift of the reference below 2 ppm during the three week measurement period. The next challenge is to improve the component mechanical stability including the reduction of the component temperature coefficient. Before commercialisation component mounting and hermetic packaging need further attention as well.

Also, the DC voltage reference showed a significant improvement compared to results published earlier. In addition to the actions mentioned above, the DC voltage reference would still require improvement in the feedback electronics.

Kärkkäinen, Anna-Maija. MEMS based voltage references [MEMSiin perustuvat jännitereferenssit]. Espoo 2006. VTT Publications 613. 109 s. + liitt. 42 s.

Avainsanat MEMS, micro electromechanical systems, DC voltage reference, AC voltage reference, electrostatic charging, pull-in voltage, long-term stability, micromachining

Tiivistelmä

Mikroelektromekaanisiin systeemeihin, eli MEMSiin, perustuvat jännitereferenssit ovat ainutlaatuisia sekä ominaisuuksiltaan että toimintaperiaatteeltaan. Ne ovat pieniä ja tarkkoja, ja niillä on hyvä hinta-laatusuhde. Referenssin toiminta perustuu mikromekaanisesti valmistettuun levykondensaattoriin, jonka toinen levy on ripustettu piijousien varaan. Levyjen väliin kytketty jännite pyrkii lähentämään levyjä toisiinsa, kun taas piijousi vastustaa tätä liikettä. Voimatasapainoa levyjen välillä voidaan kuvata massa-jousi-vaimennin-mallilla ja sillä on kaksi keskeistä ominaisuutta. Sähköstaattinen voima levyjen välillä on verrannollinen jännitteen neliöön, eli sitä voidaan käyttää todellisena tehollisarvomuuntimena. Lisäksi kondensaattorin ulostulojännitteellä on maksimi, jota voidaan käyttää stabiilina jännitereferenssinä, sillä sen arvo riippuu vain yksikiteisen piin materiaalivakiosta ja jousen geometriasta. Koska referenssi-jännite on samalla myös käännealue, ohjauksjännitteen pienet vaihtelut eivät vaikuta referenssi-jännitteen arvoon ensimmäisessä kertaluvussa. Näiden ominaisuuksien ansiosta MEMS-jännitereferenssit tulevat haastamaan olemassa olevat jännitereferenssit, esimerkiksi Zenerdiodit.

Väitöskirjassa tutkitaan sekä teoreettisesti että kokeellisesti kahta jännitereferenssiä, joista toinen on suunniteltu tasajännitteelle ja toinen vaihtojännitteelle. Molemmille suunniteltiin omat MEMS-komponentit. Niiden suunnittelu, valmistus ja ominaisuudet on kuvattu yksityiskohtaisesti samoin kuin referenssien lukuelektroniikat ja valmiiden laitteiden ominaisuudet. Erityisesti huomiota on kiinnitetty referenssien sähköiseen stabilisuuteen, joka on myös nykyisin kaupallisessa tuotannossa olevien MEMS-komponenttien ongelma. Väitöstyön merkittävin saavutus on MEMS-komponenttien sähköisen stabiilisuuden parantaminen tasolle, joka mahdollistaa niiden hyödyntämisen vaativissa metrologisissa sovelluksissa. Näitä innovaatioita, samoin kuin työssä kehitettyä uutta valmistusmenetelmää, voidaan geneerisesti hyödyntää myös muihin MEMS-sovelluksiin.

Preface

The research work covered by this dissertation has been carried out at VTT Information Technology MEMS sensors group (former VTT Automation, Measurement technology group) during 2001–2005. The research work was mainly done within the EMMA project (ElectroMechanical Microcomponents for precision Applications) funded by the EU IST programme and by the Technology Development Centre of Finland (Tekes). The work has been done in close collaboration with the co-workers in the MEMS sensors group, the Centre for Metrology and Accreditation (MIKES) and VTI Technologies Oy. Also other EMMA partners Fluke P.M, Twente University, NMi – Van Swinden Laboratorium, and Physikalisch-Technische Bundesanstalt (PTB) are acknowledged.

First of all, I thank Professor Heikki Seppä and Research Professor Aarne Oja for the challenging research topic and guidance in the work. In addition Aarne Oja has instructed the dissertation work which has been a pleasure to me. Also, I wish to thank my supervisor, Professor Ilkka Tittonen from the Helsinki University of Technology for his advice as well as Professor Heli Jantunen and Professor Jukka Leikkala for carefully pre-examining the manuscript.

I thank Heikki Kuisma from VTI Technologies Oy for providing test components and helpful discussions (since 1986, when I joined the legendary MEMS group at Vaisala Oyj). I thank all my co-authors at VTT, MIKES, VTI Technologies Ltd., and NPL for good collaboration: Jukka Kynnäräinen, Nadine Pesonen, Panu Pekko, James Dekker, Mika Suhonen, Antti Manninen, Nikolai Tisnek, Shakil Awan and the previously mentioned names above. Particularly the collaboration with Jukka Kynnäräinen and Nadine Pesonen has been very inspiring and helpful to me. I have also greatly benefited from the help of other members in the MEMS sensor group Teuvo Sillanpää, Ville Kaajakari, Tomi Mattila, and Paula Holmström and other members of the Microsensing group. I thank Jari J. Penttilä and Ari Häärä for their technical assistance. Also, Seija Lepistö, Aija Kaski and Kaisa Falenius are acknowledged.

Finally, I would like to thank my family and friends for their support and bringing so much love and joy in my life.

Contents

Abstract	3
Tiivistelmä	5
Preface	6
List of acronyms and symbols	10
List of publications	13
Author's contribution	14
1. Introduction	15
1.1 MEMS	15
1.2 Voltage metrology	16
1.3 DC voltage references	17
1.3.1 Josephson voltage reference	18
1.3.2 Zener diodes	18
1.3.2.1 Principle of operation	18
1.3.2.2 Zener diode characteristics	19
1.3.2.3 IC Zeners	19
1.3.3 Bandgap references	20
1.3.4 Floating gate technology	21
1.4 AC voltage references	22
1.5 MEMS in voltage metrology	22
2. Methods	25
2.1 Electromechanical coupling in MEMS components	25
2.1.1 Static analysis	25
2.1.1.1 Translational mode	25
2.1.1.2 Rotational mode	28
2.1.1.3 DC voltage actuation	31
2.1.1.4 AC current actuation	33
2.1.2 Dynamic analysis	35
2.1.3 Damping	41
2.2 MEMS manufacturing technologies	43

2.2.1	Bulk micromachining.....	43
2.2.2	Surface micromachining	44
2.2.3	SOI	45
2.3	MEMS component.....	45
2.3.1	Component Dimensions	46
2.3.2	Materials choices.....	46
2.3.2.1	Single-crystal silicon.....	46
2.3.2.2	Polysilicon	47
2.3.2.3	Silicon oxide and silicon nitride	48
2.3.2.4	Metals	48
2.3.3	Parasitic capacitance	49
2.3.4	Packaging.....	49
2.4	VTI accelerometer	50
2.5	Stability of a MEMS component.....	51
2.5.1	Component structure	52
2.5.2	Built-in voltage.....	53
2.5.3	Depletion layer capacitance	56
2.5.4	Electrostatic charging.....	59
2.5.4.1	Charges in dielectrics.....	60
2.5.4.2	Oxide charging models	63
2.5.5	Mechanical stability	64
3.	Manufacturing and design of the components	66
3.1	EMMA Process	66
3.2	Component for the DC voltage reference.....	68
3.2.1	Geometry.....	68
3.2.2	Eigencurve	69
3.2.3	FEM simulations	70
	Calculation parameters	71
3.2.4	Resonance frequency	72
3.2.5	Electrodes.....	73
3.2.6	Component characteristics	74
3.3	Component for the AC voltage reference.....	75
3.3.1	Geometry.....	75
3.3.2	Eigencurve	77
3.3.3	FEM simulations	77
3.3.4	Electrodes.....	80

3.3.5	Component characteristics	81
3.4	Stability of the component.....	81
3.4.1	Electrical stability.....	82
3.4.2	Packaging	83
3.4.3	Stability against changes in the environmental conditions	84
3.4.3.1	Temperature	85
3.4.3.2	Humidity	86
3.4.3.3	Gravity	87
4.	Readout electronics.....	88
4.1	DC voltage reference	88
4.2	AC reference electronics	93
5.	Measurement results	95
5.1	Stability of the DC voltage reference	95
5.2	Drift of the AC reference voltage	96
5.3	Built-in voltage compensation.....	98
5.4	Stability of the AC voltage reference	99
6.	Conclusions.....	102
	References.....	104

Appendices:

 Publications I–V

*Appendix V of this publication is not included in the PDF version.
Please order the printed version to get the complete publication
(<http://www.vtt.fi/publications/index.jsp>)*

List of acronyms and symbols

ABS	Antilock Braking system
AC	Alternating current
CMOS	Complementary metal-oxide semiconductor
DC	Direct current
DIL	Dual in-line package
DMM	Digital multimeter
DRIE	Deep reactive ion etch
DVM	Digital volt meter
C-V	Capacitance vs. voltage (curve)
C4	Controlled Collapse Chip Connection technology (flip-chip)
emf	electromotive force
EDP	Ethylene diamine pyrocatechol, anisotropic silicon wet etchant
ESP	Electronic Stability Program
FGA	Floating gate analog technology
IC	Integrated circuit
JVS	Josephson voltage standard
KOH	Potassium hydroxide, anisotropic silicon wet etchant
LIGA	Litographie galvanofornung, abformung
LPCVD	Low pressure chemical vapour deposition
LTCC	Low temperature co-fired ceramic
MEMS	Microelectromechanical system
MOSFET	Metal oxide semiconductor field effect transistor
MST	Microsystem technology
NBTI	Negative bias temperature instability
PCB	Printed circuit board
PECVD	Plasma exchanged chemical vapour deposition
PID	Proportional, plus integral, plus derivative controller

PMJTC	Planar multijunction thermal converter
ppm	Parts per million
RMS	Root mean square
RF	Radio frequency
SD	Sputter deposition
SI	System of units
SOI	Silicon on insulator
TC	Linear coefficient of thermal expansion
TMAH	Tetramethylammonium hydroxide, anisotropic silicon wet etchant
A	Surface area
C	Capacitance
d	Gap (between a moving and a fixed electrode)
e	Elementary charge
E	Young's modulus
E_e	Electrostatic energy
E_C	Bottom of conduction band
E_F	Fermi energy level
E_V	Top of valence band
f	Frequency
F	Force
g	acceleration
G	Shear modulus
h	Plank constant
I	Current, Moment of inertia
J	Current density
k	Spring constant
k_B	Boltzmann's constant
m	Mass
n	Density of free electrons

N_A	Acceptor density
P	Pressure
p	Density of free holes
q	Charge
Q	Mechanical quality factor
Q_{it}	Interface-trapped charge
Q_f	Fixed oxide charge
R	Resistance
t	Time
T	Temperature, Torque
V	Voltage
V_{bi}	Built-in voltage
V_{pi}	Pull-in voltage
x	Deflection from the rest position
x_d	Extent of the space charge
α	Phase, silicon linear coefficient of thermal expansion
β	Young's modulus linear coefficient of thermal expansion
γ	Diffusion constant
δ_N	Noise displacement
ϵ	Permittivity
ϵ_0	Permittivity in vacuum
κ	Spring torsion coefficient
λ	Damping coefficient
ρ	Density
ρ_s	Space charge density
σ	Surface charge density
τ	Time constant of charging
ϕ	Tilt angle
ω	Angular frequency

List of publications

This dissertation includes the following publications, which are referred to in the text by Roman numerals I–V.

- I. Kärkkäinen, A., Oja, A., Kyynäräinen, J., Kuisma, H. and Seppä, H. Stability of Electrostatic Actuation of MEMS. *Physica Scripta*, Vol. T114, 2004, pp. 193–194.
- II. Kärkkäinen, A., Pekko, P., Dekker, J., Pesonen, N., Suhonen, M., Oja, A., Kyynäräinen, J. and Seppä, H. Stable SOI Micromachined Electrostatic AC Voltage Reference. *Microsystem Technologies*, Vol. 12, Dec. 2005, pp. 169–172.
- III. Kärkkäinen, A., Pesonen, N., Suhonen, M., Oja, A., Manninen, A., Tisnek, N. and Seppä, H. MEMS-Based AC Voltage Reference. *IEEE Transactions on Instrumentation and Measurement*, Vol. 54, Apr. 2005, pp. 595–599.
- IV. Kärkkäinen, A., Awan, S.A., Kyynäräinen, J., Pekko, P., Oja, A. and Seppä, H. Optimized Design and Process for Making a DC Voltage Reference Based on MEMS. *IEEE Transactions on Instrumentation and Measurement*, Vol. 54, Apr. 2005, pp. 563–566.
- V. Kärkkäinen, A., Tisnek, N., Manninen, A., Pesonen, N., Oja, A. and Seppä, H. Electrical stability of a MEMS-based AC voltage reference. Submitted to *Sensors and Actuators A*.

Author's contribution

The results presented in this dissertation are obtained in collaboration with several other persons from VTT and the Centre for Metrology and Accreditation (MIKES). The author has been the main writer in all of the publications I–V. The author has designed both the DC and the AC reference components. All the calculations and simulations related to the components are done by the author except the theoretical AC reference frequency response (Fig. 4) in publication III. Due to the lack of an appropriate text book, a majority of the formulas are derived from the basic equations by the author, including also those presented in the Methods Section. The author has participated in the EMMA process development by defining the targets for the structures and suggested processing methods, but not in the component manufacturing in the clean room. The author has designed the built-in voltage compensation for the AC reference readout electronics. She is also a co-author in the patent application related to that innovation. The author has participated in the development of the measurement systems and performed most of the measurements, except those in publication IV and the AC reference long-term stability measurement in publications II, III, and V.

1. Introduction

1.1 MEMS

The acronym for Microelectromechanical systems, MEMS, lacks a definition, but it is used to describe simultaneously a toolbox, a physical product, and a methodology all in one [1]. Typical MEMS products are mechanical actuators, sensors and other devices, which are microscopic in scale and are fabricated by integrated circuit technology. The operation principle of these components can be based on various physical phenomena and the sensors can be thermal, optical, mechanical, magnetic, etc. [2]. The devices may be either independent components or integrated into circuit devices. Microsystem technology (MST) is a platform which enables manufacturing of MEMS components characterised for their small size, low cost, low power consumption, reliability and integrability with electronics.

Currently MEMS components are applied in communication technology, automotive and transportation industry, medical and biological technologies, environmental control, etc. Hard disc drive read/write heads, inkjet printer heads, accelerometers and pressure sensors are the traditional mass market applications. Today an average car comprises more than 50 sensors, luxury models more than 100 sensors, and roughly one third of them are based on MST [3]. MEMS accelerometers are applied as air bag inflators, in Antilock Braking Systems (ABS), and in Electronic Stability Programs (ESP). MEMS based angular rate sensors or gyroscopes measure rotational motion about vertical axis (yaw rate) or longitudinal axis (rollover) of vehicles. Manifold absolute pressure sensors are also employed in the air intake manifold, where they measure the engine load by detecting the sub pressure as well as the turbo charge pressure.

Accelerometer and pressure sensors based on MEMS usually exploit micromachined beams, membranes or cantilevers. The movement is detected either capacitively or piezo-resistively. The advantages of these structures are that there is no mechanical contact causing wearing, damping can be controlled with the residual gas pressure inside the component enclosure, the characteristics of the components are predicted by conventional mechanical theory, high resonant frequencies and hence large band-widths are obtainable. The challenges

are sensitivity of microstructures to mechanical stress and fairly low capacitance values which require careful design of the readout electronics.

MEMS sensors are not only miniaturized mechanical sensors because scaling down in dimensions (d) results in stronger electrostatic force which scales as d^{-2} . A direct consequence of this is that the voltage level of capacitive transducers, as well as resolution, is usually limited by the pull-in phenomenon, not by the electric breakdown. The mechanical, the material and the electric properties as well as the sensor readout electronics and manufacturing process are tightly interconnected which makes the design of a MEMS component interesting and challenging.

1.2 Voltage metrology

The volt is defined in the International System of Units (SI) as: "*The volt is the electromotive force between two points on a conductor carrying a constant current of 1 ampere when the power dissipated between the two points is 1 watt*"[4]. Realisation of the volt depends on the experiments that relate the ampere and the volt to the mechanical units of length, force and power. Before the early 1970s Weston cells, based on electromotive force (emf), were used as voltage standards. The Weston cell consists of a cadmium amalgam anode and a mercury-mercurous sulfate cathode with a saturated cadmium sulfate solution as the electrolyte. Drift and transportability problems limited their accuracy to about 1 part in 10^6 (ppm) [5]. This accuracy was dramatically improved after Brian Josephson discovered that electrons can tunnel in pairs (Cooper pairs) between two superconductors separated by a thin insulating barrier in the superconducting state. The Josephson effect was first used with the existing Weston cell voltage standard to improve the accuracy of the measurement constant $2e/h$, where e is the elementary charge and h is the Planck constant. Soon the single-junction Josephson cells, based on fundamental physical constants rather than artefacts, replaced the electrochemical cells as voltage standards. However, the disadvantage was that they could only generate very small voltages, about 1 to 10 mV. The output voltage was increased by connecting up to about 20 junctions in series, which was difficult because of the junction non-uniformity. All the junctions required to be individually biased. In 1977, M. T. Levinson and colleagues showed that unbiased Josephson junctions

would spontaneously develop quantized DC voltages when irradiated with microwaves, opening the path to successful Josephson junction arrays [6]. Only in the last ten years the junction technology has developed to the level which enables output voltages of ± 10 V with common bias current in series-array Josephson standards [5]. Currently the relative voltage uncertainty is less than 10^{-9} at 10 V level. National metrology laboratories decided in 1990 that the AC Josephson effect is the representation of the volt and agreed that the value of the Josephson constant $2e/h$ is $K_{J-900} = 483597.9$ GHz/V.

1.3 DC voltage references

Voltage references are fundamental building blocks in a variety of instruments operating over a very wide range of accuracies. Applications range from data logging systems to digital multimeters (DMM) and precision laboratory references. Many lower precision instruments, such as handheld DMMs, do not employ separate voltage references. Their analog to digital converter usually includes a voltage reference.

Voltage reference instruments are used by calibration laboratories to maintain a local standard for voltage. Lower level equipment is calibrated against these instruments. They are also used as a means of importing traceability from higher levels within the traceability chain, usually the Josephson standard, which is the state-of-the-art instrument today.

The key performance criterion for a voltage reference is the stability with time and temperature, in particular the predictability of temporal drift, immunity to effects of humidity and atmospheric pressure, and immunity to effects of transportation in some applications.

Zener diodes and bandgap references are the most common DC voltage references either used alone or as a part of an integrated voltage reference circuit. A new reference device based on CMOS floating gate analog technology has recently been introduced. General characteristics of these references and the Josephson voltage standard shall be discussed next.

1.3.1 Josephson voltage reference

The Josephson voltage standard is the state of the art voltage reference as discussed in Section 1.2. The basic element of the reference is the Josephson junction which consists of two superconductor electrodes separated by a thin insulator layer. In a superconducting state, electrons are attracted to each other and form bound pairs, Cooper pairs, which tunnel through the junction. An applied DC voltage V across the barrier would generate an AC current at the frequency $f = 2eV/h$, where e is the elementary charge and h is Planck's constant. During each cycle of the oscillation, a single quantum of magnetic flux ($h/2e$) passes through the junction. It is difficult to directly observe this small oscillation. However, if an AC current is applied to the junction, there is a range of bias current for which the flow of flux quanta will phase-lock to the applied frequency. An applied AC current of frequency f would generate a DC voltage V_n at the quantized values $V_n = nhf/2e$, where n is an integer. This effect is known as the AC Josephson effect. The stability of the Josephson volt depends only on the stability of f . In other words, a Josephson junction is a frequency-to-DC voltage converter. The best devices today consist of 19 000 junctions and they are able to produce a series of very accurate quantized voltages up to 12 V [6].

Josephson-junction-based voltage standard systems are rather expensive and large devices mainly used by National Standards Laboratories to maintain the local standard for voltage. They consist of microwave source and feed, cryostat, probe, chip, and readout and control system. Microwave energy is fed into the chip mounted in the probe's chip carrier and the chip is cooled by liquid helium.

1.3.2 Zener diodes

1.3.2.1 Principle of operation

A Zener reference is based on the breakdown of a reverse biased p-n junction [7]. Any reverse biased p-n junction has a small reverse current flow due to the presence of minority carrier holes and electrons in the vicinity of the depletion region. As the reverse bias voltage across the junction is increased, the carriers acquire an increasing amount of energy between lattice collisions. At a certain voltage, the breakdown voltage, the carriers have enough energy to create new

electron-hole pairs in collisions with the silicon atoms. This is called the avalanche process in which the current in a reverse-biased diode dramatically increases at a certain voltage threshold. A resistor in series with the diode establishes a constant current, allowing the Zener to operate as a stable reference voltage. The Zener reference behaves as a typical shunt, or two-terminal, reference.

The operation of a Zener diode can also be based on Zener breakdown which is different from the avalanche effect described above. The Zener breakdown occurs only in very heavily doped junctions if the electric field is large enough for a valence electron to make a transition from the valence band to the conduction band. This process is a tunneling effect, but there is no multiplication effect involved. Although the Zener breakdown mechanism is only important for breakdown voltages below about 6 V, all breakdown diodes are commonly referred to as Zener diodes.

1.3.2.2 Zener diode characteristics

Lower precision Zener references offer outputs in the range from 1.2 V to 10 V with accuracies from 0.2% to 5%, and temperature coefficients in the range between 10 ppm/°C and 150 ppm/°C.

The drawbacks of the low precision Zener diodes are the substantial noise associated with surface effects, poor voltage tolerance and the dependence of Zener voltage on current and temperature. To reduce these problems, two-terminal and three-terminal reference circuits have been developed which include a number of active devices to compensate the temperature effects, provide constant current to the Zener diode, and buffer the output voltage, etc. [8].

1.3.2.3 IC Zeners

The best commercially available voltage reference integrated circuits (IC) are based on burn-in and careful selection of the Zener diode component, temperature-stabilized housing and integrated electronics.

The temperature stability of a Zener diode, which is about 0.5 ppm/°C, can be improved by an order of magnitude by utilizing the component TO-package as a temperature stabilized oven. A reference Zener, a temperature compensation

transistor, a temperature sensor transistor and a heater resistor are all on a single chip, which is mounted in a TO-package. An external circuit is required to implement a temperature control circuit to maintain the chip at a constant elevated operating temperature and supply a constant current to the reference Zener. For example the LTZ1000/100A (Linear Technology) reference utilises this technology and the temperature coefficient of the component is less than 0.05 ppm/°C and long term stability is about 1 ppm/year [8].

An even better way is to mount the whole reference circuitry in a metal box and maintain the box at an elevated temperature. This enables a temperature stability of ± 50 mC at room environment, but it is bulky, slow and has high power consumption [8].

1.3.3 Bandgap references

Voltage reference circuits usually fail to provide small temperature coefficients without a temperature control circuit, which is undesirable especially if small size and low power consumption are desired. Instead of trying to control the temperature of the circuit it is also possible to eliminate the temperature coefficient by adding the reference voltage to another voltage that has a temperature coefficient of the same order of magnitude but with different sign. The bandgap voltage reference circuit is based on compensating the negative temperature coefficient of a transistor base-emitter voltage V_{BE} with a positive temperature coefficient of the thermal voltage V_T . The thermal voltage source is realised using two identical p-n junctions having different collector current densities J_C . The base-emitter voltage difference of these two transistors is $\Delta V_{BE} = kT/e \ln(J_{C1}/J_{C2})$, where k is Boltzmann's constant and e the elementary charge and T temperature [7]. The temperature coefficients for V_{BE} and for ΔV_{BE} are about -2 mV/°C and +0.085 mV/°C respectively at room temperature T_R . When the positive temperature coefficient is multiplied with a constant K , about 23.5, the sum of these voltages has a zero temperature coefficient at T_R as shown in Fig. 1. The bandgap voltage reference compensates only the linear term of temperature coefficient and hence the temperature coefficient is zero only at one temperature T_R . Nevertheless, fairly small, about 50 ppm/°C, temperature coefficients are achievable with this technique.

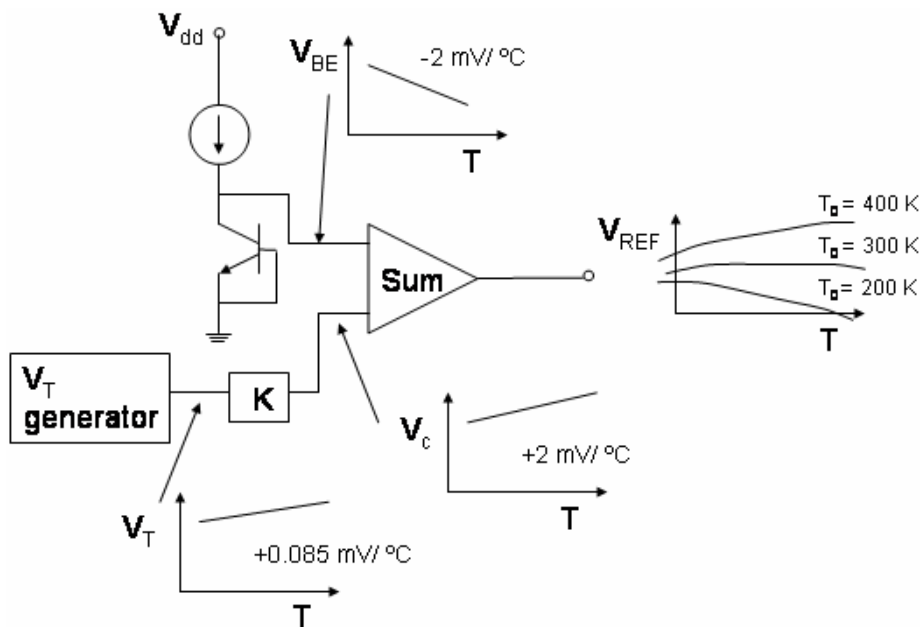


Figure 1. Bandgap voltage reference (redrawn after [7]).

1.3.4 Floating gate technology

A new commercial reference device has recently been announced by Intersil Corporation based on floating gate analog (FGA) technology, an extension of non-volatile memory [9]. FGA technology is based on storing a precise charge in a floating gate cell. The reference voltage is output from the buffered floating gate voltage. The devices, as well as the amplifier circuitry, are manufactured using CMOS process. The advantage of the FGA technology is that the reference voltage is not determined by the breakdown voltage or bandgap voltage but can be designed for a wide range of voltages.

The components are specified from 1.25 V to 5 V output with temperature coefficients from 1 to 20 ppm/°C, accuracy from 0.5 mV to 5 mV, stability of 10 ppm/sqrt(1000h), noise of 30 μ V p/p (0.1–10 Hz), at a 500 nA supply current.

1.4 AC voltage references

There are only two voltage references, which are fundamentally based on AC voltage, namely the AC voltage Josephson reference and the MEMS based AC voltage reference described in this dissertation.

Usually AC voltage sources are based on generating an AC voltage from DC and respectively an AC voltage is measured by converting the AC to DC. AC converters are fundamental building blocks in a variety of instrumentation operating over a very wide range of accuracies, like DC references discussed in Section 1.3. The middle and lower accuracy devices are simple rectifier circuits, which detect the signal peak values. The output is calibrated to give the equivalent RMS value of a sinusoidal signal. If the signal is noisy or the signal shape differs from sinusoidal, substantial errors can occur. Higher precision devices utilise sampling with fast A/D converters and RMS to DC converters realised with discrete components. Thin film or planar multijunction thermal converters (PMJTC), based on thin-film technology, can realise a zero AC-DC difference with an uncertainty below 0.1 ppm at 1 kHz [10]. However, thermal conversion is a complicated and a time consuming measurement method. The inherent limitation of thermal sensors is the need to generate heat for signal detection and ultimately the accuracy is limited by the phonon noise.

All major National Standards Laboratories are presently developing AC voltage standards based on Josephson junction arrays, discussed in Section 1.3.1. The approach is to generate a programmable digital-to-analog converter capable of synthesizing arbitrary waveforms. One of the major challenges is to fabricate uniform junctions for large arrays [5]. The AC Josephson standard suffers from the same limitations as the DC Josephson voltage standard: they are expensive, large devices, which need to be operated at cryogenic temperatures.

1.5 MEMS in voltage metrology

Microsystem technology has enabled improvement of existing voltage standards and creation of new standards based on quantum phenomena or characteristic properties of micromechanical moving plate capacitors. Two state-of-the-art standards, namely Josephson junctions and multijunction thermal converters, are

manufactured using MST as already mentioned in the previous Section. Manufacturing of a Josephson junction requires an extremely thin (few nanometers) insulator layer, which is not possible without semiconductor fabrication technologies. Multijunction thermal converters can be manufactured using traditional technologies, but MST has enabled a substantial improvement in device performance. The decreased device size (thermal mass) and reproducible manufacturing process, utilising well characterised materials, creates more accurate, faster, and less expensive MJTCs.

The potential of MEMS in metrology is discussed in [11]. During the last 10 years several new devices based on micromechanical moving plate capacitors have been suggested. The principle of operation of a true RMS-to-DC converter was first published in 1995 [12]. The operation of the device has been demonstrated using surface micromachined [13] and bulk micromachined [14] devices. Also a RMS-to-DC converter based on a SOI process and comb-structure has been presented in [15].

The principle of operation of a DC voltage reference and an AC voltage reference, both based on the pull-in phenomenon of a moving plate capacitor, were first published in 1998 [16]. Further analysis of the voltage references, as well as the principle of operation of a DC current reference, a low frequency voltage divider, and a microwave detector, are presented in [17]. The first experimental results of a DC voltage reference and an AC voltage reference are published in [17] and [18]. Those results are based on commercial bulk micromachined angular rate sensors. A surface micromachined beam designed to be used as a DC voltage reference is reported in [19] and later analysed in more detail in [20].

The previous studies demonstrated the feasibility of the idea, *i.e.* the use of the pull-in voltage as a voltage reference, but the stability of the devices has not been sufficient. This dissertation, including the publications, concentrates on analysing and solving this problem.

The approximate accuracy levels for different voltage references are compared in Fig. 2. The best standards before the invention of the Josephson voltage standard (JVS) in the early 1970s could reach an accuracy of 10^{-6} . This level of accuracy is currently achieved by high quality (HQ) Zener diodes. However, the

characteristics of the high quality Zener diodes have remained the same for tens of years, whereas the MEMS references are in the beginning of their life cycle and there is a huge potential for improvement. In addition to accuracy, also long-term stability, temperature coefficient, and noise voltage level are important characteristics of the references.

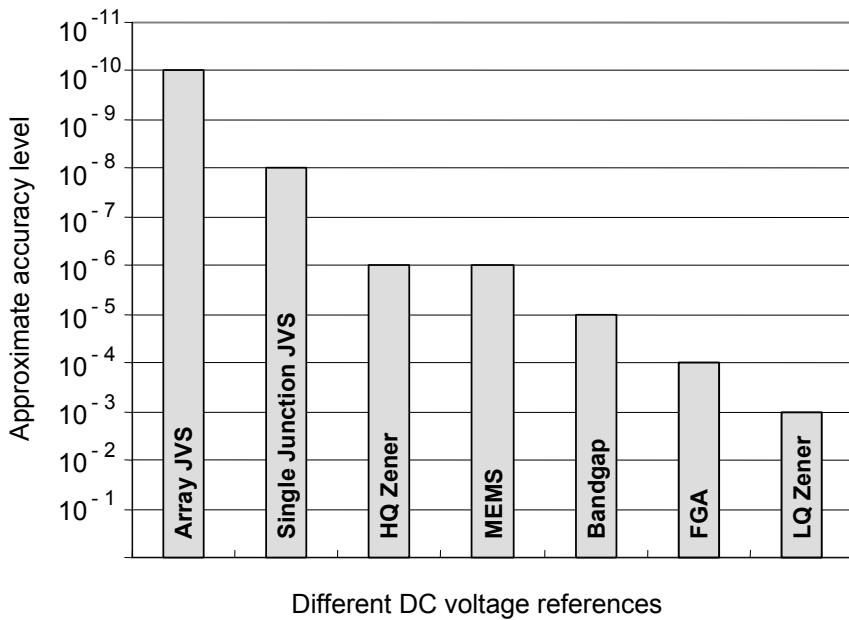


Figure 2. The approximate accuracy levels of different DC voltage references.

2. Methods

2.1 Electromechanical coupling in MEMS components

Electromechanical coupling of a moving plate capacitor, especially the pull-in phenomenon, is well known both theoretically and experimentally, for a review see [21] and [22]. However, the dynamics of a current driven microactuator in the low frequency range has not been published and will be discussed here in more detail.

2.1.1 Static analysis

A MEMS moving plate capacitor, shown in Fig. 3, is manufactured from two silicon wafers, where the upper one is etched to form a moving mass suspended by three elastic springs. The spring-mass system can be described by the dynamic equation of a forced oscillator

$$F_e(t) = m \frac{d^2x}{dt^2} + \lambda \frac{dx}{dt} + kx - F_m, \quad (1)$$

where m is the mass of the moving plate, λ is the damping coefficient, related to gas damping of the component, and k is the spring constant [23]. F_m describes the force the capacitor experiences, for example due to the ambient gravity or any other external force, and F_e the electrostatic force acting on the moving plate. In the static analysis of a parallel plate capacitor it is assumed that the variation of the actuation is slow enough, so that the system is in equilibrium all the time, *i.e.* the time-dependent terms in (1) vanish. The plate movement is analysed both in translational and rotational modes.

2.1.1.1 Translational mode

The electrostatic force F_e acting on the moving plate of the parallel plate capacitor, shown in Fig. 3, due to an external voltage V_{ext} is

$$F_e = \frac{1}{2} V_{\text{ext}}^2 \frac{\epsilon A}{(d-x)^2} = \frac{1}{2} V_{\text{ext}}^2 \frac{C}{(d-x)}, \quad (2)$$

where ε is the permittivity of the medium between the capacitor plates, d is the gap between the plates at rest position ($V_{\text{ext}} = 0$), x is the deflection from the rest position, and A is the electrode surface area [23]. The parallel plate capacitance C has an expression

$$C = \frac{\varepsilon A}{d - x}. \quad (3)$$

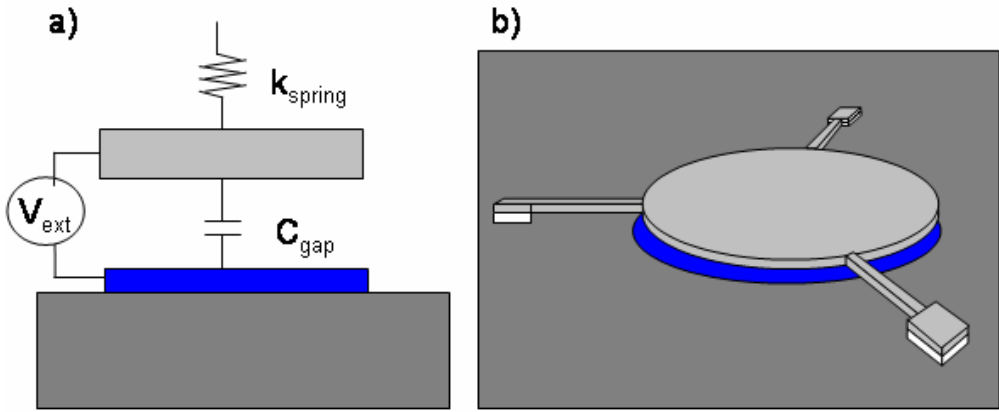


Figure 3. Schematic model for a translationally moving parallel plate capacitor (a) and its realisation with a MEMS component (b).

Assuming that there are no external forces acting on the system, $F_m = 0$, Eq. (1) simplifies to

$$\frac{1}{2} V_{\text{ext}}^2 \frac{\varepsilon A}{(d - x)^2} = kx, \quad (4)$$

where k is the spring constant

$$k = 3 \frac{Eh^3 w_s}{l_s^3} \quad (5)$$

for the plate suspended with three springs as shown in Fig. 3 [24]. E is Young's modulus, h the plate thickness, w_s the spring width and l_s the spring length. Equation (5) assumes that the spring is fixed from one end and guided from the other end.

Solving V_{ext} from Eq. (4) results in

$$V_{\text{ext}} = \sqrt{\frac{2(d-x)^2 kx}{\epsilon A}}. \quad (6)$$

The maximum of V_{ext} , *i.e.* the pull-in voltage V_{pi} , is

$$V_{\text{pi}} = \sqrt{\frac{8kd^2}{27C_0}}, \quad (7)$$

which occurs at $x = d/3$. C_0 is the nominal capacitance ($x = 0$)

$$C_0 = \frac{\epsilon A}{d}. \quad (8)$$

The eigencurve of the moving plate capacitor is shown in Fig. 4.

The pull-in voltage can be used as a voltage reference since the relative uncertainty of the pull-in voltage $\Delta V_{\text{pi}}/V_{\text{pi}}$ is proportional to the relative uncertainty of the displacement $\Delta x/d$ squared

$$\frac{\Delta V_{\text{pi}}}{V_{\text{pi}}} \approx -\frac{27}{8} \left(\frac{\Delta x}{d} \right)^2, \quad (9)$$

which results from derivation of (7). The relative displacement can easily be controlled at a level of 10^{-4} resulting to relative voltage accuracy in the order of 10^{-6} .

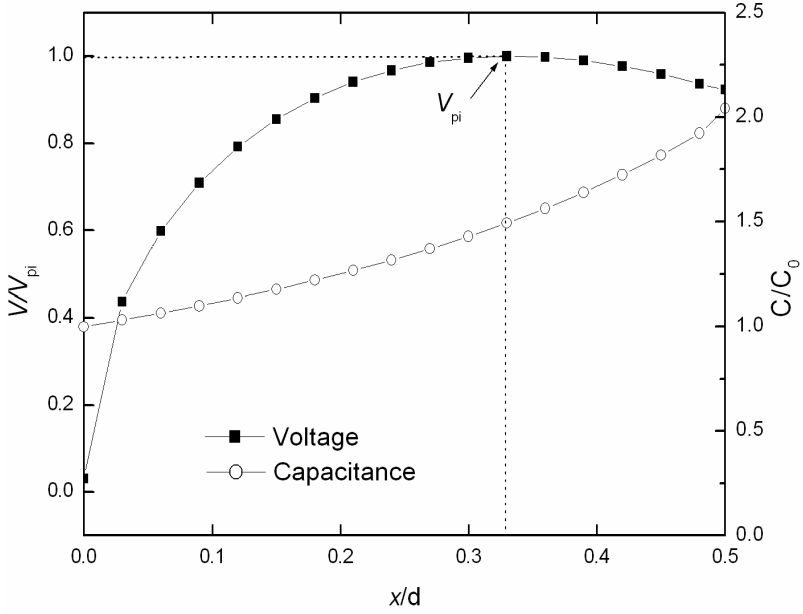


Figure 4. Eigencurve of a moving plate capacitor. The pull-in voltage is the maximum of the voltage curve.

2.1.1.2 Rotational mode

If the moving capacitor plate is suspended with two springs from the centre of the mass, as shown in Fig. 5, the plate moves in a rotational mode, *i.e.* tilts. In that case the equilibrium equation is

$$T = \kappa\varphi, \quad (10)$$

where φ is the tilt angle, κ is the spring torsion coefficient, and T is an external torque [24]. For rectangular springs, as shown in Fig. 5, the total spring torsion coefficient is

$$\kappa = 2\frac{G}{l_s}ab^3\left[\frac{16}{3} - 3.36\frac{b}{a}\left(1 - \frac{b^4}{12a^4}\right)\right], \quad (11)$$

where G is the shear modulus of silicon, l_s is the length and $a \times b$ is the cross section of a single spring ($a \geq b$) [24]. The torque can be calculated as

$$T = \int_{c-e/2}^{c+e/2} F_{dl} dl = \int_{c-e/2}^{c+e/2} \frac{1}{2} \frac{\varepsilon H V_{\text{ext}}^2 dl}{(d - l \tan \varphi)^2} = \quad (12)$$

$$\frac{\varepsilon H V_{\text{ext}}^2}{2 \tan^2 \varphi} \left[\ln \left(\frac{1 - a_1 \tan \varphi}{1 - a_2 \tan \varphi} \right) + \frac{1}{1 - a_1 \tan \varphi} - \frac{1}{1 - a_2 \tan \varphi} \right],$$

where c is the distance to the centre of the electrode, z is the length of the electrode,

$$a_1 = \frac{c + z/2}{d}, \text{ and } a_2 = \frac{c - z/2}{d}. \quad (13)$$

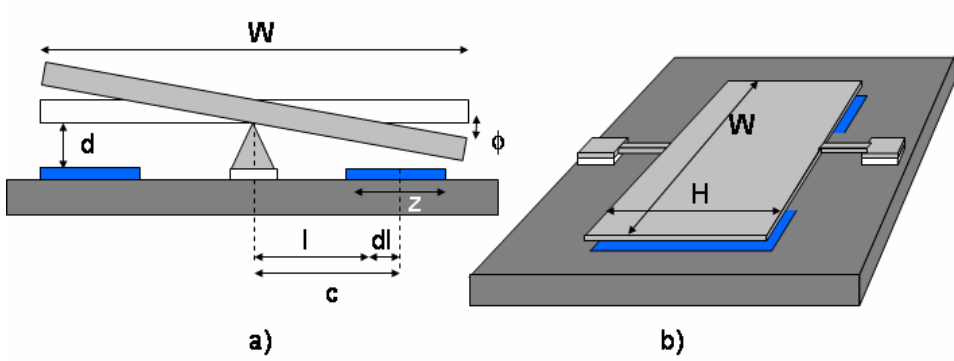


Figure 5. Rotationally moving capacitor, side view (a) including notations used in the text and a component (b).

By combining Equations (10) and (12), V_{ext} gets the expression

$$V_{\text{ext}} = \left\{ \frac{2\kappa\varphi \tan^2 \varphi}{\varepsilon H} \left[\ln \left(\frac{1 - a_1 \tan \varphi}{1 - a_2 \tan \varphi} \right) + \frac{1}{1 - a_1 \tan \varphi} - \frac{1}{1 - a_2 \tan \varphi} \right]^{-1} \right\}^{1/2}. \quad (14)$$

This equation can be solved numerically. The eigencurve of a rotationally moving capacitor is shown for different lengths of the electrode (z) in Fig. 6, and for different heights of the gap (d) in Fig. 7.

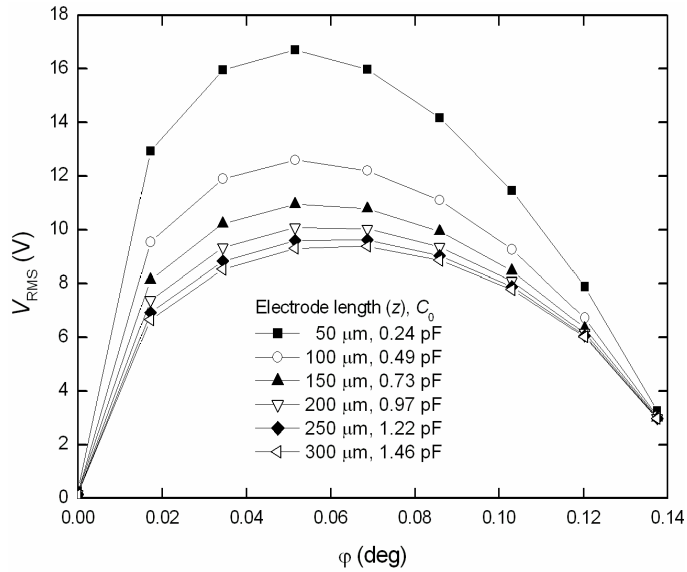


Figure 6. Eigencurve of a MEMS capacitor as a function of the rotation angle φ for different lengths of the electrode. The electrode length determines also the value of nominal capacitance C_0 , which is displayed in the legend. Other parameters used in the calculation are listed in Table 3 in Section 3.2.1.

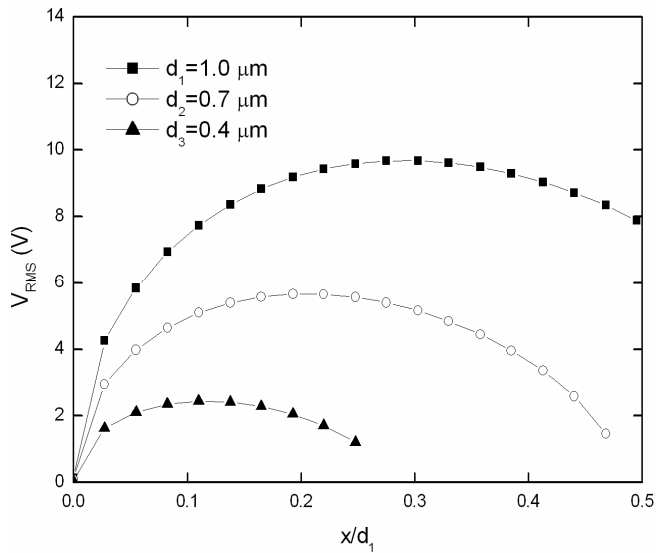


Figure 7. Component eigencurve as a function of relative displacement x/d_1 for different heights of the gap (displayed in the legend). Other parameters used in the calculations are listed in Table 3 in Section 3.2.1.

2.1.1.3 DC voltage actuation

When DC voltage is used to actuate a parallel plate capacitor, like the one shown in Fig. 3, the system is stable only below the pull-in voltage, *i.e.* for displacements $x < d/3$. The instability originates from the positive feedback to the system, which is provided by the voltage source. When the plate deflects, the capacitance increases and the voltage source adds more charge causing the plate to deflect even further. There are a number of techniques to increase the stable actuation range, for a review see [21] and [25]. The most feasible techniques for the voltage reference use are the voltage feedback, discussed below, and the actuation with an AC current source, which is discussed in the next Section.

A feedback loop enables stable actuation in the region which is unstable using a simple DC voltage source. A basic understanding of this phenomenon is obtained considering a system model illustrated in Fig. 8. The output of the system $Y(s)$ is determined by the feedback function $H(s)$ if $|K_0G(s)H(s)| \gg 1$,

$$\frac{Y(s)}{R(s)} = \frac{K_0G(s)}{1 + K_0G(s)H(s)} = \frac{1}{1/K_0G(s) + H(s)} \approx \frac{1}{H(s)}, \quad (15)$$

where K_0 and $G(s)$ are the controller and plant functions respectively. Thus, with a high open loop gain K_0 , the overall transfer function is sensitive to variations in the feedback gain factor, but relatively insensitive to variations in the transfer function [26].

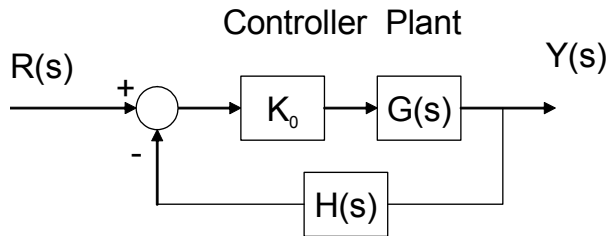


Figure 8. A general graphical presentation of a feedback loop.

A control system model for a DC voltage actuated capacitor is displayed in Fig. 9. The aim of the circuit is to keep the position of the moving plate at the pull-in point, x_{pi} , which is the system input. The controller defines the position

change dx needed to minimize the position error $e = x_{pi} - x_m$, where x_m is the measured displacement. Different kinds of controllers can be used. For a linear controller the transfer function is $G_1 = K_0$ and for a PID controller $G_1 = K_0 + K_d s + Ki/s$ [26]. The transfer function for the actuation voltage is obtained from Eq. (4), $G_2 = C_0 V_{ext}^2 / 2d(1 - x/d)^2$. The component dynamics is described by Eq. (1) and the Laplace transformation of it is

$$F(x) = ms^2 X(s) + \lambda s X(s) + kX(s), \quad (16)$$

assuming that the initial displacement and velocity vanish, *i.e.* $X(0) = 0$ and $\dot{X}(0) = 0$, as well as the external force acting on the system, $F_m = 0$. The component dynamic transfer function G_3 is then

$$G_3 = \frac{X(s)}{F(x)} = \frac{1}{m} \left(\frac{1}{s^2 + \lambda s/m + k/m} \right). \quad (17)$$

Finally, the position detection transfer function G_4 depends on the readout electronics used. For an electronics described in Section 4.1, the transfer function is

$$G_4 = \frac{\text{Re}\{V\}}{\delta x} = \frac{27}{16} \frac{V_{\text{ext,RMS}}}{d} \frac{\left(\frac{C_A}{C_m} + \frac{9}{4} \right)}{\left(\frac{C_A}{C_m} + \frac{9}{4} \right)^2 + \left(\frac{9}{4} R_s \omega C_A \right)}, \quad (18)$$

where C_A is the amplifier input capacitance, C_m is the nominal capacitance of the plate deflection detection electrode and R_s is the resistance of the silicon spring (it has been assumed that the parasitic capacitance C_p is negligible).

The overall transfer function of the feedback control system is then

$$\frac{x_{pi}(s)}{V_{\text{out}}(s)} = \frac{G_1 G_2 G_3}{1 + G_1 G_2 G_3 G_4}. \quad (19)$$

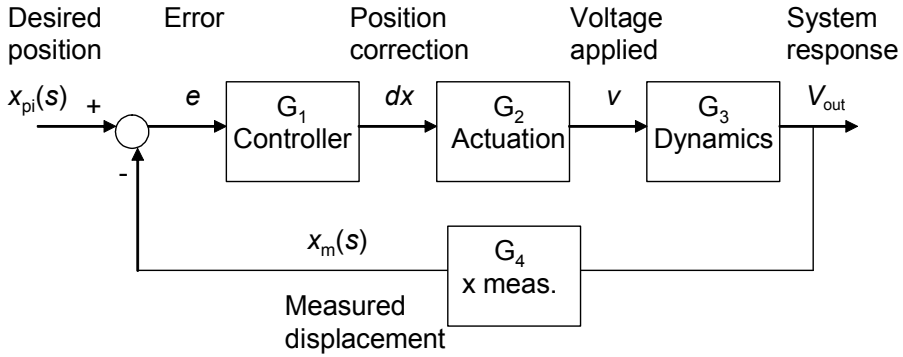


Figure 9. A feedback control system diagram for a DC voltage actuated moving plate capacitor.

2.1.1.4 AC current actuation

A DC voltage actuated MEMS capacitor is unstable at the pull-in point and the displacement x of the moving plate is limited to $d/3$ unless a feedback loop is used. The feedback system usually requires additional electrodes for the plate displacement detection and an advanced electronics for the feedback circuit implementation. These problems can be avoided by using AC current actuation. When the displacement of the capacitor is controlled using charge drive instead of voltage drive the electrostatic force between the capacitor plates does not depend on the remaining gap and hence the system is stable. It has been theoretically shown that if the AC current drive is ideal, any position across the gap is stable. In practice the maximum displacement is limited by the parasitic capacitance and leakage currents of the device [27].

If a sinusoidal current with an amplitude \hat{I} and angular frequency ω , $I = \hat{I} \sin(\omega t)$, is driven through a capacitor, the force acting on the moving plate is

$$F_e(t) = -\frac{\partial E_e}{\partial x} = -\frac{\partial}{\partial x} \left(\frac{q^2(t)}{2C} \right) = \frac{1}{2} \frac{q^2(t)}{\epsilon A} = \frac{\hat{I}^2}{2\epsilon A \omega^2} \cos^2(\omega t), \quad (20)$$

where $q(t)$ is the capacitor charge integrated from the current equation above assuming that the time average of the capacitor charge is zero, which corresponds to a vanishing DC voltage across the capacitor. The average force acting on the component is

$$\bar{F}_e = \frac{1}{\pi} \int_0^{\pi} \frac{\hat{I}^2}{2\epsilon A \omega^2} \cos^2(\omega t) dt = \frac{\hat{I}^2}{4\epsilon A \omega^2} = \frac{I_{\text{RMS}}^2}{2\epsilon A \omega^2}. \quad (21)$$

The Equation of motion (1) for a moving plate capacitor, shown in Fig. 3, is now

$$\frac{I_{\text{RMS}}^2}{2\epsilon A \omega^2} = kx - F_m \quad (22)$$

in the static case. Solving x from (22) and substituting it into the equilibrium equation

$$\frac{1}{2} V_{\text{ext}}^2 \frac{\epsilon A}{(d-x)^2} = kx - F_m \quad (23)$$

results in an expression for the amplitude of the AC RMS voltage, V_{AC} , across the plate

$$V_{\text{AC}} = V_{\text{ext,RMS}} = \frac{I_{\text{RMS}}}{\omega C_0} \left[1 - \frac{4}{27} \left(\frac{I_{\text{RMS}}}{\omega C_0 V_{\text{pi}}} \right)^2 - \frac{F_m}{kd} \right]. \quad (24)$$

The amplitude V_{AC} reaches a maximum value

$$V_{\text{AC}}^{\text{max}} = V_{\text{pi}} \left(1 - \frac{F_m}{kd} \right)^{3/2}, \quad (25)$$

where $V_{\text{pi}} = \sqrt{8kd^2 / 27C_0}$, at $I_{\text{RMS}} = (3/2)\omega C_0 V_{\text{pi}} \sqrt{1 - F_m / kd}$. This voltage amplitude value can be utilised as a reference voltage since the relative uncertainty of the reference voltage is proportional to the relative uncertainty of the driving current squared

$$\frac{\Delta V_{\text{AC}}}{V_{\text{AC}}^{\text{max}}} \approx -\frac{3}{2} \left(\frac{\Delta I}{I_{\text{RMS,max}}} \right)^2. \quad (26)$$

In Fig. 10 the RMS voltage V_{AC} is shown as a function of the RMS current I_{RMS} for a typical component with different frequency values of the driving current.

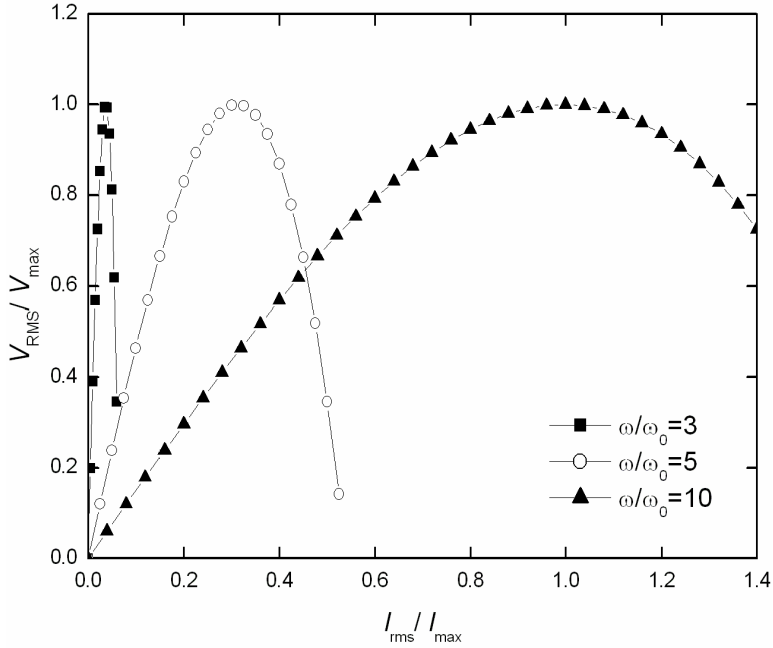


Figure 10. Eigencurves for a MEMS component with different frequency values of the driving current I_{RMS} assuming that $F_m = 0$. The undamped resonance frequency is ω_0 .

2.1.2 Dynamic analysis

In the previous analysis, it has been assumed that either the frequency of the actuation is much higher than the component mechanical resonance frequency or the motion of the moving electrode is sufficiently damped, so that the position of the moving electrode is stationary. In that case the time-dependent terms in the equation of motion (1) will vanish. However, if either of these assumptions is not valid, the plate oscillation can not be omitted. The plate movement will also generate other harmonic frequencies into the output signal in addition to the original frequency of the sinusoidal input signal. If the AC voltage is not measured using the phase locking technique, the additional frequency components will cause an error in the AC RMS value.

In order to find out the effect of plate oscillation on the reference voltage, the equation of forced oscillation needs to be solved. In the case of AC current actuation, the electrostatic force F_e acting on the component when sinusoidal current with an amplitude \hat{I} and angular frequency ω , $I = \hat{I} \sin(\omega t)$, is driven through a capacitor, is (see Eq. (20))

$$F_e = \frac{\hat{I}^2}{2\varepsilon A \omega^2} \cos^2(\omega t) = \frac{I_{\text{RMS}}^2}{2\varepsilon A \omega^2} (1 + \cos(2\omega t)). \quad (27)$$

The equation of the forced oscillator is now

$$\frac{d^2 x}{dt^2} + 2\gamma \frac{dx}{dt} + \omega_0^2 x = \frac{I_{\text{RMS}}^2}{2m\varepsilon A \omega^2} (1 + \cos(2\omega t)), \quad (28)$$

where $\gamma = \lambda/2m$ and $\omega_0 = \sqrt{k/m}$. The external force term F_m has assumed to be negligible. Equation (28) has the solution

$$x(t) = \hat{x}_0 \left(1 + \frac{1}{\Omega} \sin(2\omega t - \alpha) \right), \quad (29)$$

where

$$\Omega = \sqrt{\left(4 \left(\frac{\omega}{\omega_0} \right)^2 - 1 \right)^2 + \left(\frac{4\gamma\omega}{\omega_0^2} \right)^2} = \sqrt{\left(4 \left(\frac{\omega}{\omega_0} \right)^2 - 1 \right)^2 + \left(\frac{2\omega}{\omega_0 Q} \right)^2}, \quad (30)$$

$$\hat{x}_0 = \frac{1}{2\varepsilon A k} \left(\frac{I_{\text{RMS}}}{\omega} \right)^2, \quad (31)$$

and

$$\tan(\alpha) = \frac{4\omega^2 - \omega_0^2}{4\gamma\omega}. \quad (32)$$

The amplitude ratio between the oscillating component \hat{x}_0/Ω and the non-oscillating component \hat{x}_0 as a function of the driving angular frequency ω is shown in Fig. 11 for different Q values of the component. The component mechanical Q value, $Q = \sqrt{km}/\lambda = \omega_0/2\gamma$, varies from about 0.01 for well damped components up to 10^6 for vacuum packaged components. It can be observed that the oscillating component dominates at the energy resonance $\omega_0/2$, *i.e.* when the driving frequency equals the natural frequency of the oscillation without damping and hence the energy transfer from the applied force to the oscillator is at maximum. Above the resonance the amplitude ratio decreases as $1/\omega^2$.

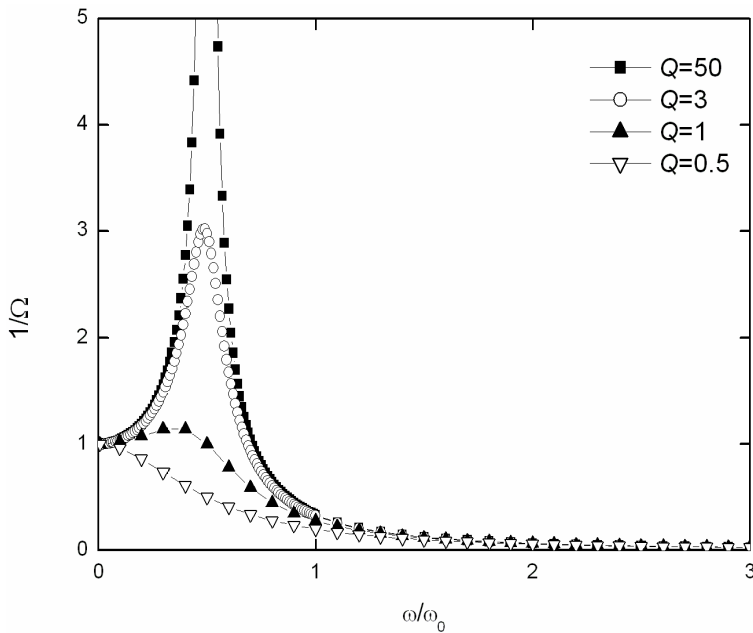


Figure 11. The amplitude ratio between the oscillating and the non-oscillating components of the capacitor plate displacement x actuated by current $I = \hat{I} \sin(\omega t)$ as function of the normalized angular frequency ω/ω_0 .

The phase α , calculated using Eq. (32), as a function of the relative angular frequency ω/ω_0 , is displayed in Fig. 12 for different Q values.

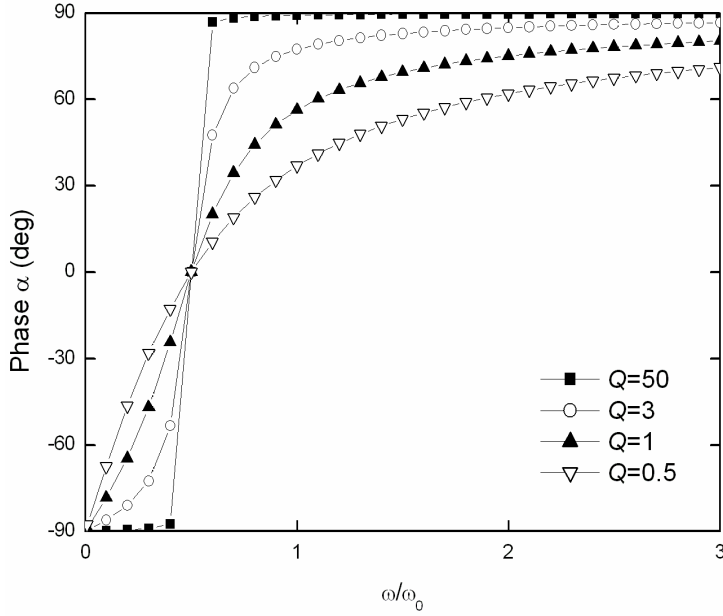


Figure 12. The phase α as function of the relative angular frequency ω/ω_0 for different Q values.

The voltage over the capacitor can now be calculated

$$\begin{aligned}
 V &= \frac{q(t)}{C(t)} = \frac{\sqrt{2}}{\varepsilon A} \left(\frac{I_{\text{RMS}}}{\omega} \right) (d - x(t)) \cos \omega t & (33) \\
 &= \hat{U}_\omega \sin(\omega t - \beta) - \hat{U}_{3\omega} \sin(3\omega t - \alpha) = U_\omega + U_{3\omega}
 \end{aligned}$$

where

$$\hat{U}_\omega = \frac{\sqrt{2} I_{\text{RMS}}}{\omega \varepsilon A} \left[\left(d - \hat{x}_0 \left(1 - \frac{\sin \alpha}{2\Omega} \right) \right)^2 + \hat{x}_0^2 \left(\frac{\cos \alpha}{2\Omega} \right)^2 \right]^{1/2} \quad (34)$$

and

$$\hat{U}_{3\omega} = \frac{\sqrt{2}}{k(2\varepsilon A)^2 \Omega} \left(\frac{I_{\text{RMS}}}{\omega} \right)^3. \quad (35)$$

The phase α is given in Eq. (32) and β is

$$\beta = \arcsin \left(\frac{-d + \hat{x}_0 \left(1 - \frac{\sin \alpha}{2\Omega} \right)}{\left[\left(d - \hat{x}_0 \left(1 - \frac{\sin \alpha}{2\Omega} \right) \right)^2 + \hat{x}_0^2 \left(\frac{\cos \alpha}{2\Omega} \right)^2 \right]^{1/2}} \right). \quad (36)$$

According to Eq. (33) the voltage across the capacitor oscillates with the driving frequency $f = \omega/2\pi$ and with the third harmonic $3f$. The amplitude ratio of these components is

$$\frac{\hat{U}_{3\omega}}{\hat{U}_{\omega}} = \frac{\hat{x}_0}{2\Omega \left[\left(d - \hat{x}_0 \left(1 + \frac{\sin \alpha}{2\Omega} \right) \right)^2 + \hat{x}_0^2 \left(\frac{\cos \alpha}{2\Omega} \right)^2 \right]^{1/2}}. \quad (37)$$

This ratio at the maximum point of the voltage-current curve is shown for a typical component in Fig. 13.

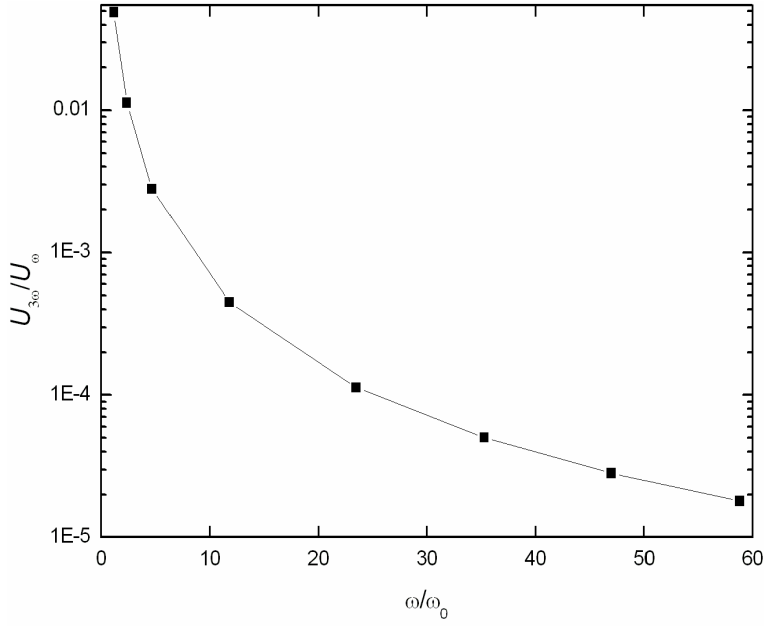


Figure 13. Amplitude ratio of the voltage components at driving frequency and the third harmonic $\hat{U}_{3\omega} / \hat{U}_{\omega}$. The following numerical values have been used: $m = 1.45 \times 10^{-6}$ kg, $A = 1.45 \times 10^{-6}$ m², $\varepsilon = 8.85 \times 10^{-6}$ C²/Nm, $d = 2 \times 10^{-6}$ m and $k = 105$ N/m.

At high frequencies, $\omega \gg \omega_0$, $\alpha \approx 90^\circ$ as can be seen in Fig.12, and Eq. (37) simplifies to

$$\frac{\hat{U}_{3\omega}}{\hat{U}_{\omega}} \approx \frac{1}{2\Omega} \frac{\hat{x}_0}{1 - \frac{\hat{x}_0}{d}}. \quad (38)$$

The RMS voltage over the moving plate is then

$$\begin{aligned} V_{\text{RMS}}^2 &= U_{\omega, \text{RMS}}^2 + U_{3\omega, \text{RMS}}^2 \\ &\approx \left(\frac{I_{\text{RMS}}}{\omega C_0} \right)^2 \left[\left(1 - \frac{\hat{x}_0}{d} \left(1 - \frac{1}{2\Omega} \right) \right)^2 + \left(\frac{\hat{x}_0}{d} \frac{1}{2\Omega} \right)^2 \right]. \end{aligned} \quad (39)$$

Hence both components, *i.e.* U_{ω} and $U_{3\omega}$, contribute to the reference voltage value. The distortion will change the value of the voltage maximum V_{RMS} and its position I_{RMS} . The voltage ratio $V_{\text{RMS}}/V_{\text{max}}$ is shown in Fig. 14 for different Q values, when the driving frequency f equals the mechanical resonance frequency f_0 . V_{max} corresponds to Q value 3.

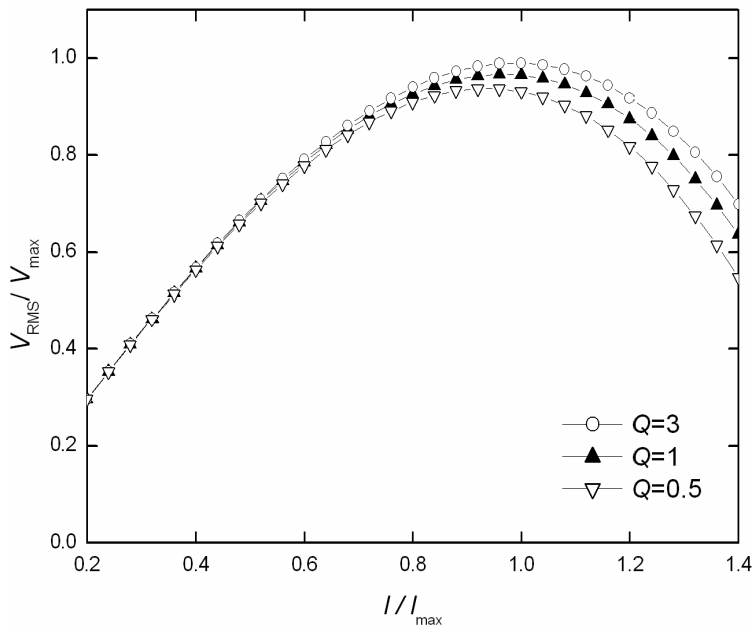


Figure 14. Reference voltage change due to the distortion with different Q values, $f = f_0$.

At high frequencies the component U_{ω} dominates and the case equals to the static case presented in Section 2.1.1.4 Only close to the mechanical resonance frequency the third harmonic component becomes significant.

2.1.3 Damping

The mechanical Q value of the moving plate capacitor can be controlled by adjusting the gas pressure inside the component enclosure. In the analysis above it was assumed that the damping coefficient is constant, which is a valid assumption for a qualitative analysis. However, for a quantitative analysis the

compressibility of the gas needs to be taken into account. In that case two different frequency domains can be observed. Below the cut-off frequency the gas has enough time to flow away from the gap, thus causing dissipation, whereas above the cut-off frequency the gas film is trapped and squeezed between the electrodes and behaves like a spring with low dissipation [28]. Further refinement of the model also includes the surface reflections of the gas molecules from the silicon and metal interfaces [29]. The major differences in the simulation results compared to the ideal harmonic oscillator model are the larger phase shift at low frequencies and generation of a new resonance in the high frequency area [28].

In voltage reference applications the component is usually actuated to the pull-in point with a frequency much higher than the mechanical resonance frequency in order to avoid the distortion caused by the third harmonic which is a potential error source in two different ways. First, if the RMS voltage is not measured using a phase-locked voltage detector, the higher harmonic will increase the voltage maximum, i.e. the value of the reference voltage, as seen from Eq. (39). Second, this voltage increase depends on the mechanical Q value related to the gas pressure in the component enclosure. As it is difficult to control the gas pressure inside the package after closing and if the hermetic package leaks with time, the reference voltage will change.

Gas damping will also increase the mechanical noise of the component [30]. The molecules in any material at a temperature above absolute zero are constantly vibrating, which gives rise to small random motions in the micro structure. The mechanical noise of the component sets the fundamental noise floor of the voltage reference [17], [18]. According to equipartition theorem the noise displacement δ_N at DC for a singly clamped cantilever, like the VTI accelerometer, is [30]

$$|\delta_N| = \sqrt{\frac{2k_B T}{\pi f_0 k Q}} = \sqrt{\frac{2k_B T}{\pi^3 f_0^3 m Q}} \quad \text{in} \left[\frac{\text{m}}{\sqrt{\text{Hz}}} \right], \quad (40)$$

where T is the absolute temperature and k_B is the Boltzmann's constant. For typical values of $T = 300$ K, $f_0 = 0.5$ kHz, $k = 30$ N/m, $f = 1$ Hz, and $Q = 1$ the noise displacement is 4×10^{-7} μm corresponding to noise voltage of 6×10^{-12} V near

the pull-in point (10 V). It has been assumed that the bandwidth is 1 Hz. The noise spectrum is flat (white noise), but shaped by the force-to-displacement transfer function of the resonator (Eq. 17) such that it peaks at the resonance frequency f_0 . Equation (40) demonstrates the fundamental relationship between mechanical noise and component size. As the component mass decreases the noise will increase. Noise of this nature can be a fundamental problem in some surface micromachined devices [30].

2.2 MEMS manufacturing technologies

Silicon micromechanics is traditionally divided into two categories: surface micromechanics and bulk micromechanics. The silicon-on-insulator (SOI) process is an emerging technology falling in between surface and bulk micromachining as far as the thickness of the structures and the lateral resolution are concerned. The unconventional surface micromachining technique LIGA (Litographie Galvanoformung, Abformung), which also allows fabrication of structures with high aspect ratio, is not discussed here since it requires X-ray lithography equipment that is not commonly available in a process line. There are a number of different variations of these manufacturing technologies and they can be combined in various ways. Hence a strict categorisation is not possible. However, depending on the desired component structure, some manufacturing processes are more feasible than others. The main processing technologies for manufacturing a moving plate capacitor using a silicon wafer is briefly reviewed next.

2.2.1 Bulk micromachining

Bulk micromachining is used in manufacturing large seismic mass devices which have applications for example in high precision, low-g accelerometers. Often the whole wafer thickness is used to process the moving beam/cantilever and the cavity is formed by bonding this wafer with another silicon or glass wafer. Bulk micromachining is based on etching single-crystal silicon. Traditionally wet etchants, like potassium hydroxide (KOH), ethylene diamine pyrocatechol (EDP) or tetramethylammonium hydroxide (TMAH), are used. It enables a good control of the dimensions, but the typical pyramid of V-groove

shapes formed in anisotropic etching limits the freedom of design and increases the device size. The recently developed plasma etching enables narrow line widths and high aspect ratios also for bulk micromachining. With Deep Reactive Ion Etching (DRIE) it is possible to obtain aspect ratios of 20:1 [31]. Loading, *i.e.* reduction of the etch rate with increasing etch area, feature charging and notching are challenges in plasma etching [32].

Single-crystal silicon wafers are stress free. However, high doping concentrations, for example $7 \times 10^{19} \text{ cm}^{-3}$ boron, used to improve the electric conductivity of the silicon or used as an etch stop layer, can cause high intrinsic tensile stress [33]. Different process steps, like oxidation or annealing at high temperatures, can change the tensile stress to compressive stress. Sandwich structures, *i.e.* a stack of wafers manufactured from different materials bonded together, are susceptible to mechanical stress, which originates from the different temperature coefficients of the materials.

2.2.2 Surface micromachining

Surface micromachining is a mature processing technology generally used in manufacturing of high-g accelerometers, pressure sensors, etc. In surface micromachining the devices are made of thin films deposited on the surface of a silicon wafer, which acts merely as a support for the structure. The most widely used materials are low-pressure chemical vapour deposited (LPCVD) polycrystalline silicon as the structural material and silicon dioxide as the sacrificial layer. The LPCVD polycrystalline layers are typically a few micrometers thick but with an epi-reactor it is possible to deposit tens of micrometers thick epitaxial films [34]. However, stress control becomes more difficult with increasing layer thickness. The major advantages of surface micromachining are the simplicity of the process and the use of standard CMOS fabrication. The major challenge is the internal stress control of the polysilicon film, which is originally under compressive stress, and the variation of the stress along the growth direction [34]. Also, planarity and stiction problems are common in surface micromachining.

2.2.3 SOI

A silicon-on-insulator (SOI) wafer is composed of two single-crystal silicon wafers with a silicon oxide layer in between. The relatively thin (1–2 μm) oxide layer can be used as an etch stop, an isolation layer, or as a sacrificial layer. Hence relatively thick silicon structures can be realised with well defined layer heights. A wide range of thicknesses are available for the structure wafer. The internal stress in SOI wafers is low [32]. Different micromachining technologies are compared in Table 1.

Table 1. Comparison of different micromachining technologies. These values vary depending on the manufacturing equipment and materials used.

	Bulk	SOI	Surface
Thickness of structures	> 10 μm	> 5 μm	< 5 μm
Lateral resolution	1.4 \times wafer thickness* / few micrometers (DRIE)	< 2 μm	< 2 μm
Tensile stress	none**	low	moderate/high
IC compatibility	no	yes	yes
Seismic mass	large	medium	small

* In $\langle 100 \rangle$ direction with anisotropic wet etch.

** Usually the stress in bulk micromachined structures arises from bonding the bulk wafer to another wafer.

2.3 MEMS component

The manufacturing process sets the rules for the component design, *i.e.* the maximum size of the released area, the minimum height of the gap, the layer thicknesses, etc. Some fundamental design considerations are discussed in this Section.

2.3.1 Component Dimensions

The size of the released structure determines the moving capacitor electrode area and hence the component capacitance value. For the readout electronics it is advantageous to have a large enough capacitance. Depending on the manufacturing design rules, the released structure should typically be smaller than $800\ \mu\text{m} \times 800\ \mu\text{m}$ in order to avoid the stiction problem.

The area of the released structure and the wafer thickness determine the seismic mass m of the component. The mass together with spring constant k determine the component mechanical resonance frequency $f_0 = \sqrt{k/m}/2\pi$. If a low resonance frequency is preferred, the component size is maximized, assuming that the spring constant remains the same. However, a massive device is more susceptible to external vibrations.

Although with micromachining it is possible to manufacture extremely thin structures or narrow features in nanometer scale, the relative accuracy is only about $10^{-1} \dots 10^{-3}$, *i.e.* orders of magnitude worse than using traditional technologies [35]. The process uniformity is a critical parameter in MEMS fabrication and has a great impact on the component yield. Also, if the dimensions of the component vary, the sensitivity and capacitance will vary accordingly elaborating the design of the readout electronics and final testing of the device.

2.3.2 Materials choices

The selection of materials available for MEMS manufacturing is large. However, in practice only a restricted number of materials is available in one single process line. The most common substrate and device wafer material is silicon, which has well characterised properties and mature processing technology.

2.3.2.1 Single-crystal silicon

Single-crystal silicon has excellent mechanical properties. Silicon shows no drift or hysteresis at normal temperatures. The resistivity of silicon varies from 0.001 to 20 000 $\Omega\text{-cm}$ depending on the doping level. High-resistivity silicon can in

some applications be used as a dielectric layer whereas high-conductivity silicon is used as an electrode material. However, silicon is brittle. It breaks if the induced stress is higher than the yield stress.

Typical material properties of silicon are presented in Table 2.

Table 2. Typical material properties of Si at 25 °C used in the calculations.

	Symbol	Si at 25 °C	Unit	Reference
Density	ρ	2.3×10^3	kg/m ³	[36]
TC*	α	2.84×10^{-6}	°C ⁻¹	[37]
Intrinsic resistivity		3.3×10^5	Ω-cm	[36]
Young's modulus	E	1.3×10^{11}	Pa	[37]
Shear modulus	G	5.75×10^{10} ... 7.9×10^{10} **	Pa	[35]
TC of Young's modulus	β	-65×10^{-6}	°C ⁻¹	[37]

* Linear coefficient of thermal expansion (TC)

** Depending on the crystal orientation.

2.3.2.2 Polysilicon

Since it is difficult to grow thin films of single-crystal silicon, polycrystalline silicon can be used instead. Polysilicon is widely used in surface micromachining as a structural layer. The internal film stress of polysilicon depends greatly on the deposition process. The stress can be controlled by deposition conditions, post deposition annealing or film doping [32]. Depending on the doping level polysilicon can be used as an insulator or a conductor. Its interface with silicon dioxide is stable and its lithography and etching properties are good [31].

2.3.2.3 Silicon oxide and silicon nitride

The most common insulators used in silicon technology are silicon oxides (SiO_x) and silicon nitrides (SiN). The high-frequency C - V curve of thermal SiO_2 shows no hysteresis or displacement of the capacitance-voltage (C - V) curve minimum point unlike other insulators. But the high deposition temperature (800...1000 °C) limits its use in later stages of fabrication, especially if metal layers have been deposited. Sputter Deposition (SD) and Plasma Exchanged Chemical Vapour Deposition (PECVD) are processed at temperatures below 400 °C, but the dielectric properties are inferior compared to thermal SiO_2 [33].

2.3.2.4 Metals

Metals in MEMS are needed for the electric contacts and in some cases for the electrode surfaces. Aluminium (Al) is commonly used especially if Al bond wires are used. Aluminium is easy to sputter and it forms a good mechanical contact with silicon. Alloys of aluminium, for example Al-1%Si, are used to increase the stability of the metallization. A disadvantage of aluminium is hillock formation at temperatures above 200 °C, which can short-circuit the narrow gap of a MEMS structure. Hillocks are small protrusions, which are formed when compressive stresses in Al relax [31]. Hillock formation can be reduced by sputtering a thin layer of another metal, molybdenum for example, on the top of the aluminium. Al also forms a native oxide layer.

Other generally used metals in MEMS manufacturing are molybdenum (Mo), tungsten (W), copper (Cu), and tantalum (Ta) and several compounds and alloys like TiW, Al-Cu etc. The electric resistivities vary from 1.92 $\mu\text{ohm-cm}$ (Cu) to 48 $\mu\text{ohm-cm}$ (Ti) [31]. The thin film resistivity is often much higher than bulk resistivity.

Gold (Au) would be an ideal metal in many MEMS applications since it is a noble metal and thus does not oxidise or form any other compounds with processing chemicals. However, gold is not CMOS compatible and it is not available in many clean rooms.

Some metals can produce a large change in its electric resistivity due to gas adsorption and are therefore used as gas sensors. Metal oxides ZnO , TiO_2 and

In₂O₃ as well as precious catalytic metals Pt and Pd should be avoided when a stable capacitor electrode is desired [2].

2.3.3 Parasitic capacitance

Parasitic capacitance is usually minimized in a MEMS component design, because it causes a loss of sensitivity as will be demonstrated in Section 4.1. The major sources of the parasitics are the anchoring areas of the released structures, which are also used for the electric contact (bonding or flip chip) to the moving electrode and hence need to be at least 100 μm × 100 μm. A typical parasitic capacitance value for a component which has three springs (see Fig. 3) is

$$C_p = 3 \times \frac{\epsilon_{ox} A}{d} = 3 \times \frac{3.4 \times 10^{-11} \text{ F/m} \times (100 \mu\text{m})^2}{1 \mu\text{m}} = 1.0 \text{ pF} \quad (41)$$

assuming that the oxide layer thickness is 1 μm between the upper and lower electrodes. Hence the parasitic capacitance can be the same order of magnitude as the work capacitance of the MEMS component. Other sources for the parasitics are the connection wires, which should be kept as short as possible and well shielded.

2.3.4 Packaging

Packaging provides mechanical support, protection from the environment, and electrical connection to the MEMS component. These functions can also be separated between different levels of packaging. For example, the zero-level package can be wafer-level encapsulation, *i.e.* bonding of an additional silicon or glass wafer on top of the MEMS device wafer, which provides hermetic enclosing and mechanical shield. The first-level package can be a dual in-line (DIP or DIL) package, including also the readout electronics, which provides the electrical connections. In volume production it is economical to use standard packages for further component handling in testing and final mounting on a printed circuit board (PCB).

In the voltage reference application the mechanically induced stress to the component due to rigid mounting is critical. Often an elastic adhesive is used as die-attached material in order to minimize the mechanical stress due to package bending caused by mechanical stress or temperature induced stress [38]. The thermal expansion coefficient (TC) of the package should be equal or slightly greater than the TC of silicon for reliability since thermal shock or thermal cycling may cause die cracking and delamination if the materials are unmatched or if the silicon is subject to tensile stress [39].

An open capacitive structure is very sensitive to changes in humidity, pressure etc. Hence the sensor needs to be encapsulated in vacuum or in a protective gas atmosphere. Inertial gases, like argon or nitrogen, are commonly used. High gas pressure works as a mechanical damper as discussed in Section 2.1.3. Suitable hermetic packages for MEMS components are metal packages (TO-can, DIL, etc.) and ceramic Low Temperature Co-fired Ceramic (LTCC) packages. Also wafer level encapsulation is an economical and high quality option for packaging, which results in a small sensor size. Before the final lid seal, a bake is usually performed to drive out any trapped gas or moisture. This also reduces the moisture related corrosion of metals in the component.

The electric contacts to the MEMS component are usually done using wire bonding, conductive adhesive, soldering or Controlled Collapse Chip Connection technology (C4), generally called flip-chip, depending on the number and size of contact pads, component temperature durability, etc. Soldering and flip-chip connections can cause stress to the component [39] and should hence be avoided in voltage reference use.

2.4 VTI accelerometer

Several measurements presented in this dissertation are performed using bulk micromachined accelerometers manufactured by VTI Technologies Oy [40]. The accelerometer is a cantilever attached at one end as shown in Fig. 15. The component consists of three silicon wafers. A silicon wafer where the moving structure is etched is anodically bonded between two glass-covered silicon wafers. A single component comprises of two identical capacitors which are formed by the surfaces of the moving mass and the fixed electrodes above and

below it. The components are enclosed in a gas atmosphere by wafer level anodic bonding. The pressure inside the cavity is high enough to over damp the cantilever movement, *i.e.* the mechanical Q value is well below 1. The components are sensitive to inclination change, which is characteristic for an accelerometer, and therefore they are not optimal in voltage reference use.

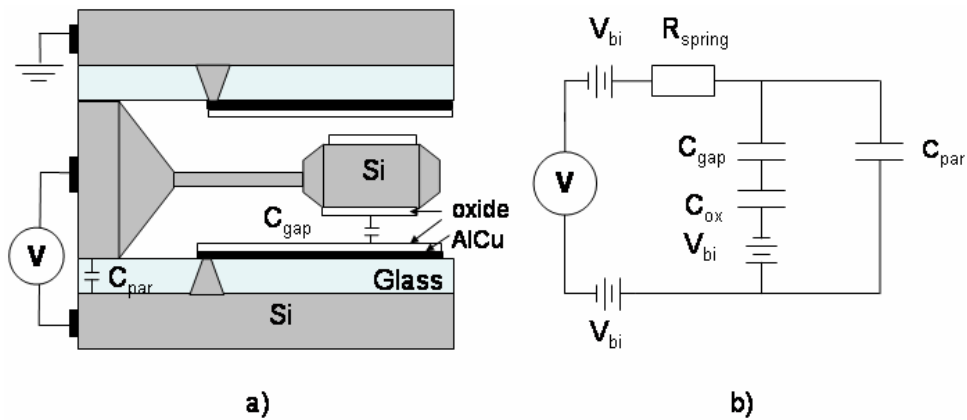


Figure 15. a) A schematic view of an accelerometer by VTI Technologies and b) its equivalent circuit. V is the external voltage source, V_{bi} is the built-in voltage of the metal-silicon junction. C_{gap} is the component capacitance (work capacitance), which has a parasitic capacitance C_{par} in parallel. C_{ox} is the capacitor formed by the dielectric layer (usually SiO_2). R_{spring} is the resistance of the silicon spring.

The electrode materials varied. Most of the components had AlCu, Ta or Mo coating on the non-moving electrode. Some of the components had a dielectric layer processed on top of the metal. Also the moving electrode was metallised in some of the components.

2.5 Stability of a MEMS component

Fundamental factors effecting the stability of the reference voltage, according to Eq. (7), are the stability of the spring constant k , the gap d , the permittivity ϵ , and the electrode area A of the component. A stable spring constant is achieved by using stress free single-crystal silicon springs. Although single-crystal silicon

is mechanically an extremely stable material, the spring constant has a temperature coefficient arising mainly from the temperature coefficient of the modulus of elasticity (Young's modulus), which is in the order of $-6 \times 10^{-5}/^{\circ}\text{C}$. However, usually the temperature coefficient of the device is 10–20 times higher, which results from a change in the gap due to mechanical stress.

Voltage references are operated at the pull-in point, which implies that there is a high electric field (about 0.1 MV/cm) between the electrodes. Various electrostatic surface and interface effects are potential sources of electrical instability. Especially metal-silicon interface effects and oxide charging can reduce the stability of the device as will be discussed below.

2.5.1 Component structure

An ideal capacitor, which is desired in the voltage reference application, is mechanically stable and the surface potentials of the electrodes are well defined. A semiconductor surface may be unstable due to surface charges, which will cause energy band bending [36]. Hence metal electrodes are preferred although metallizing the moving electrode significantly complicates the manufacturing process of the component. A cross section of a component with metal electrodes is shown in Fig. 16.

The electric contact to the upper electrode goes through the silicon spring. From an electrical point-of-view it would be advantageous to access the metal directly in order to avoid the built-in voltage V_{bi} between silicon and metal. However, this would require metallizing the spring which would significantly reduce the mechanical stability of the component. A metal layer on the silicon spring would induce stress and also increase the temperature coefficient due to the bi-metallic effect. If the metal contact on top of the moving plate is processed of the same metal as is used for the electrode coating, the built-in voltages should cancel each other.

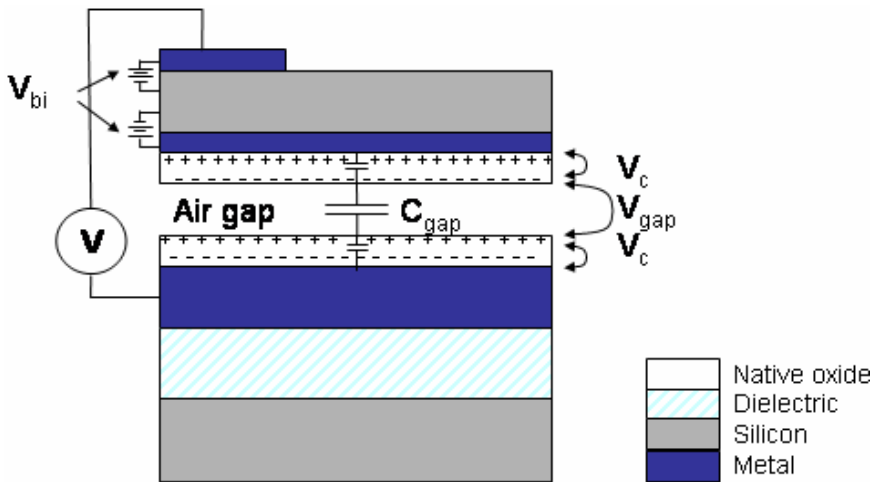


Figure 16. A cross section of an ideal MEMS moving plate capacitor (not in scale). V_{bi} is the built-in voltage between metal and Si and V_c is the potential caused by oxide charging.

Surfaces and interfaces, where defects are concentrated, are areas where charges are preferentially trapped and hence potential sources for instability. The design goal for the moving plate capacitor design presented in Fig. 16 was to minimize these effects. However, still a metal-silicon surface and a native oxide layer exist and their effect on the device stability will be discussed in the next Section.

2.5.2 Built-in voltage

The energy band diagram of a metal and an n -type semiconductor interface before and after contact is displayed in Fig. 17. When an n -type semiconductor is attached to metal, electrons will diffuse from the semiconductor to the metal since the Fermi level E_F of the semiconductor is higher than the Fermi level of the metal. A negative surface charge will be created on the metal side whereas a positive charge will be created in the semiconductor depletion region. This charge imbalance will create an electric field which opposes the diffusion current. Electrostatic potential related to this field bends the energy bands on the semiconductor side. At equilibrium the electrostatic potential balances the Fermi level difference.

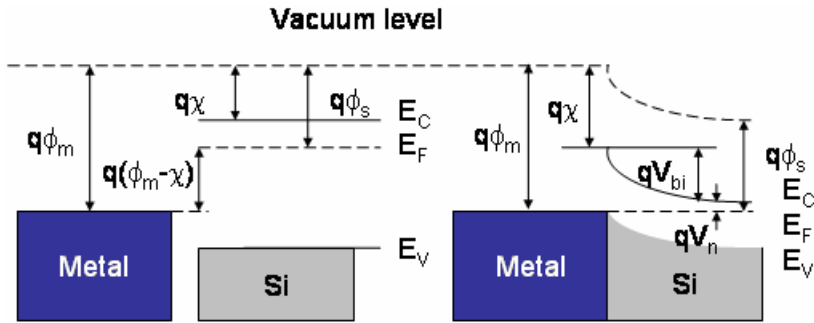


Figure 17. Energy band diagram of an isolated metal adjacent to an n-type semiconductor under thermal non-equilibrium condition and metal-semiconductor contact in thermal equilibrium (redrawn after [36]).

The built-in voltage V_{bi} is defined as the potential seen by the electrons in the conduction band trying to move to the metal

$$V_{bi} = \phi_{Bn} - V_n = \phi_m - \phi_s, \quad (42)$$

where qV_n is the difference between the bottom of the conduction band and the Fermi level. Similar results also apply for p -type semiconductor. Hence the built-in voltage can be calculated from the work function difference of the materials. The work function difference varies with the doping concentration. For p -type silicon the work function difference increases as a function of the doping level and for n -type silicon the work function difference decreases as a function of the doping level [36]. For example in the case of aluminium and p -type silicon, $N_A = 10^{18}$, $V_{bi} \approx 4.1 \text{ V} - 5.1 \text{ V} = -1.0 \text{ V}$. However, in practice the situation is more complicated. The disruption of the crystal lattice produces a large number of surface energy states located in the forbidden bandgap. These surface states can act as donors or acceptors that influence the final determination of the barrier height [36].

The built-in voltage of the moving plate capacitor can be experimentally determined from the component C - V curve as the offset voltage with respect to zero bias voltage as shown in Fig. 18. Hence the built-in voltage translates the C - V curve along bias voltage axis, but does not change the shape of the curve.

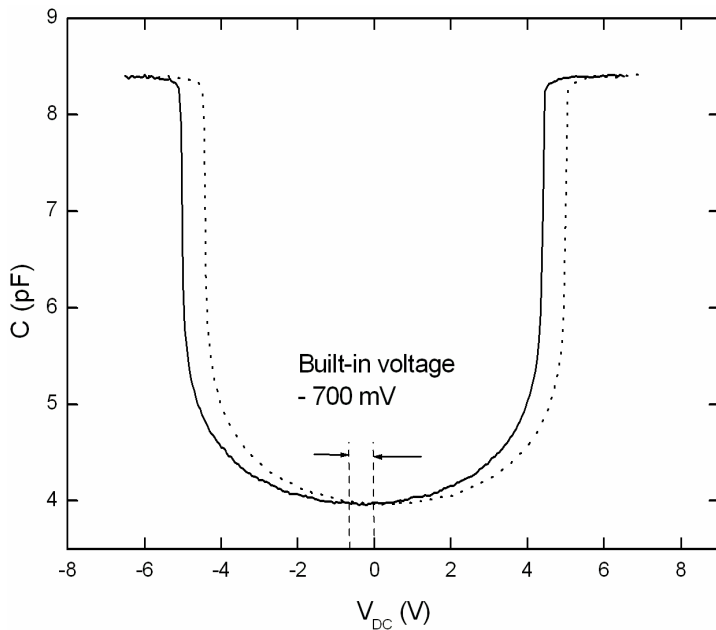


Figure 18. *C-V curve of a moving plate capacitor.*

Extensive studies on the built-in voltage and its temperature dependence for different MEMS components manufactured by VTI Technologies Oy (mainly accelerometers) have been done [41, 42]. The non-moving electrode of the VTI components is different from the metal-semiconductor structure presented above. The electric contact to the non-moving electrode goes via silicon as shown in Fig. 15 in Section 2.4. Also, in some devices the moving electrode was not coated with metal and some metal electrodes had an additional SiO₂ coating. However, the measurement results still have general applicability. The measured built-in voltage values agreed only partly with theory. Large variations were observed in the built-in voltages, even for components from the same wafer. The built-in voltages and their temperature coefficients were lower in the metal-metal structures, especially in the Mo-Mo structures, than in the metal-Si structures. A SiO₂ layer on top of the metal generally decreased the values of the built-in voltage as well as its temperature dependence. A thick SiO₂ layer could even change the sign of the built-in voltage which suggests that the layer was heavily charged. Theoretically the SiO₂ layer on top of the metal electrode should not have an effect on the temperature dependence. It is suggested in [42] that the trapped charges in the oxide balance the temperature dependence.

However, another explanation is that there are residuals of process chemicals inside the component enclosure, and their adsorption on the metal surfaces varies with temperature which causes a change in the surface potential. The SiO₂ layer passivates the electrode surface and hence reduces the temperature dependence. This theory is in agreement with the stability study of a MEMS resonator, where the humidity inside the component enclosure was observed to cause drift of the resonance frequency [43].

2.5.3 Depletion layer capacitance

When a bias voltage is applied to the metal-semiconductor junction the energy band diagram will change as shown in Fig. 19 for a *p*-type semiconductor. When the bias voltage is zero (case a), the band diagram is in thermal equilibrium and the Fermi levels of both materials are equal (as also shown in Fig. 17 for an *n*-type semiconductor).

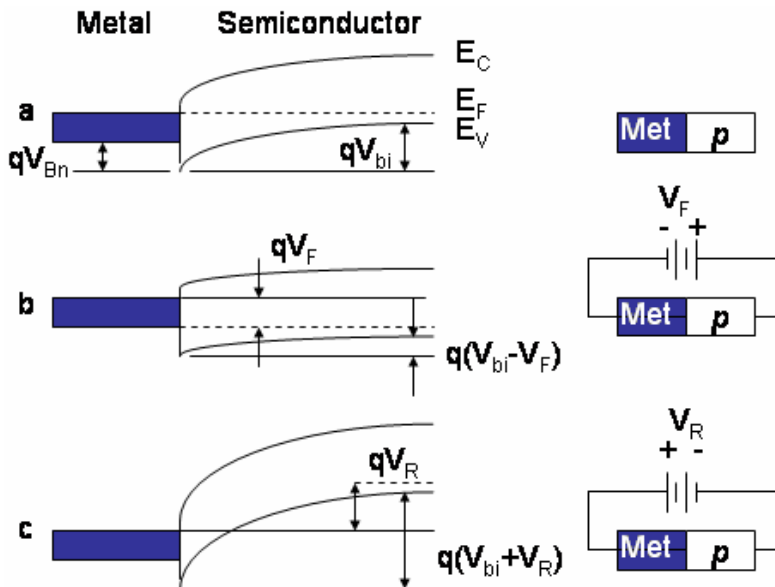


Figure 19. Energy band diagram of a metal *p*-type semiconductor junction under different bias conditions: a) thermal equilibrium b) forward bias V_F and c) reverse bias V_R .

If a negative voltage V_F (forward bias) is applied to the metal with respect to the semiconductor, electrons can easily move from the semiconductor to the metal because the semiconductor-to-metal barrier height has decreased by voltage V_F (case b). A reverse bias V_R (case c) has the opposite effect. It increases the barrier height by V_R .

The charge and field distributions for a metal-semiconductor contact are shown in Fig. 20 a) and b) respectively.

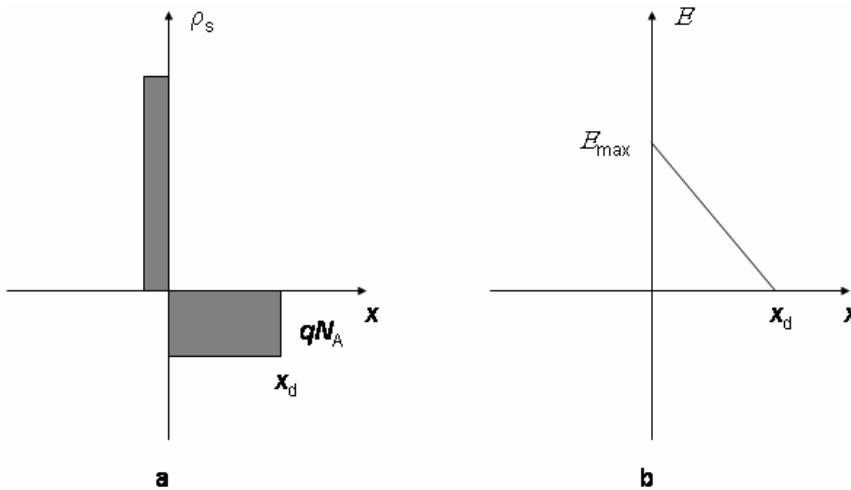


Figure 20. Charge distribution (a) and electric field distribution (b) in a metal *p*-type semiconductor junction.

Assuming that the metal is a perfect conductor and the extent of the space charge ρ_s in the semiconductor is x_d , *i.e.*, the $\rho_s = -qN_A$ for $x < x_d$ and $\rho_s = 0$ for $x > x_d$, the electric field distribution is given by

$$E(x) = \frac{qN_A}{\epsilon_s}(x_d - x) = E_{\max} - \frac{qN_A}{\epsilon_s}x \quad (43)$$

where N_A is the acceptor density, ϵ_s is the permittivity of the semiconductor, and E_{\max} is the maximum electric field located at the junction interface. The voltage across the space charge region is

$$V_{bi} - V_{bias} = \frac{E_{max} x_d}{2} = \frac{q N_A x_d}{2 \epsilon_s} \quad (44)$$

where V_{bias} equals $+V_F$ for forward bias and $-V_R$ for reverse bias. The depletion region x_d forms a voltage controlled capacitor with capacitance

$$\frac{C_{dep}}{A} = \frac{\epsilon_s}{x_d} = \sqrt{\frac{q \epsilon_s N_A}{2(V_{bi} - V_{bias})}} \quad (45)$$

This capacitance is in series with the moving plate capacitance and it can have a significant effect on the reference voltage. The MEMS capacitance is typically order of pF while the depletion layer capacitance is order of nF. The bias voltage required to eliminate the depletion region capacitance is well above the component pull-in voltage due to the voltage division between these capacitances. The relative change of the pull-in capacitance $(C_{pi} - C_{tot})/C_{pi}$, where $C_{tot} = C_{pi} C_{dep} / (C_{pi} + C_{dep})$, as a function of the relative forward bias V_{bias}/V_{bi} is shown in Fig. 21.

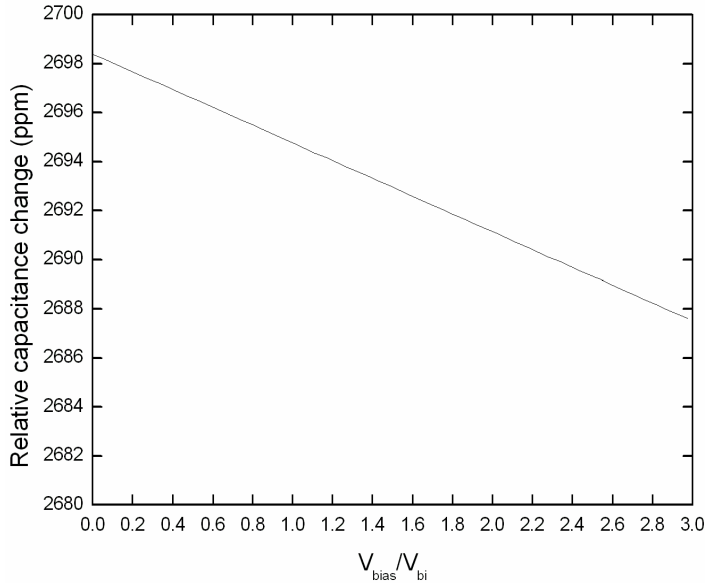


Figure 21. Relative change of the pull-in capacitance as a function of relative forward bias voltage assuming acceptor density $N_A = 2 \times 10^{18}$ (corresponds to Si resistivity of $0.02 \Omega\text{-cm}$), $V_{bi} = 0.7 \text{ V}$ and gap $1 \mu\text{m}$.

The depletion region capacitance can be reduced by a good ohmic contact between the metal-semiconductor interface, *i.e.* low contact resistance, by extra doping the contact area of the silicon [36]. Also, it is advantageous to connect the high potential to the moving mass if *p*-type silicon is used (forward bias).

2.5.4 Electrostatic charging

Formation of a native oxide on the surfaces of electrodes is difficult to avoid even when the electrodes are coated with metal. A dielectric layer can have a considerable amount of trapped charges [45]. A sheet charge causes a voltage V_c between the electrodes [36]

$$V_c = -\frac{d_{\text{ox}}\sigma_{\text{ox}}}{\epsilon_{\text{ox}}}. \quad (46)$$

If the dielectric layer is native oxide on silicon, V_c is typically of the order of -50 mV, assuming that the SiO₂ layer thickness d_{ox} is 1 nm, permittivity is $\epsilon_{\text{ox}} = 3.8 \epsilon_0$ and surface charge density σ_{ox} is 10^{12} e/cm^2 . Hence the charges create a potential difference over the component the same way as the built-in voltage does. The offset voltage of a C - V curve is the sum of these two voltages.

A charged dielectric layer can also have another effect on the C - V curve since it can reduce the effective gap of the component as shown in Fig. 16. Depending on the location of the charge in the dielectric, the amount of the gap reduction is between the height of the dielectric layer (charges locate on the air-dielectric surface) and zero (charges locate on the metal-dielectric surface). Charges in dielectrics are discussed in the next Section in more detail. The effect of the gap reduction on the component C - V curve is shown in Fig. 22.

A change in the component parasitic capacitance transfers the C - V curve along the capacitance axis, but does not change the shape of the curve as seen in Fig. 22.

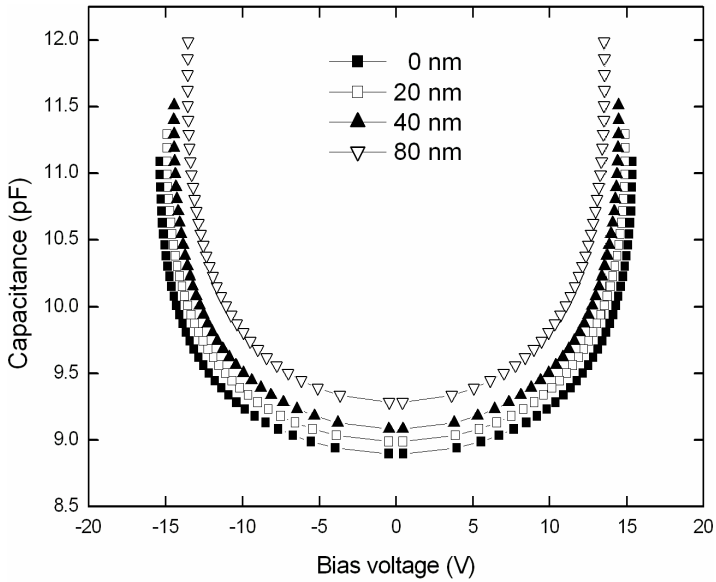


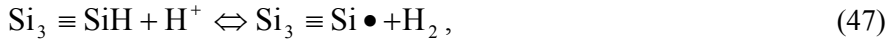
Figure 22. *C-V curve for the round component (dimensions listed in Table 5) with a nominal gap value of $1\ \mu\text{m}$ ($\delta g = 0\ \text{nm}$) and reduced gap values. The gap reduction, δg , is 20 nm, 40 nm, and 80 nm. The change of the *C-V* curve offset (232 mV for 50 nm thick oxide assuming charge density $10^{11}\ \text{e}/\text{cm}^2$) does not show in this scale.*

2.5.4.1 Charges in dielectrics

Charge trapping mechanisms in dielectrics have been investigated for more than 30 years in association with metal-oxide-semiconductor (MOS) transistors [36]. The scaling down of the MOS devices has recently activated this research field again. The Negative Bias Temperature Instability (NBTI) has been observed to shorten the lifetime of p-channel field-effect MOS transistors when stressed with negative gate voltage at elevated temperatures [46]. Another commercially important application, where dielectric charging degrades the device operation, is a capacitive RF-MEMS switch [47]. Although much effort has recently been dedicated to study the dielectric charging, details of the phenomena are not yet clearly understood.

Traditionally charges in MOS capacitors are classified in four groups: interface-trapped charges, fixed oxide charges, oxide-trapped charges, and mobile ionic charges [36]. In addition to these charges, in moving plate capacitors there are surface charges at the electrode-air interface.

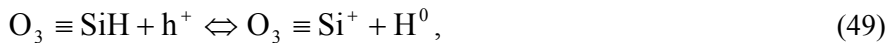
An interface trap charge, Q_{it} , results from the silicon dioxide and silicon (SiO₂-Si) interface properties and it is dependent on the chemical composition of the interface. The trap density in the <100> orientation can be as low as 10^{10} cm⁻², about an order of magnitude smaller than in the <111> orientation [36]. Si dangling bonds, *i.e.* trivalent silicon atoms with an unsaturated valence electron, $Si_3 \equiv Si \bullet$, act as interface trap centres, which are usually passivated by low-temperature hydrogen annealing. Subsequent arrival of a positively charged ion at the interface can cause depassivation of the SiH bond, which is suspected to cause the NBTI. There are two basic approaches to explain this phenomenon: the hydrogen model [48] and the chemical reacting model [49]. In the hydrogen model as the SiH bond breaks, due to an electric field for example, H^+ diffuses away and reacts directly with SiH. The products of this reaction are an H_2 molecule and a positively charged dangling bond centre:



where $\equiv SiH$ is a hydrogenated trivalent silicon and H^+ is positively charged hydrogen ion (proton). H_2 can later dissociate and act again as a catalyst to disrupt additional SiH bonds. In the chemical reacting model a species Y diffuses to the SiO₂-Si interface and creates a trap and X . Y can be, for example, a neutral water molecule and a hole at the silicon surface ($Y = H_2O + h^+$) and X is then H^+ . The interface trap creation via hydrogen model can be modelled as



A fixed oxide charge Q_f can be regarded as a sheet charge locating near the SiO₂-Si interface. This charge is fixed and cannot be affected over a wide variation of surface potential [36]. Generally Q_f is positive and depends on oxidation and annealing conditions and on silicon orientation. For <100> oriented silicon the Q_f is typically $10^{10} \dots 10^{12}$ cm⁻². Similar to interface trap creation model fixed charges can be modelled as



where h^+ is a hole and H^0 is a neutral hydrogen atom. An interface trap and a hydrogenated trivalent silicon defect in SiO₂ are illustrated in Fig. 23. Interface

trap charges and fixed charges can be distinguished with a $C-V$ measurement. As the applied bias voltage is varied, the Fermi energy at the oxide-semiconductor interface changes accordingly and affects the occupancy of the surface states. The interface states cause the transition in the capacitance measurement to be less abrupt. The combination of the low frequency and high frequency capacitance allows a calculation of the surface state density [36].

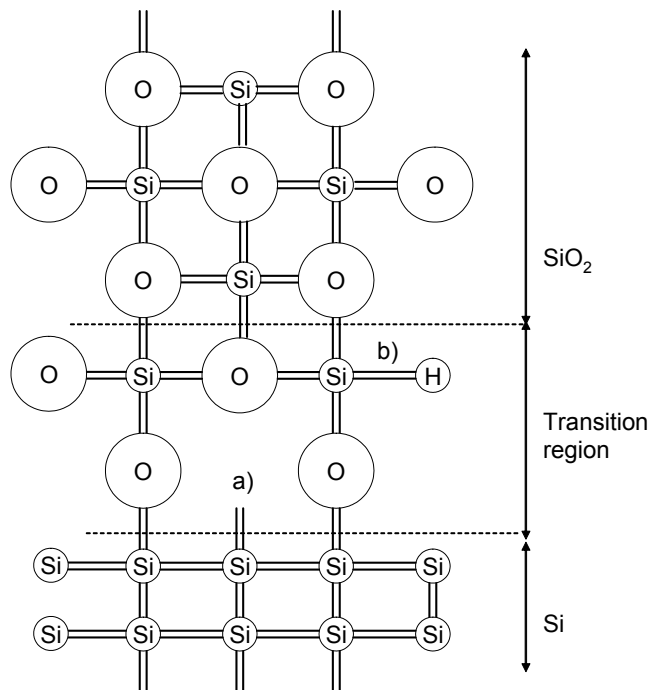


Figure 23. A silicon atom forms a covalent bond with its four nearest neighbours in wafer bulk. The crystal lattice is broken at the SiO₂ interface. In the transition region there are a) interface traps (dangling bonds) and b) $\equiv \text{SiH}$ defects. Redrawn after [49].

Mobile oxide charges result from ionic contamination due to Na⁺, Li⁺, K⁺, Ca⁺⁺, and Mg⁺⁺. They are impurities that are carefully controlled in IC processes. Especially sodium was a big concern in early days of MOS manufacturing. The glass used in anodic bonding contains sodium and for this reason anodic bonding is not a CMOS compatible process. Since anodic bonding is used in manufacturing of the VTI sensors they contain mobile sodium ions. Hydrogen is the most common impurity in IC fabrication and cannot easily be avoided.

H^+ can exist for prolonged periods in oxides as a mobile charge [46]. On the other hand, hydrogen is also used to passivate Si dangling bonds as discussed earlier.

As a summary, common to all these charging models is that they depend on the electric field in the oxide and that the charging saturates over time (unlike the oxide-trapped charges, which are due to defects in the SiO_2 , and are very stable). Threshold voltage shifts of MOS structures in the NBTI experiments have been found to be proportional to the electric field as E_{ox}^m , where m lies in the range of $1.5 \leq m \leq 3$ [46], whereas in RF-MEMS switch reliability studies, the electric field dependency has been measured to be exponential ($\exp(E)$) [50]. The major difference between these experiments is the thickness of the oxide layer, which is in the order of nanometers in the NBTI studies and two orders of magnitude thicker in the RF-MEMS studies. In thin oxides the charges can tunnel from the insulator to the semiconductor and vice versa [51] which could explain the difference. Also the oxide quality and deposition process has a significant impact on the charging properties which complicates the analysis of the charging effect.

The charging analysis above considers only silicon dioxide, which is the most extensively studied dielectric material. Also other materials, especially high dielectric constant (ϵ) materials like $SiON$, Al_2O_3 , HfO_2 , Al_2O_3 , ZrO_2 and silicates, have been experimented. There is no direct relationship between an insulator conductivity and its charging properties since the trapped charges are rather related to the defects in the crystallographic structure than to the nature of the bulk material (ionic or covalent bond) [47]. Still, some of the experiments demonstrate low density of interface defects for high dielectric constant materials. Also a recently proposed model, further developed from the hydrogen model, proposes that the saturation voltage of a MOSFET threshold voltage shift, is proportional to $1/\epsilon$ [52].

2.5.4.2 Oxide charging models

The time dependence for oxide charging under bias voltage has been studied for both pFETs [52] and for RF-MEMS switches [50]. The first model is based on physical principles of SiO_2 interface (hydrogen model discussed earlier). According to this model the threshold voltage shift ΔV_t of a transistor is

$$\Delta V_t = -\frac{Q_{it} + Q_f}{C_{ox}} = \Delta V_{\max} \left(1 - \exp\left(-\frac{t}{\tau}\right)^\gamma \right), \quad (50)$$

where the ΔV_{\max} depends on the electric field, initial SiH density, oxide thickness, energy levels of interface and oxide traps and dielectric constant of the oxide. γ is a constant related to dispersive diffusion of bonded and interstitial hydrogen atoms (often assumed to be approximately 1 for thick oxides) and τ is a time constant.

The oxide charging model developed for RF-MEMS switches takes also into account discharging observed to occur during long experiments. If N_0 is the total trap density, e elementary charge, τ_1 time constant for charging, and τ_2 time constant for discharging, the surface charge σ gets an expression

$$\sigma = N_0 e \frac{\tau_1}{\tau_1 + \tau_2} \left(1 - \exp\left(-\frac{\tau_1 + \tau_2}{\tau_1 \tau_2} t\right) \right). \quad (51)$$

In pFETs and switches the moving plate is in contact with the oxide layer but in the voltage reference application the capacitor formed by the air gap, C_{gap} , significantly reduces the voltage over the oxide layer. Since MEMS capacitances are typically in pF-region and the oxide capacitances is in nF-region the voltage over the oxide is three orders of magnitude smaller than the applied bias voltage.

2.5.5 Mechanical stability

Mechanical deformation of the electrodes can change the gap d . Intrinsic stress, inherent in an epi-poly process, strongly influences time and temperature stability of the component. Hence the use of stress-free substrate material, such as SOI, is essential.

Also rigid mounting of the component can cause external stress, as shown in Fig. 24. Package-induced stress to wafer level vacuum encapsulated MEMS resonators have been studied in [44]. The results demonstrate that with a good mechanical design it is possible to reduce the component drift below 0.1 ppm/month, which is sufficient even for high-precision applications.

There are several ways to decrease the package induced stress: an increase in the thickness of the component makes it more rigid, spring shape and suspension can be optimized to release the stress, reinforcing structures can be mounted inside the enclosure, and materials, which have nearly equal thermal expansion coefficients, can be chosen.

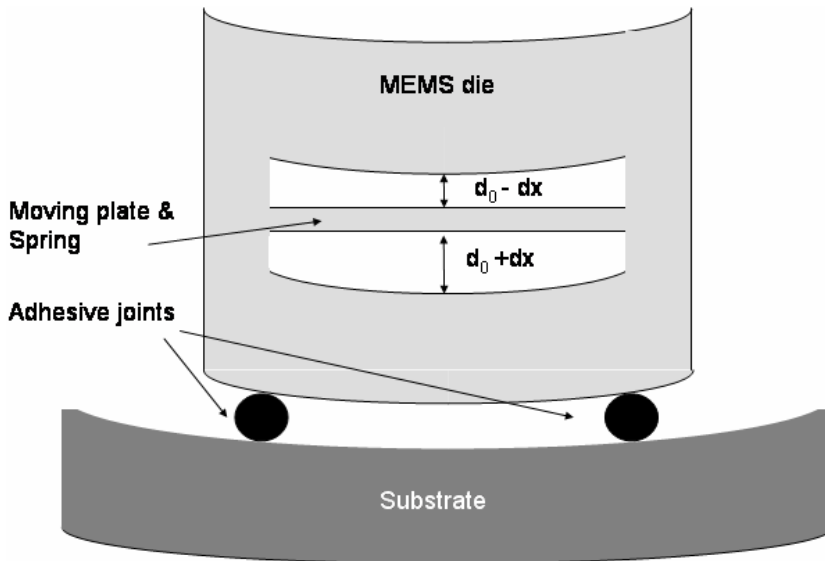


Figure 24. Gap deformation of a component due to package bending (not in scale).

3. Manufacturing and design of the components

Electrode surface quality and mechanical stress are the key factors defining the stability of a MEMS component. A new fabrication process was developed to optimize these factors. The major improvements introduced by the EMMA SOI process are the use of stress-free SOI wafers, and sputtering of both electrode surfaces by thermally and chemically stable metal. Two components were designed for the process. One component was optimized for the DC voltage reference use and the other for the AC voltage reference use.

3.1 EMMA Process

SOI was selected as the starting point of the design because of well defined device layer thickness and buried oxide layer, which was used as etch stop. Although the substrate layer was removed during the process, this manufacturing scheme is expected to give the best results in terms of stability, especially mechanical stress. Further, inertial effects are not important in SOI. A 20 μm SOI-wafer is easily available and thick enough to make the bi-metallic effect negligible. The gap height, determined by the buried oxide layer thickness, is not a critical value in the voltage reference application.

The device wafer was a SOI wafer, which had a 20 μm thick device layer and 1 μm buried oxide layer, and the substrate wafer was a 380 μm thick double side polished Si wafer. Both wafers were highly doped with boron resulting to silicon resistivity of 0.015–0.02 $\Omega\text{-cm}$. The metal electrodes were placed in wells to avoid problems in wafer bonding. The well depth and oxide thickness of the substrate wafer defined the gap height which was 1 μm .

The process consisted of four phases: 1) processing of the device (moving part) wafer, 2) processing of the substrate wafer, 3) bonding of the wafers, and 4) processing of the bonded pair as shown in Fig. 25. Low temperature fusion bonding is utilised in bonding of the sputtered wafers. After wafer bonding the handle layer of the SOI wafer and the buried oxide were removed by etching. Then the upper component surface was sputtered and patterned and finally the

moving mass was released with inductively coupled plasma (ICP) etching. The process required 10 lithography steps.

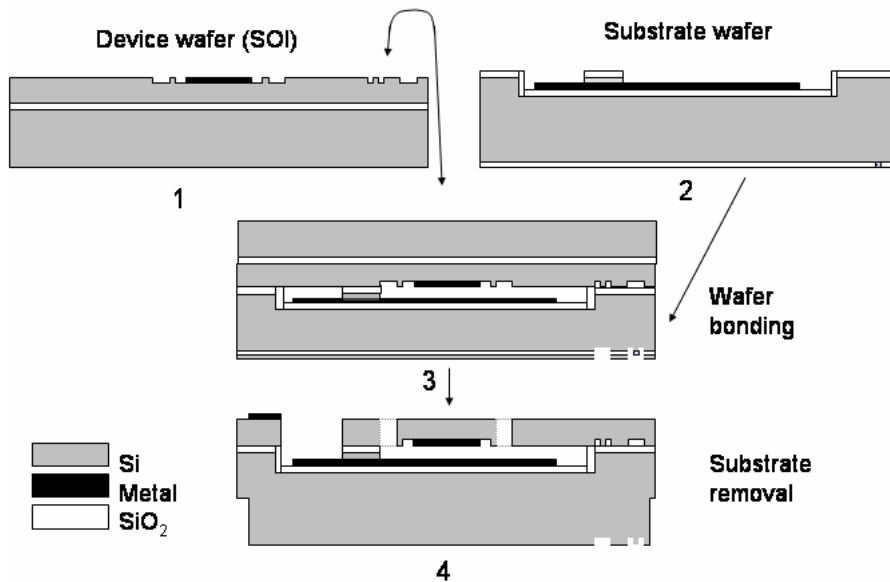


Figure 25. EMMA SOI process.

The most critical step in the process was the wafer bonding. If the surface quality of the wafers were insufficient, large non-bonded areas could be observed in optical or acoustical measurements. In the worst case, the wafers did not bond at all. To keep the surfaces in bondable condition, careful process planning and frequent cleaning procedures were required throughout the process. Metal residues had to be removed from bonding surfaces with great care.

Also, trapped gas bubbles between the bonded wafers can cause large non-bonded areas, as was experienced in the early stage of process development. Those were eventually removed by etching gas outlet grooves in the substrate wafer. The component yield from the successfully bonded areas was very good.

Hillocks on Al electrodes were observed to form even at 200 °C. Hillock formation could be reduced by sputtering a thin layer of Mo on top of the Al.

3.2 Component for the DC voltage reference

The design of the DC voltage reference component was based on the following choices and design rules:

- SOI, device layer thickness $20\ \mu\text{m}$
- Gap height $1\ \mu\text{m}$
- Released area $< 800 \times 800\ \mu\text{m}$
- Pull-in voltage $10\ \text{V}$
- Capacitance $> 1\ \text{pF}$
- Electrode material Al, Mo or MoSiN
- Double electrodes for four terminal point measurement.

3.2.1 Geometry

The seesaw component is shown in Fig. 26 and its dimensions are listed in Table 3. The seesaw was fabricated with two different spring width w_s values: $26\ \mu\text{m}$ and $34\ \mu\text{m}$. The electrode length z is measured from the edge of the seesaw.

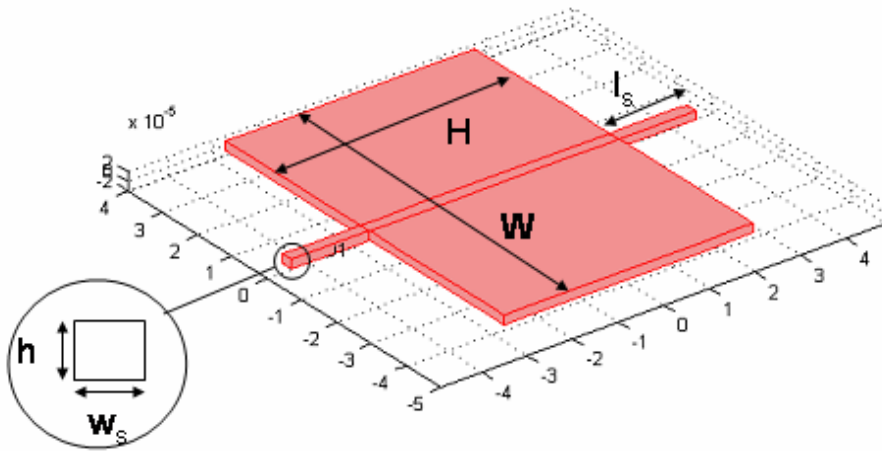


Figure 26. Seesaw design for the DC voltage reference use.

Table 3. Dimensions, materials constants, and calculated parameters for the DC voltage reference.

Dimensions and constants	Symbol	Value	Calculated parameters	Symbol	Value
Plate thickness	$h = 2a$	20 μm	Capacitance ($x = 0$)	C_0	1.22 pF
Spring length	l_s	180 μm	Pull-in voltage	V_{pi}	9.7 (19.4) V
Spring width	$w_s = 2b$	26 (34) μm	Resonance frequency	f_{res}	27 (54) kHz
Plate length	W	800 μm	Mass	m	0.02 μg
Plate width	H	550 μm	Spring constant	k	1.8 (13) kN/m
Electrode length	z	250 μm	Momentum of inertia	I	$1.12 \times 10^{-15} \text{ kgm}^2$
Gap	d	1 μm	Center of the electrode	C	275 μm
Vacuum permittivity	ϵ_0	$8.85 \times 10^{-12} \text{ J/K}$	Electrode surface area	$A_{\text{el}} = H \times z$	0.14 mm^2
Si density	ρ	2330 kg/m^3	Plate surface area	$A = H \times W$	0.44 mm^2

3.2.2 Eigencurve

The calculated eigencurve of the seesaw component is shown in Fig. 27. The pull-in point corresponds to the maximum of the curve, $V_{\text{pi}} \approx 9.7 \text{ V}$ for the 26 μm thick spring and $V_{\text{pi}} \approx 19.4 \text{ V}$ for the 34 μm thick spring.

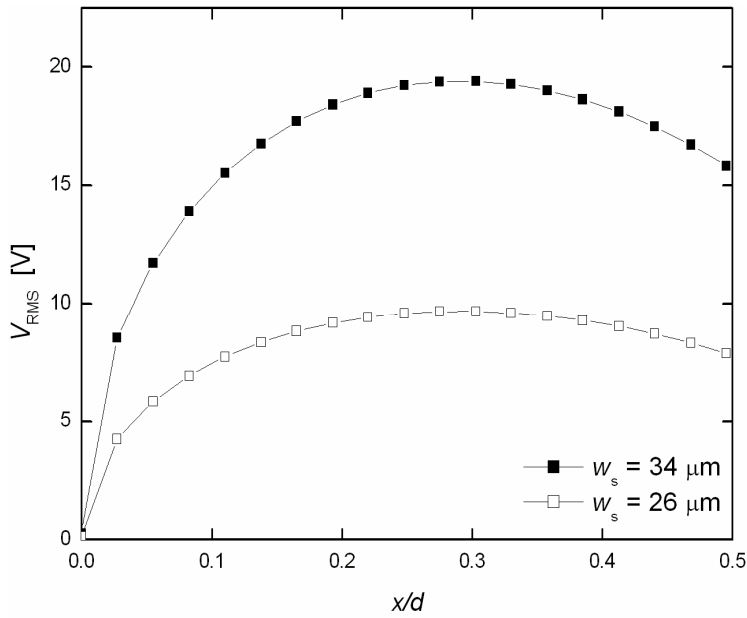


Figure 27. Eigencurve of the seesaw component as a function of deflection x divided by gap d .

3.2.3 FEM simulations

Ansys 7.0 was used to simulate the moving plate deflection due to the electrostatic force by an external voltage source and to calculate the resonance frequencies for the eigenmodes of the moving plate modals. Since Ansys is not a multiphysical program, the voltage (or electrostatic force) could not be applied into the model as such. It was assumed that the voltage causes a uniform pressure P on the electrode according to equation $P = F_e / A$, where F_e is calculated from Eq. (2). The simulation parameters used are listed in Table 4, and the boundary conditions are displayed in Fig. 28. The analytical deflection values and simulated values are compared in Fig. 29. The results agree quite well. The simulated deflection values are larger than analytically calculated because the simulation takes into account the silicon deformation at the spring anchoring areas.

Table 4. Ansys model parameters.

Materials parameters	Value	Calculation parameters	
Young modulus	130 GPa	Element type	SOLID92
Poisson ratio	0.27	Number of elements	2691
Shear modulus	66 GPa		

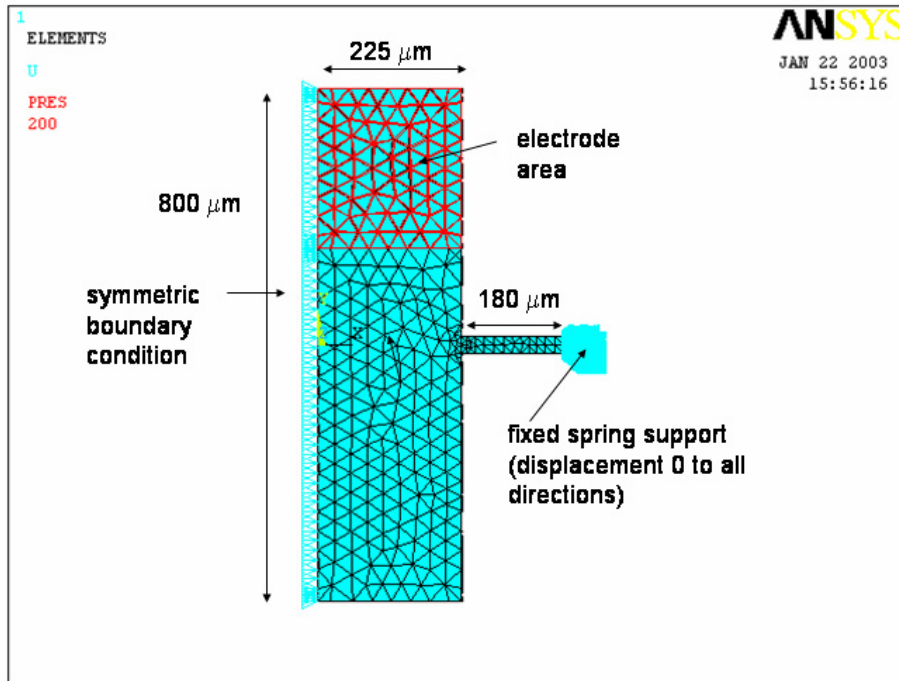


Figure 28. The boundary conditions used in the simulations.

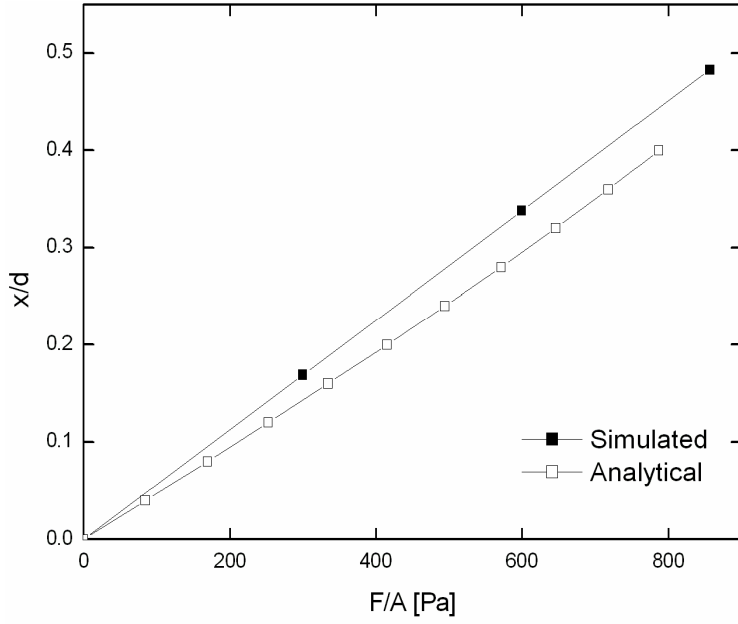


Figure 29. Analytically calculated deflection values for the seesaw as a function of the applied voltage compared against simulation results (spring width 26 μm).

3.2.4 Resonance frequency

The lowest mechanical resonance frequency of the seesaw component can be calculated from [24]

$$f_m = \frac{1}{2\pi} \sqrt{\frac{k}{I}} \quad (52)$$

where the moment of inertia I is

$$I = m \left[\frac{W^2 + h^2}{12} \right]. \quad (53)$$

The theoretical value for the resonance frequency is 27.1 kHz and the simulated value is 23.6 kHz. The first four modals and their characteristic frequencies are shown in Fig. 30.

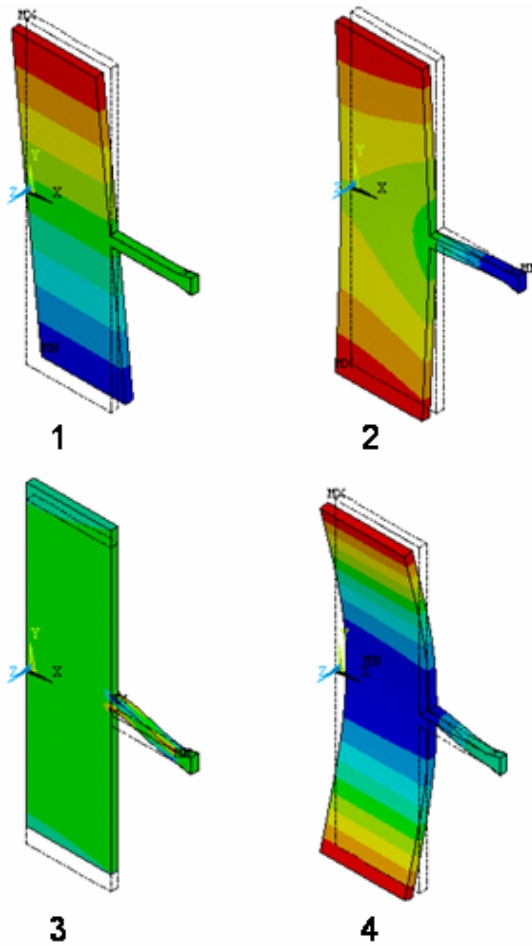


Figure 30. The first four modals of the seesaw component. The corresponding characteristic frequencies are 23.6 kHz, 71.9 kHz, 137.6 kHz, and 276.6 kHz.

3.2.5 Electrodes

The upper electrode of the seesaw component is a simple rectangle whereas the substrate wafer electrodes are divided as shown in Fig. 31. The two sections in the middle are the sense electrodes for displacement control (3 and 4). The top electrodes (1 and 2) are used for actuating the seesaw to the pull-in position while the other electrodes (5 and 6) are grounded. The effective built-in voltage (V_{bie}), *i.e.* the contact potential difference of the silicon-metal junction V_{bi}

together with the voltage V_c due to charges on the native oxide layers, can be compensated by splitting the actuation electrode into two equal sections and applying slightly different voltages with opposite polarity on the electrodes. If a positive voltage V_p is applied to electrode 1 and a negative voltage V_n is applied to electrode 2, so that $V_p = V_0 + V_{\text{bie}}$ and $V_n = -V_0 + V_{\text{bie}}$, with V_0 being the average of positive and negative pull-in voltage values, the electrostatic force F_e , $F_e \propto V_p^2 + V_n^2 \approx 2V_0^2$, is independent of V_{bie} in the first order.

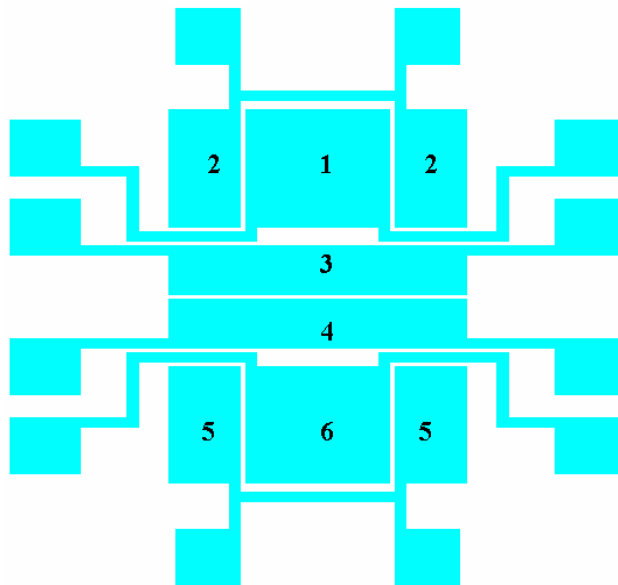


Figure 31. Divided substrate wafer electrodes enable effective built-in voltage compensation.

3.2.6 Component characteristics

The average nominal capacitance (electrodes 1 and 2 together, see Fig. 31) of the components was measured to be about 1.4 pF and the pull-in voltages varied between 6...14 V. The average built-in voltage was about -0.7 V (low potential contacted to the moving electrode). The C - V curve of a seesaw component is shown in Fig. 32.

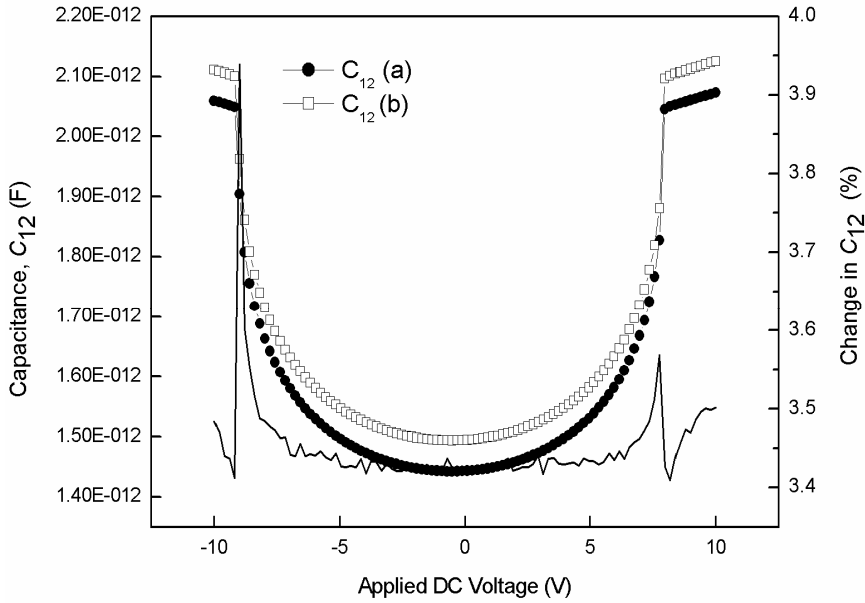


Figure 32. The characteristic C - V curves (a and b) of a component showing the measured pull-in voltage and the effective built-in voltage (the shift of the minima from 0 V). Curve b was measured after curve a and the difference of the curves is also shown (on the right hand side).

3.3 Component for the AC voltage reference

The component for the AC voltage reference was manufactured at the same time (on the same wafer) as the DC reference component. Hence the same design rules applied. The AC voltage component did not need the counter-electrode for the feedback, hence it is advantageous to utilise the whole released area for the work capacitance and hence the translational mode of operation was selected.

3.3.1 Geometry

The round component for the AC voltage reference is shown in Fig. 33 and the corresponding dimensions are displayed in Table 5. There were two variations of the sensor regarding the spring width w_s : 20 μm and 30 μm . All the calculations are done accordingly.

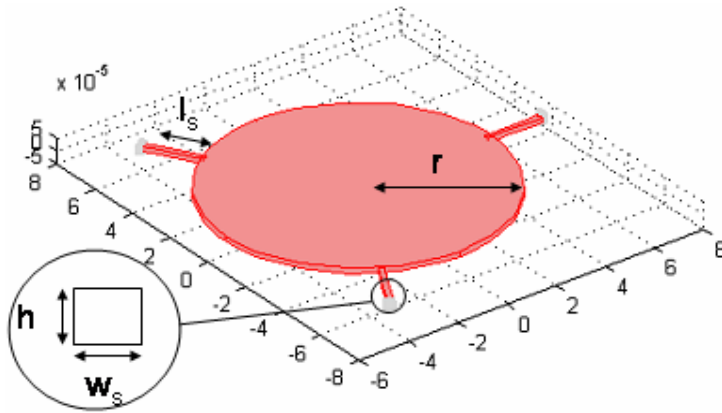


Figure 33. Round component for the AC voltage reference.

Table 5. Component dimensions, materials constants and analytically calculated characteristics.

Values	Symbol	Value	Calculated values	Symbol	Value
Plate thickness	h	20 μm	Capacitance	C_0	4.45 pF
Radius	r	400 μm	Pull-in voltage	V_{pi}	15.4 (18.8) V
Spring length	l_s	260 μm	Spring constant	k	3.5 (5.3) kN/m
Spring width	w_s	20 (30) μm	Mass	m	0.024 μg
Gap	d	1 μm	Surface area	A	0.5 mm^2
Si density	ρ	2330 kg/m^3	Resonance frequency	f_m	61 (74) kHz
Young's modulus	E	131 GPa	Deflection due to gravity	x	0.7 \AA

3.3.2 Eigencurve

The calculated eigencurve for the round component is shown in Fig. 34. The voltage V_{RMS} as a function of deflection x is displayed for the two different spring width values $w_s = 20 \mu\text{m}$ and $w_s = 30 \mu\text{m}$.

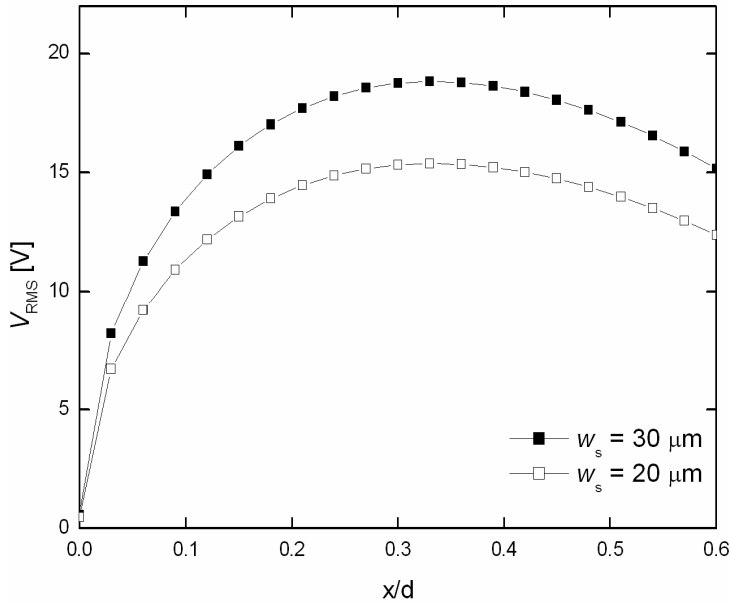


Figure 34. Eigencurve of the round component.

3.3.3 FEM simulations

Ansys 7.0 was used to simulate the component deflection by an external voltage and find out the moving plate modals and their characteristic frequencies. The simulation model used is shown in Fig. 35 and the simulation parameters are listed in Table 6. The simulated deflection values and analytically calculated values are compared in Fig. 36. The simulated deflection values for a component, the spring width of which is $30 \mu\text{m}$, approximately equals the values analytically calculated for a component, which has $20 \mu\text{m}$ wide springs. The simulation gives larger deflection values because it takes into account the silicon deformation at the spring anchoring points. Also the analytical equation used for

the deflection calculations is known to be too stiff, *i.e.* it gives too small deflection values.

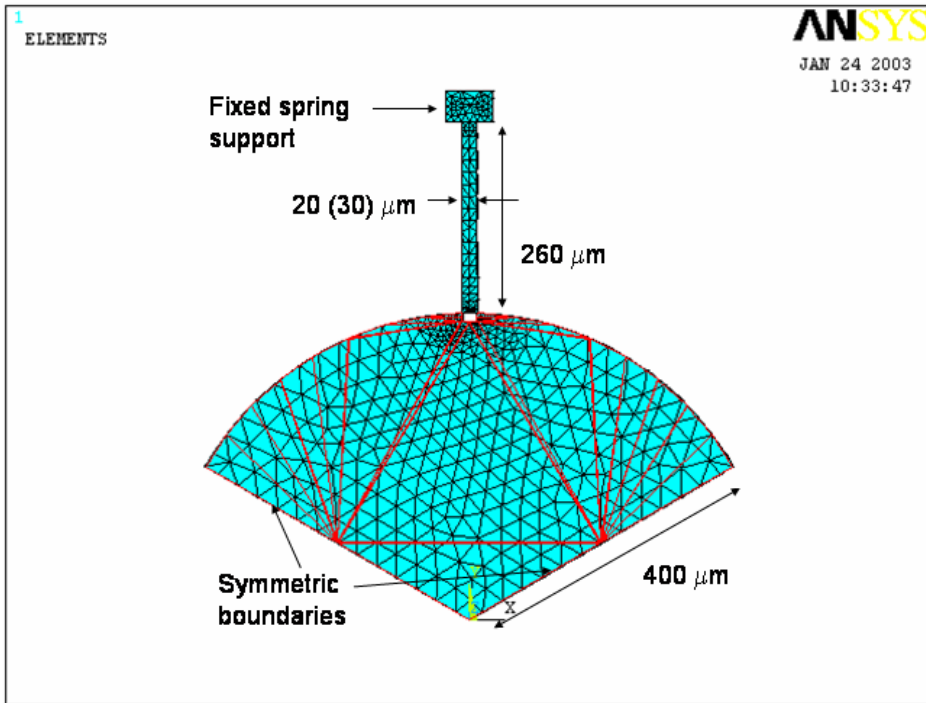


Figure 35. FEM model for the round component.

Table 6. Ansys model parameters.

Material parameters	Value	Calculation parameters	Value
Young modulus	130 GPa	Element type	SOLID187
Poisson ratio	0.27	Number of elements	2576
Shear modulus	66 GPa	Number of nodes	5157

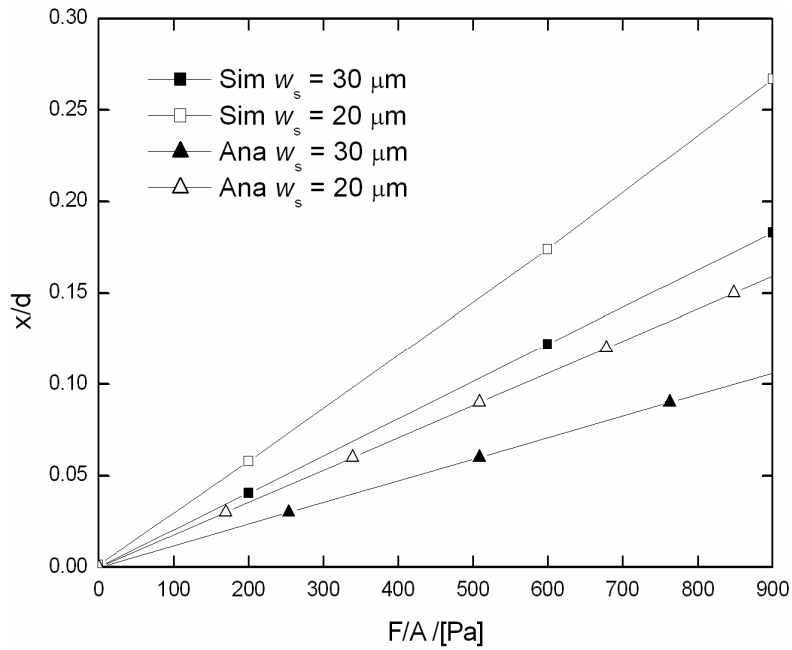


Figure 36. Analytical plate deflection compared to simulated values for two components, the spring widths of which are $w_s = 20 \mu\text{m}$ and $w_s = 30 \mu\text{m}$.

The first four characteristic modals are displayed in Fig. 37.

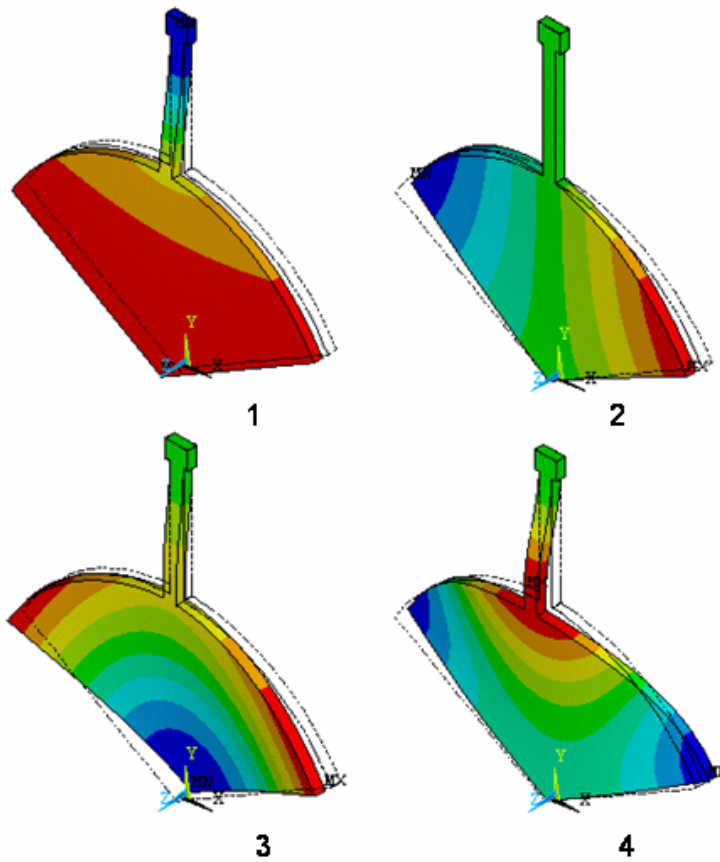


Figure 37. The first four modals of the round component. The corresponding characteristic frequencies are 53.5 kHz, 145 kHz, 442 kHz, and 606 kHz.

Also the deflection due to gravity was simulated with Ansys. It was 1.35 Å for $w_s = 20 \mu\text{m}$ and 0.9 Å for $w_s = 30 \mu\text{m}$, which are slightly higher than the analytically calculated values 0.67 Å and 0.45 Å.

3.3.4 Electrodes

The substrate wafer electrode for the round component is displayed in Fig. 38. There is one central electrode and a 10 μm thick guard electrode around it. The guard electrode suppresses the stray field between the capacitor plates. Double electrodes are designed for four terminal point measurement connections. The two outermost connectors are connected to the guard and the two innermost to the electrode.

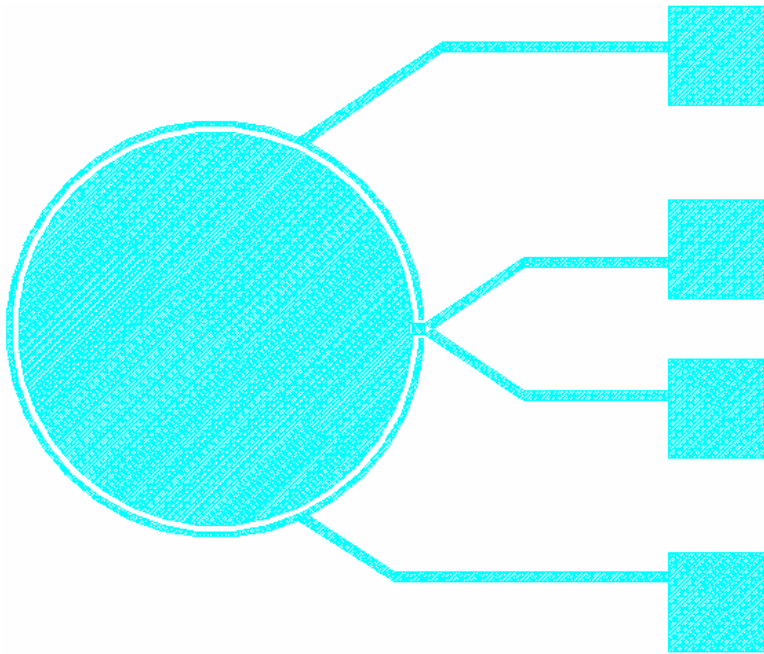


Figure 38. The substrate wafer electrode for the round component.

3.3.5 Component characteristics

The average of the nominal capacitance was measured to be about 5.2 pF and the pull-in voltages varied between 7...16 V for the round components. The built-in voltage was about -0.7 V.

3.4 Stability of the component

The component stability comprises of electrical stability, mechanical stability and stability against changes in environmental conditions. The same considerations apply both to the DC voltage reference component and to the AC voltage reference component and are hence discussed together.

3.4.1 Electrical stability

When a MEMS component is actuated with a DC voltage, the electrostatic charging will cause the reference voltage drift. This can be avoided by using AC current instead of DC voltage as is experimentally demonstrated in [I]. However, even in the absence of an external DC voltage source there is a DC voltage over the component due to the contact potential difference of the silicon-metal junction and charging of the dielectric layer as discussed in Section 2.5. In the case of DC voltage actuation, it is impossible to distinguish the different DC components from each other. The additional DC components due to the built-in voltage and charging will simply reduce the reference voltage value. However, if the component is actuated with a AC current $I(t) = \hat{I} \sin \omega t$ V_{AC} , and there is also a DC component present, V_{DC} , the force balance equation is

$$\frac{\hat{I}^2}{2\varepsilon A \omega^2} \cos^2(\omega t) + \frac{1}{2} V_{DC}^2 \frac{\varepsilon A}{(d-x)^2} = kx . \quad (54)$$

V_{DC} is a sum of all DC terms effecting on the component

$$V_{DC} = V_{bi} + V_C + V_{bias} , \quad (55)$$

where V_{bi} is the built-in voltage, V_C is the voltage due to charges on the dielectric layers, and V_{bias} is the externally applied DC bias voltage. Also, surface effects can contribute to the DC voltage term. For example, a thin layer of process residual on the top of the electrode surface can change the surface potential of the metal.

Assuming that the angular frequency of the oscillation, ω , is much higher than the component mechanical resonance frequency, the RMS voltage V_{AC} across the plate is (see Eq. (23))

$$V_{AC} = \frac{\hat{I}(d-x)}{\sqrt{2\omega\varepsilon A}} = \sqrt{\frac{2k}{\varepsilon A} (d-x)^2 x - V_{DC}^2} . \quad (56)$$

The maximum of V_{AC} , *i.e.* the reference voltage, can be calculated from $dV_{AC}(\hat{I})/d\hat{I} = (dV_{AC}(x)/dx)(dx/d\hat{I}) = 0$ Since $dx/d\hat{I} \neq 0$, the maximum is reached

when $dV_{AC}(x)/dx = 0$, which occurs at $\hat{I} = (3/\sqrt{2})\omega\varepsilon AV_{pi}/d$ (or $x = d/3$). The maximum of V_{AC} is

$$V_{AC}^{\max} = \sqrt{V_{pi}^2 - V_{DC}^2}. \quad (57)$$

Since $V_{DC} \ll V_{AC}$ small time variations ΔV_{DC} of the V_{DC} can be described as $V_{DC} = V_{DC,0} + \Delta V_{DC}$, where $V_{DC,0}$ is a constant, and Eq. (57) can now be expressed as

$$V_{AC}^{\max} = V_{pi} - \frac{V_{DC,0}^2}{2V_{pi}} - \frac{V_{DC,0}}{V_{pi}} \Delta V_{DC} \quad (58)$$

Equation (58) demonstrates that selecting $V_{DC,0} = 0$, small changes in the DC voltage, ΔV_{DC} , have no effect on the reference voltage in the first order.

3.4.2 Packaging

Two different packages were experimented with: a TO-8 can and a LTCC package as shown in Fig. 39. TO-8 can was selected because it was easily available and the equipment for hermetic enclosing in a nitrogen atmosphere existed. The LTCC package was expected to induce less mechanical stress to the MEMS component due to temperature changes since the linear coefficient of temperature expansion is about 6 ppm/°C, *i.e.* close to that of silicon (3 ppm/°C). However, the hermetic enclosing of the LTCC packages failed, hence a comparison between the LTCC and the TO-8 could not be made. Also, that was concluded to be the major reason why the stability of the component did not reach the level of the VTI hermetically packaged component. The stability of the AC voltage reference was measured to be ± 60 ppm in 14 hours [II] using the round component while the stability was measured to be ± 1 ppm in 22 days [V] using the VTI component. The readout electronics and the measurement setup were improved for the latter measurement complicating the direct comparison of these results.

The component was attached in the package using a small drop of soft adhesive in one corner. Also conductive silver epoxy was tested in order to ground the substrate wafer. Al bond wires were used for electric contacts.

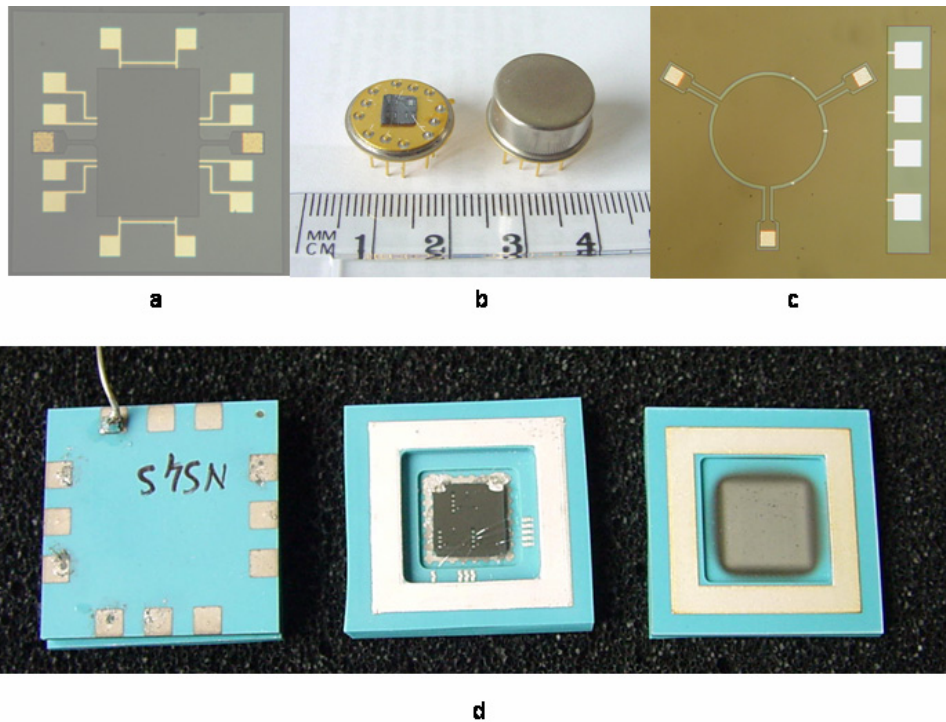


Figure 39. a) Photograph of a seesaw component, b) component mounted in a TO-8 can and hermetically enclosed TO-8 can, c) photograph of a round component, and d) LTCC package for the seesaw component.

3.4.3 Stability against changes in the environmental conditions

Calibration standards, like voltage references, are usually operated in a room environment. Still, the device is subject to modest changes in temperature, pressure, and humidity. Changes in ambient pressure can deform the package or the component structure. The mechanical stability was already discussed in Section 2.5.5. Temperature coefficient, effect of humidity and the ambient gravity for the component manufactured are discussed below.

3.4.3.1 Temperature

The temperature coefficient for a component manufactured using EMMA process, shown in Fig. 25, can be derived from the pull-in voltage equation calculated in Section 2.1.1 (Eq. 7)

$$V_{pi} = \sqrt{\frac{8}{27}} d_0 \sqrt{\frac{k}{C_0}}, \quad (59)$$

where d_0 is the initial height of the gap, C_0 the initial capacitance and k the spring constant. The gap in the EMMA process is determined by the depth of the cavity in the substrate wafer. The temperature dependences of the parameters above are

$$d_0(T) = d_0(1 + \alpha T), \quad (60)$$

$$k(T) = 3E(1 + \beta T)w_s(1 + \alpha T)\left(\frac{h}{l_s}\right)^3 \approx k[1 + (\alpha + \beta)T] \quad (61)$$

and

$$C_0(T) = \varepsilon \frac{A(1 + \alpha T)^2}{d_0(1 + \alpha T)} \approx C_0(1 + 2\alpha T), \quad (62)$$

where h and A are the thickness and area of the moving plate, w_s and l_s are the thickness and the length of the spring, and E is Young's modulus. The linear coefficient of thermal expansion for Si and the temperature coefficient of Young's modulus are α ($= 2.6 \times 10^{-6}/^\circ\text{C}$) and β ($= -65 \times 10^{-6}/^\circ\text{C}$) respectively. The temperature dependence of the pull-in voltage can now be calculated by differentiating Eq. (59). If the second order terms with respect to the temperature T are neglected the result is

$$\begin{aligned} \frac{\partial V_{pi}}{\partial T} &= V_{pi} \left(\frac{1}{d_0} \frac{\partial d_0}{T} + \frac{1}{2k} \frac{\partial k}{T} - \frac{1}{2C_0} \frac{\partial C_0}{T} \right) \approx V_{pi} \left(\frac{1}{2}(\alpha + \beta) - \frac{1}{2}\alpha \right) \quad (63) \\ &= V_{pi} \frac{\beta}{2} \end{aligned}$$

Theoretically the temperature coefficient of the pull-in voltage, about -33 ppm/°C, is determined by the temperature coefficient of the Young's modulus. However, the measured temperature coefficient of the AC reference voltage was about -140 ppm/°C for the round component and -240 ppm/°C for the VTI component [III]. In the case of the round component it was assumed that the major part of the temperature coefficient arises from the component mounting. The VTI component was resting on the top of a TO-8 can and connected to the package only via the bond wires. It is assumed that the higher temperature coefficient of the VTI component is dominated by the component bending due to the different temperature coefficients of silicon and glass.

The theoretical temperature coefficient calculated above is not the ultimate limit since it is possible to design a component, where temperature coefficients arising from different sources cancel each other resulting in a negligible temperature coefficient. For example [53] presents a RF MEMS capacitor utilizing a compensation structure to eliminate the effect of intrinsic and thermal stress.

3.4.3.2 Humidity

Open capacitive structures are very sensitive of changes in humidity so that they are even used as humidity sensors [2]. Especially silicon surface is very hydrophilic unless cleaned with hydrofluoric acid [31]. Hence the components for the voltage reference application need to be packaged hermetically. However, even with hermetic package, there are residuals of process chemicals inside the component enclosure. Their adsorption and desorption on the surfaces of the component electrodes can cause noise or drift [30]. The importance of vacuum encapsulation has been demonstrated using silicon microresonators [43]. The long term stability (df/f) of the resonator was improved from about 40 ppm below 1 ppm during 42 days by packaging the component in vacuum. The relative humidity was 20...35 RH % during the measurement period.

3.4.3.3 Gravity

Depending on the moving plate suspension and position, ambient gravity can decrease the gap between electrodes. The effect of gravity on the reference voltage has already been calculated in Section 2.1.1.4 and is presented in Eq. (25). The change in the reference voltage V_{ref} is

$$V_{\text{ref}} = V_{\text{pi}} \left(1 - \frac{F_{\text{m}}}{kd} \right)^{\frac{3}{2}}, \quad (64)$$

where V_{pi} is the pull-in voltage, F_{m} the force due to gravity acting on the moving mass m , $F_{\text{m}} = mg$, and g is the constant of gravity. The change of the reference voltage is -216 ppm for a typical component positioned and suspended as shown in Fig. 3. Component parameters given in the Table 5 were used in the calculation.

4. Readout electronics

The readout electronics is important to the overall device performance. A good review is given in [23]. If not carefully designed, it can limit the performance and the range of applicability of the MEMS component. A capacitive readout has a high resolution and low power consumption, which makes it suitable for this purpose. Usually the displacements to be detected are in the order of nanometers. The corresponding capacitance changes are typically in the order of femtofarads which can be resolved with a $4.0 \text{ aF} / \sqrt{\text{Hz}}$ resolution even with a commercial capacitive readout circuit [54]. However, when ultimate stability and sensitivity is required, custom made electronics is necessary. Two dedicated electronics, one for the DC voltage references and one for the AC voltage references, were designed and manufactured.

4.1 DC voltage reference

A block diagram of the DC voltage reference electronics utilizing feedback is displayed in Fig. 40. It is designed for the seesaw component shown in Fig. 26. A DC voltage is connected to the electrodes on one edge (C_1 and C_2) to actuate the component, while the electrodes on the other edge (C_5 and C_6) are grounded. The DC voltage on electrodes C_1 and C_2 is adjusted by the feedback loop to keep the component at the pull-in point and this voltage is the reference voltage. The plate displacement is detected by a capacitive bridge formed by the electrodes in the middle (C_3 and C_4).

The plate displacement could be detected using one capacitor only, but it is advantageous to use two capacitors since the electrostatic force acting on the plate, due to the position detection voltage V_{ext} , can be minimized. By selecting equal values for the resistors $R_1 = R_2$ results to voltage values

$$V_1 = \frac{1-x/d}{1+x/d} V_{\text{ext}} \text{ and } V_2 = -V_{\text{ext}} \quad (65)$$

on capacitors C_3 and C_4 respectively. Here x is the plate deflection at the position detection point as shown in Fig. 40. The electrostatic forces, F_1 and F_2 , caused by the position detection voltage V_{ext} on electrodes C_3 and C_4 are

$$F_1 = \frac{C_m V_1^2}{d(1-x/d)^2} \text{ and } F_2 = \frac{C_m V_2^2}{d(1+x/d)^2}, \quad (66)$$

assuming that C_3 and C_4 are equal in size and their nominal capacitance is C_m . At the pull-in point $x_{pi} = d/3$ the forces balance each other, i.e. $F_1 = F_2$.

Also, if the voltage V_{ext} varies with time, the amplitude ratio V_1/V_2 remains unchanged, which improves the displacement detection accuracy. Hence the plate displacement is determined only by the voltages over C_1 and C_2 .

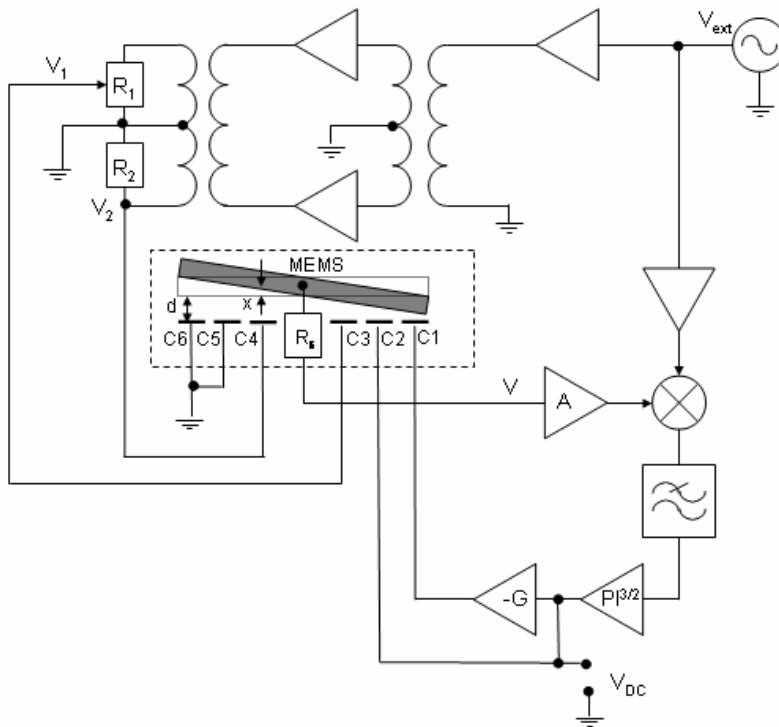


Figure 40. An electronics block diagram of a DC voltage reference based on feedback control.

In order to compensate the built-in voltage and minimize the component drift, the component is actuated to the pull-in point using slightly different voltages of opposite polarity on the electrodes C_1 and C_2 , as discussed in Section 3.2.5. The actuation voltage difference is controlled by gain G .

The voltage V at the moving plate is zero at the pull-in point $x = x_{pi}$. If the plate deflects from the pull-in point, there will be a voltage and hence a current through the silicon spring, the resistivity of which is R_s . The current will be amplified by A and the output voltage of A is combined with the reference voltage from the bridge oscillator V_{ext} by a mixer. The output of the mixer is a DC voltage with superimposed harmonic components of the input voltages. The harmonics are filtered out using a low pass filter leaving only a DC signal. This is fed to the $PI^{3/2}$ controller [55], which restores the pull-in displacement by adjusting the voltage V_{DC} , which is the DC reference voltage. A photograph of the electronics is shown in Fig. 41.



Figure 41. Photograph of the DC voltage reference.

The circuit model for the electronics is shown in Fig. 42, which takes also into account the parasitic capacitances C_{p3} and C_{p4} , mainly arising from the spring attachment points (see Section 2.3.3). In that case the voltage ratio V_1/V_2 should be adjusted from $1/2$ in order to remain the voltage V zero at the moving plate. If the AC readout voltages are $V_1 = rV_{ext}e^{j\omega}$ and $V_2 = -V_{ext}e^{j\omega}$, the voltage division ratio r should now be

$$r = \frac{\frac{3}{4}C_m + C_p}{\frac{3}{2}C_m + C_p}, \quad (67)$$

assuming that the parasitic capacitances are equal, $C_{p3} = C_{p4} = C_p$. In that case the force balance $F_1 = F_2$ is not exactly true anymore unless C_p is negligible. For example if $C_p = C_m/2$, $F_1 / F_2 = 1.5$. Hence the detection voltage V_e will cause an error in the pull-in voltage V_{pi} . The error can be minimized by using as small a detection voltage as is feasible and minimizing the component parasitic capacitance.

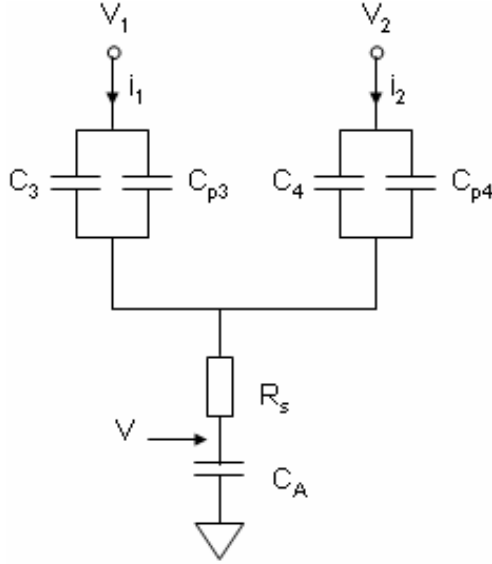


Figure 42. Circuit model for the readout electronics.

The voltage V at the moving plate can easily be derived:

$$V = \frac{(C_3 + C_{p3})V_1 + (C_4 + C_{p4})V_2}{(C_3 + C_{p3} + C_4 + C_{p4})(1 + j\omega R_s C_A) + C_A}, \quad (68)$$

where C_A is the amplifier input capacitance. Near the pull-in point, $x=d/3+\delta x$, the capacitances C_3 and C_4 are

$$C_3 = \frac{3}{2}C_m \left(1 + \frac{3}{2} \frac{\delta x}{d}\right) \quad \text{and} \quad C_4 = \frac{3}{4}C_m \left(1 - \frac{3}{4} \frac{\delta x}{d}\right). \quad (69)$$

Inserting Eq. (69) into Eq. (68) results in

$$\frac{\text{Re}(V)}{\delta x} = \frac{9}{16} \frac{V_{\text{ext}}}{d} \frac{\left(\frac{C_A}{C_m} + 2 \frac{C_p}{C_m} + \frac{9}{4} \right) \left(\frac{9 + 10C_p / C_m}{3 + 2C_p / C_m} \right)}{\left(\frac{C_A}{C_m} + 2 \frac{C_p}{C_m} + \frac{9}{4} \right)^2 + \left(R_s \omega C_A \left(\frac{9}{4} + 2 \frac{C_p}{C_m} \right) \right)^2}. \quad (70)$$

This is the position detection transfer function $G4$ (Eq. (18), if C_p is set to zero) discussed in Section 2.1.1.3.

The parasitic capacitance and amplifier input capacitance reduce the sensitivity of the readout which is demonstrated in Fig. 43 for different parasitic capacitance C_p values and amplifier input capacitance C_A values. Typical values for the spring resistance, angular frequency, and amplifier input capacitance are $R_s = 50 \Omega$, $\omega = 628 \text{ kHz}$ and $C_A = 3 \text{ pF}$ which have been used in the calculation.

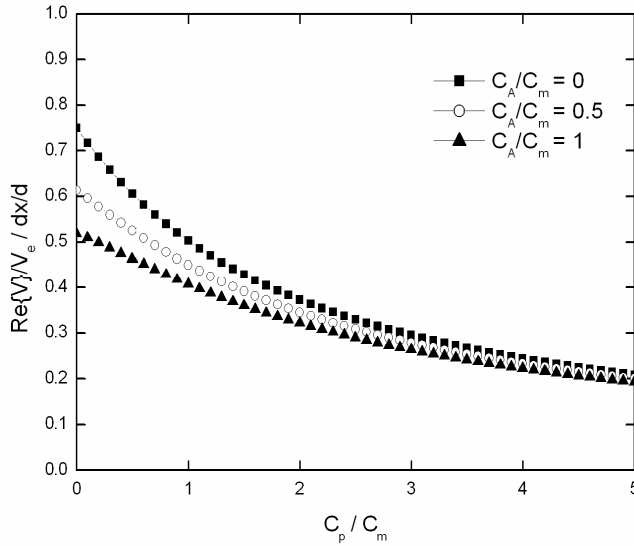


Figure 43. Relative sensitivity of the readout $\text{Re}(V)/V_e / (\delta x/d)$ as a function of the parasitic capacitance C_p for different amplifier input capacitance C_A values.

4.2 AC reference electronics

The electronics for a current actuated AC voltage reference can be realised using only a few component as show in Fig. 44. An AC voltage, the frequency of which is well above the mechanical resonance frequency, is fed to the inverting input of the main operational amplifier OA2 which acts as a voltage to current converter. The amplitude of the input current is slowly varied over the maximum point and the maximum output voltage is the AC reference voltage (the AC component of V_{out} in Fig. 44). The instrumentation amplifier IA1 isolates the source V_{AC_in} . The stability of the OA2 gain is recorded at the output of the unity gain buffer amplifier OA3. The DC bias voltage for the built-in voltage compensation is fed to the non-inverting input of OA2. A trimmer resistor is needed to find out the right DC compensation voltage, but once found, the trimmer can be replaced with a fixed resistor. Temperature, pressure and humidity are recorded during the measurement and used for the multi-regression analysis to correct the measurement data.

It has been experimentally demonstrated, that small changes in the parasitic capacitance or in the parasitic resistance over the component have no effect on the pull-in voltage [III]. Hence the stability of the electronics depends only on the stability of the MEMS component and the stability of the OA2 gain.

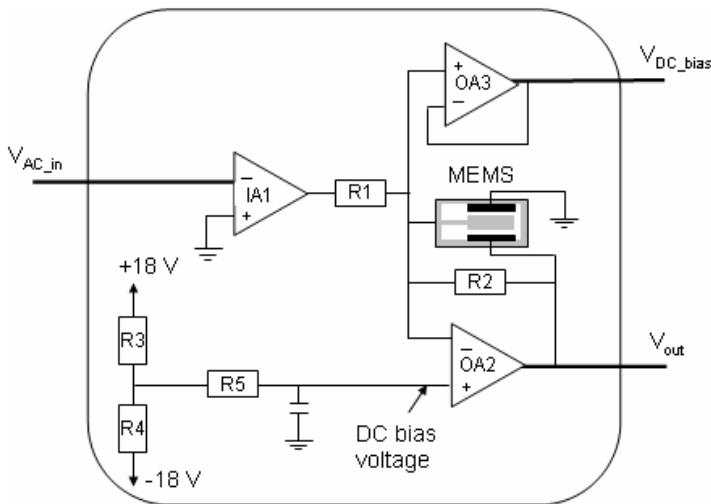


Figure 44. An electronics block diagram for the AC voltage reference.

A photograph of the readout electronics including a VTI component mounted in a TO-8 can is shown in Fig. 45.

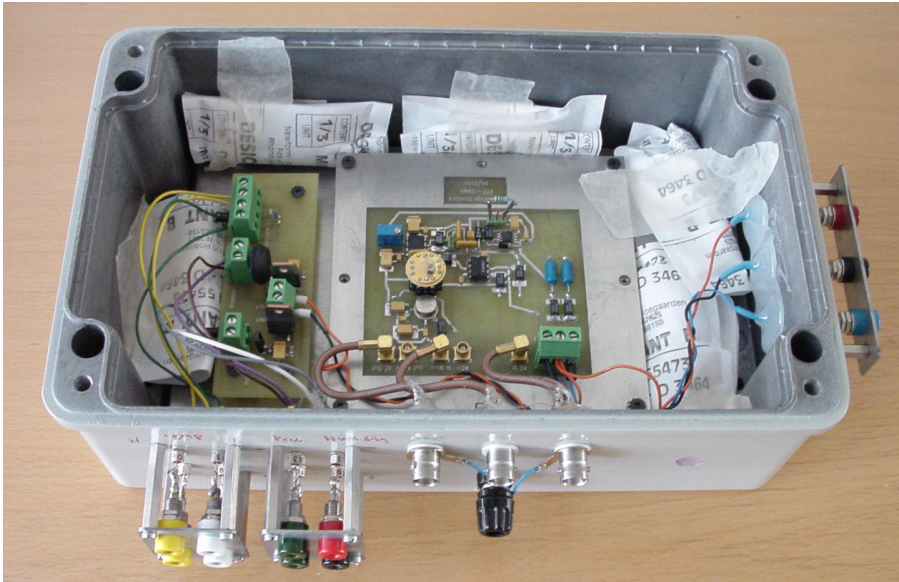


Figure 45. A photograph of the AC voltage reference including the humidity absorbing gel bags on the sides.

5. Measurement results

5.1 Stability of the DC voltage reference

The long-term stability of the DC voltage reference using a seesaw component and feedback electronics described in Section 4.1 was measured in a laboratory environment. Fig. 46 shows the measurement result. After the initial rapid change in the reference voltage the device stabilizes at approximately $60 \mu\text{V}/\text{V}$ over the next 10 hours. The result does not include any ambient temperature corrections to the measured data.

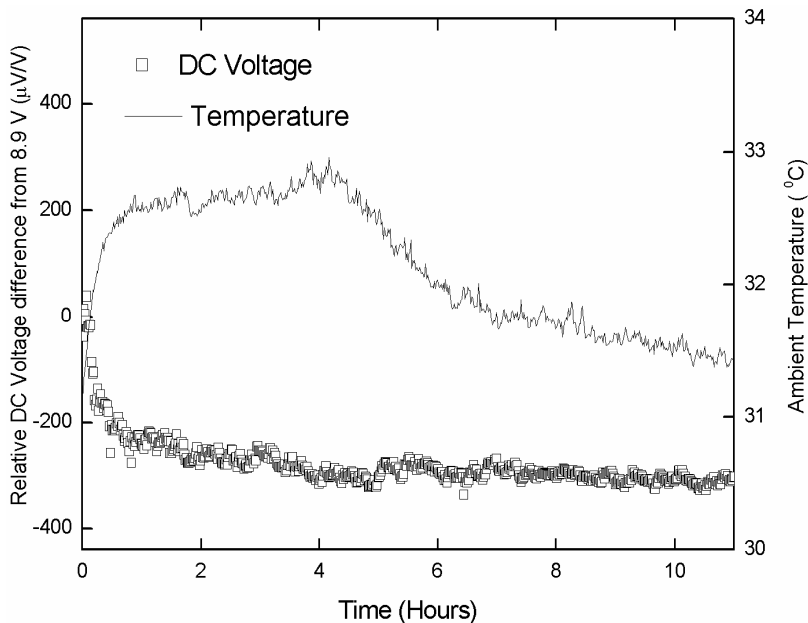


Figure 46. Long-term stability of the DC voltage reference over 11 hours. The solid curve shows the corresponding ambient temperature recorded during the measurements.

The first experimental results of the new device show an order of magnitude improvement with respect to earlier work [18]. However, the long-term stability of the reference is not sufficient for reference application. The device would still require improvements in the feedback electronics and in the component mounting as well as hermetic packaging.

5.2 Drift of the AC reference voltage

The voltage drift of the AC reference was measured when different bias voltages were applied over the MEMS component. The measurement was done in laboratory environment where the temperature varied less than 3 °C around the average value of 34 °C inside the enclosure. The bias voltage was set close to the built-in voltage value by changing the values of resistors R3 and R4 (see Fig. 44), and the AC reference voltage was monitored with an HP 3458A DVM for 4–21 days for each bias voltage setting. Two MEMS components (VTI accelerometers) were experimented: one with a thin native oxide layer (typically in the order of 1–2 nm) and the other with a 50 nm thick SiO₂ layer on top of the non-moving electrode. The non-moving electrodes of the components were coated with AlCu and the moving electrodes had an additional boron doping ($N_A = 4^{19} \text{ cm}^{-3}$). The surface areas of the electrodes were almost equal, but the spring constants (30 N/m and 105 N/m) and the gaps (5.7 μm and 2 μm) of the components (native oxide and thick oxide) were different. The measured pull-in voltage values were 9.0 V and 3.9 V respectively. The relative change of the reference voltage V_{AC} is shown in Fig. 47 for the thick oxide component. The slope of the curve is the drift rate, displayed in Fig. 48 for the thick oxide component and in Fig. 49 for the native oxide component.

Within the time span and bias voltage range used in the experiment, the drift is linear for both of the components. For the native oxide component the drift is at its minimum when the bias voltage is set to compensate the built-in voltage as explained in Section 3.4.1 and will be demonstrated in the next Section. For the thick oxide component the minimum drift is achieved at a bias voltage value of 300 mV while the built-in voltage, measured from the component $C-V$ curve, is 61 mV. This discrepancy might be related to the component mechanical drift or variation of the initial charging state of the component. Although the component was short circuited several days between the measurements, the initial charging state might have varied due to the long (de)charging time constant.

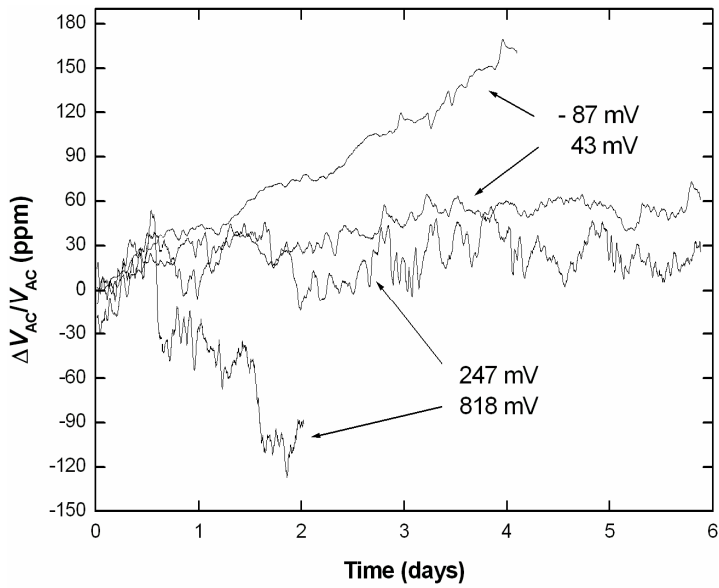


Figure 47. Measured voltage drift of the AC reference. The applied DC bias is shown in the legend.

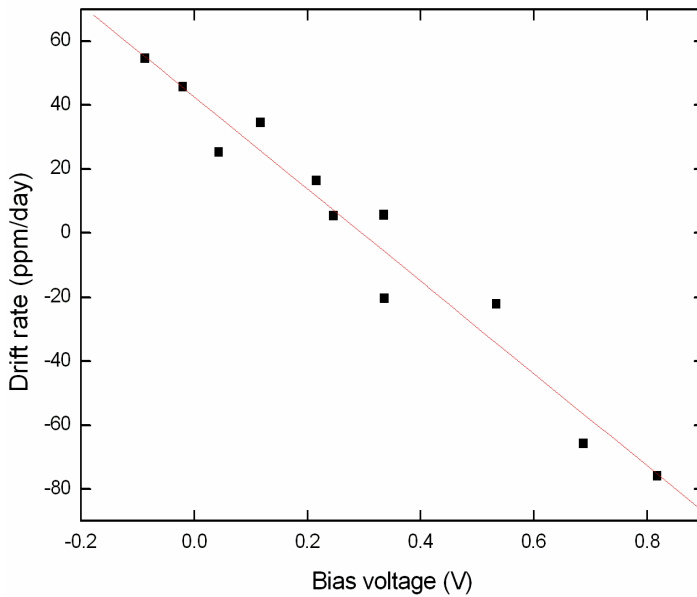


Figure 48. Measured drift rate of the AC voltage reference and a linear fit. The MEMS component was a VTI accelerometer having a 50 nm oxide layer on the non-moving electrode.

The effective built-in voltage of the thick oxide component (61 mV) compares favourably with that of the native oxide component (245 mV). However, the drift rate of the thick oxide component is approximately 20 times larger than that of the native oxide component. The built-in voltage compensation for the thick oxide component turned out to be very difficult due to the large drift rate and long time constant associated with it.

5.3 Built-in voltage compensation

The drift of the AC reference voltage due to component dielectric charging can be avoided by applying an external bias voltage which eliminates the built-in voltage over the MEMS component. The right bias voltage can be determined either from the component $C-V$ curve, as the voltage corresponding to the minimum point of the $C-V$ curve (with opposite polarity), or scanning the bias voltage of the AC reference. The bias voltage corresponding to the maximum of the reference voltage is the right compensation voltage (see Eq. 57). Figure 49 shows the measured voltage drift for a VTI component as a function of the applied bias voltage. The figure also includes the compensation voltages derived by different ways. The compensation voltage corresponding to the $C-V$ curve minimum, V_{C-V} , is -245 mV, the maximum point of the AC reference voltage, V_{AC_ref} , is -278 mV, and the zero point of the curve fitted to the measured drift rates with different bias voltages, V_{drift} , is -256 mV. The values agree fairly well especially taking into account that the original charging state of the component may have varied between the different measurements. The component was short circuited for several days between the measurement, which is enough to discharge the mobile ionic and the interface trap charges but the deep states in oxide may have time constants much longer than that.

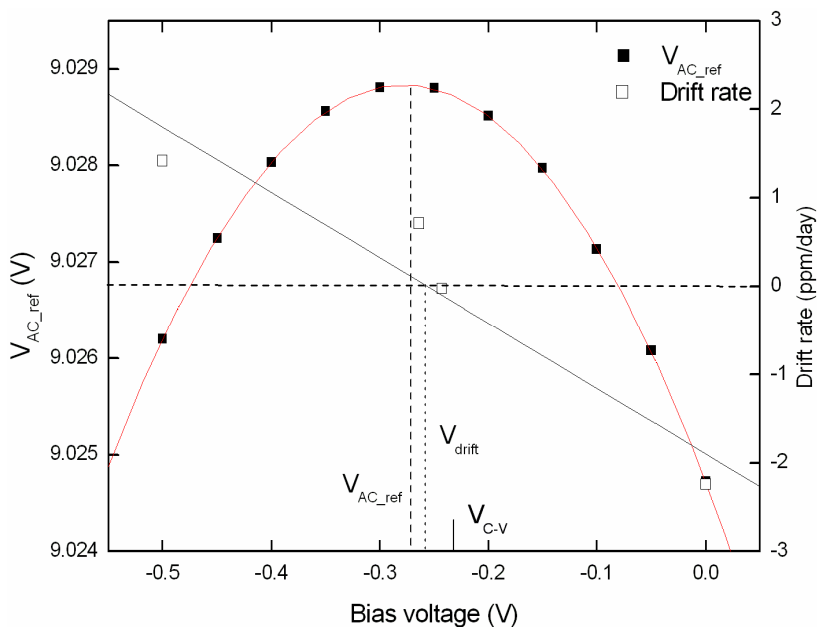


Figure 49. Measured voltage drift of the AC reference as a function of applied DC bias voltage. The C-V curve minimum, V_{C-V} , marked to the figure with the opposite polarity.

5.4 Stability of the AC voltage reference

The experimental setup for the long-term stability measurement of the AC voltage reference is shown in Fig. 50. The measurement was done at the Centre for Metrology and Accreditation MIKES. The AC voltage reference, including a VTI accelerometer as the MEMS component, was mounted on a stone table closed in a temperature stabilized chamber. The temperature varied less than $0.1\text{ }^{\circ}\text{C}$ around the average value of about $23.5\text{ }^{\circ}\text{C}$ during the 3-week measurement. The output voltage was measured using a HP 3458A DVM, the stability of which was periodically (about once in a day) checked against a Datron 4920 AC measurement standard and a Fluke 5700 A calibrator (the upper part of Fig. 50). No drift between these three devices was observed during the three-week measuring period within the scatter of about 2 ppm, which indicates that the repeatability of the DVM during the experiment was of the order of 2 ppm.

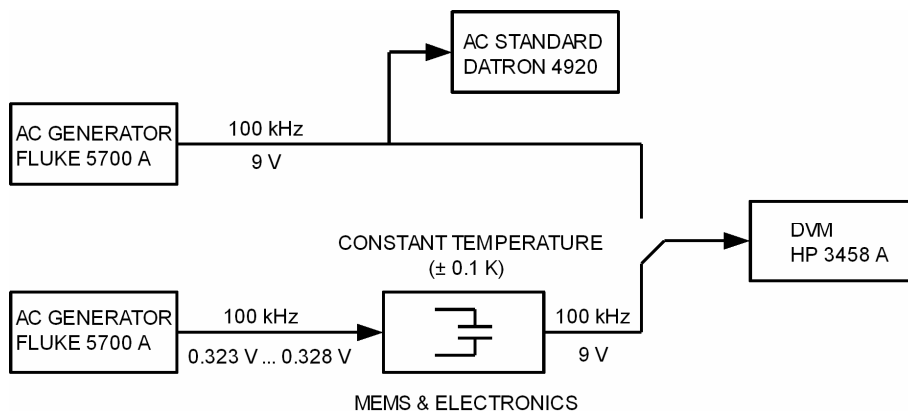


Figure 50. Measurement setup for the long-term stability measurement. The lower part is the actual measurement system, and the upper part was used for calibration of the DVM. (courtesy of MIKES).

The bias voltage was first set to the measured value of the built-in voltage -0.245 V (with opposite polarity) and fine tuned later to -0.243 V (see Fig. 49). The measurement was made by changing the amplitude of the 100 kHz driving current across the maximum point, and by recording the RMS value of the reference output voltage with the DVM for each amplitude value. A second-order polynomial fit was made to the data and the voltage at the maximum was determined. Essentially identical results, with slightly larger scatter, would have been obtained by monitoring the output voltage at a fixed amplitude of the driving current set to the pull-in point. The results are plotted in Fig. 51 after correcting the data for ambient pressure ($-6\text{ }\mu\text{V/hPa}$) and temperature ($-180\text{ }\mu\text{V/}^\circ\text{C}$). No drift could be observed in the 100 kHz output voltage of the device within the measurement accuracy of about 2 ppm . After the stability test was finished, both AC drive and DC bias (built-in voltage compensation) were disconnected but the device was kept in the temperature isolated measurement chamber. After one day the voltages were reconnected and the experiment was started again. After a relaxation period of about 8 hours , the output voltage returned to the original level within the measurement accuracy of about 2 ppm .

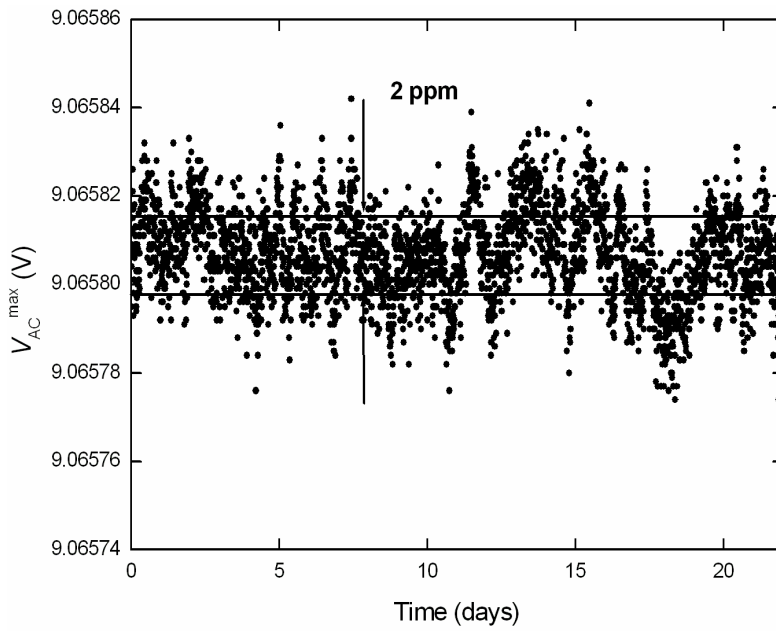


Figure 51. Long-term stability of the AC voltage reference (courtesy of MIKES).

6. Conclusions

This dissertation investigates a DC voltage reference and an AC voltage reference based on the pull-in phenomenon of a micromechanical moving plate capacitor. The main emphasis is on the device stability which is one of the main criteria of the device applicability in metrology. The stability of the AC voltage reference was improved to the ppm-level. This level of performance is sufficient for many applications.

The major achievements of this work are solving the electrostatic stability of the MEMS component by applying AC voltage actuation together with the built-in voltage compensation, and creating a new silicon-on-insulator (SOI) process which enables metallization of the moving electrode. Metal electrodes significantly increase the component stability although with increased complexity of the manufacturing process. The methods for improving the stability of MEMS components can be generally exploited in MEMS applications and the new process has already been applied in manufacturing of a MEMS magnetometer.

This work demonstrates that MEMS based voltage references can be very stable if manufactured from single-crystal silicon and mounted in a hermetic package, which causes no mechanical stress to the component. MEMS references compare favourably to the existing devices by size, price and power consumption. The value of the pull-in voltage depends on the component dimensions and can be set to a wide range of values. MEMS components can be integrated with the readout electronics, as is illustrated in Fig. 52.

MEMS based voltage references can provide a competitive alternative to the conventional voltage reference devices. However, plenty of work still remains to commercialize these devices. The manufacturing process is not suitable for mass production, mechanical design of the component could be improved and a new stress free hermetic packaging developed.

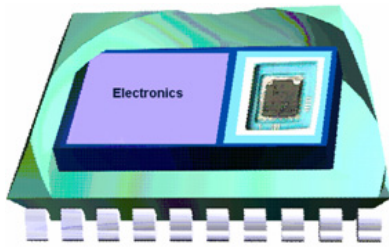


Figure 52. Future vision of the MEMS based voltage reference.

References

- [1] Maluf, N. An Introduction to Microelectromechanical Systems Engineering, Artech House, 2000, ISBN 0-89006-581-0.
- [2] Gardner, J.W. Microsensors, John Wiley & Sons, 1994, ISBN 0-471-94145-2.
- [3] Krueger, S., Müller-Fiedler, R., Finkbeiner, S. and Trah, H.-P. MST News 1/05, pp. 8–10.
- [4] Taylor, B.N. (Ed.) The International System of Units (SI). Washington, DC: U.S. General Printing Office, 1991, NBS Special Publ. 330.
- [5] Benz, S.P. and Hamilton, C.A. Application of the Josephson Effect to Voltage Metrology, Proceedings of the IEEE, Vol. 92, No. 10, Oct. 2004, pp. 1617–1629.
- [6] <http://nvl.nist.gov/pub/nistpubs/sp958-lide/html/315-318.html> (22.6.2006).
- [7] Gray, P. and Meyer, R.G. Analysis and design of analog integrated circuits, John Wiley & Sons, 2nd edition, 1994, ISBN 0-471-59984-0.
- [8] Horrowich, P. and Hill, W. The art of electronics, Cambridge University Press, 2nd edition, 1989, ISBN 0-521-37095-7.
- [9] <http://www.intersil.com/Vref/index.asp> (22.6.2006).
- [10] Klonz, M., Laiz, H. and Kessler, E. Development of Thin-Film Multijunction Thermal Converters at PTB/IPHT, IEEE Trans. Instrum. Meas., Vol. 50, Dec. 2001, pp. 1490–1498.
- [11] Wolffenbittel, R.F. and van Mullem, C.J. The Relationship Between Microsystem Technology and Metrology, IEEE Trans. Instrum. Meas., Vol. 50, Dec. 2001, pp. 1469–1474.

- [12] van Drieënhuizen, B.P. and Wolffenbittel, R.F. Integrated Micromachined Electrostatic True RMS-to-DC Converter, *IEEE Trans. Instrum. Meas.*, Vol. 44, No. 2, 1995. pp. 370–373.
- [13] van Drieënhuizen, B.P. Integrated Electrostatic RMS-to-DC Converter, Ph.D. Thesis, Delft University, 1996.
- [14] de Graaf, G., Bartek, M., Xiao, Z., van Mullem, C.J. and Wolffenbittel, R.F. Bulk Micromachined Electrostatic True RMS-to-DC Converter, *IEEE Trans. Instrum. Meas.*, Vol. 50, No. 6, Dec. 2001. pp. 1508–1512.
- [15] Kynnäräinen, J., Oja, A.S. and Seppä, H.A. Micromechanical RMS-TO-DC Converter, in *Digest, CPEM2000*, Sydney, May 2000, pp. 699–700.
- [16] Suhonen, M., Seppä, H., Oja, A.S., Heinilä, M. and Näkki, I. AC and DC Voltage Standards Based on Silicon Micromechanics, in *Digest, CPEM98*, Washington DC, July 1998, pp. 23–24.
- [17] Seppä, H., Kynnäräinen, J. and Oja, A. Microelectromechanical Systems in Electrical Metrology, *IEEE Trans. Instrum. Meas.*, Vol. 50, No. 2, Apr. 2001, pp. 440–444.
- [18] Kynnäräinen, J., Oja, A.S. and Seppä, H. Stability of Microelectromechanical Devices for Electrical Metrology, *IEEE Trans. Instrum. Meas.*, Vol. 50, No. 6, Dec. 2001, pp. 1499–1503.
- [19] Cretu, E., Rocha, L.A. and Wolffenbittel, R.F. Micromechanical Voltage reference Using the Pull-In of a Beam, *IEEE Trans. Instrum. Meas.*, Vol. 50, Dec. 2001, pp. 1504–1507.
- [20] Rocha, L.A., Cretu, E. and Wolffenbittel, R.F. Full characterisation of pull-in in single-sided clamped beams, *Sensors and Actuators, A110*, 2004, pp. 301–309.
- [21] Seeger, J.I. and Boser, B.E. Charge Control of Parallel-Plate, Electrostatic Actuators and the Tip-In Instability, *Journal of Microelectromechanical Systems*, Vol. 12, No. 5, Oct. 2003, pp. 1–16.

- [22] Rocha, L.A. Dynamics and Nonlinearities of the Electro-Mechanical Coupling in Inertial MEMS, Ph.D. Thesis, Delft University, 2005.
- [23] Senturia, S.D. Microsystem design, KluwerAcademic Publishers, 2001, ISBN 0-7923-7246-8.
- [24] Roark, R.J. and Young, W.C. Formulas for Stress and Strain, McGraw-Hill, 6th edition, 1989, ISBN 0-07-100373-8.
- [25] Nadal-Guardia, R., Dehé, A., Aigner, R. and Castañer, L.M. Current Drive Methods to Extend the Range of Travel of Electrostatic Microactuators Beyond the Voltage Pull-In Point, Journal of Microelectromechanical Systems, Vol. 11, No. 3, June 2002, pp. 255–263.
- [26] Lewis, P.H. and Yang, C. Basic Control Systems Engineering, Prentice Hall International, Inc., 1997, ISBN 0-13-744434-6.
- [27] Castañer, L.M., Pons, J., Nadal-Guardia, R. and Rodríguez, A. Analysis of the extended operation range of electrostatic actuators by current-pulse drive, Sensors and Actuators, A 90, 2001, pp. 181–190.
- [28] Veijola, T., Kuisma, H., Lahdenperä, J. and Ryhänen, T. Equivalent-circuit model of the squeezed gas film in a silicon accelerometer, Sensors and Actuators, A 48, 1995, pp. 239–248.
- [29] Veijola, T., Kuisma, H. and Lahdenperä, J. The influence of gas-surface interaction on gas-film damping in a silicon accelerometer, Sensors and Actuators, A 66, 1998, pp. 83–92.
- [30] Kovacs, G.T.A. Micromachined transducers source book, McGraw-Hill Companies Inc., 1998, ISBN 0-07-290722-3.
- [31] Franssila, S. Introduction to Microfabrication, John Wiley & Sons Ltd, 2004, ISBN 0-470-85105-8.

- [32] Kiihamäki, J. Fabrication of SOI micromechanical devices, Ph.D. Thesis, Helsinki University of Technology, 2005. VTT Publications 559. Espoo: VTT. 87 p. + app. 28 p. ISBN 951-38-6435-9; 951-38-6436-7. <http://virtual.vtt.fi/inf/pdf/publications/2005/P559.pdf>.
- [33] Cabuz, C. Tradeoffs in MEMS materials, Proc. SPIE, Vol. 2881, 1996, pp. 160–170.
- [34] Guckel, H., Burns, D.W., Visser, C.C.G., Tilmans, H.A.C. and Deroo, D. Fine-Grained Polysilicon Films with Built-In Tensile Strain, IEEE Trans. Electron Devices, Vol. 35, No. 6, 1988, pp. 800–801.
- [35] Madou, M.J. Fundamentals of Microfabrication, CRC Press LLC, 1997, ISBN 0-8493-9451-1.
- [36] Sze, S.M. Semiconductor devices, John Wiley & Sons Ltd, 2nd edition, 2002, ISBN 0-471-33372-7.
- [37] Bourgeois, C., Steinsland, E., Blanc, N. and de Rooij, N.F. Design of resonators for the determination of the temperature coefficient of elastic constants of monocrystalline silicon, in Proc. IEEE Int. Frequency Control Symp., Orlando, FL, May 1997, pp. 791–799.
- [38] Rusanen, O. Adhesives in micromechanical sensor packaging, Ph.D. Thesis, University of Oulu, 2000. VTT Publications 407. Espoo: VTT. 74 p. + app. 54 p. ISBN 951-38-5558-9.
- [39] <http://parts.jpl.nasa.gov/docs/JPL%20PUB%2099-1.pdf> (22.6.2006).
- [40] <http://www.vti.fi> (22.6.2006).
- [41] Pohjanen, J. Sähköstaattiset pintailmiöt kapasitiivisessa kiihtyvyyssanturissa, M.Sc. Thesis, Helsinki University of Technology, 2003.
- [42] Rytönen, V.-P. Built-in voltages of metal semiconductor junctions and structures, M.Sc. Thesis, Helsinki University of Technology, 2005.

- [43] Koskenvuori, M., Mattila, T., Häärä, A., Kiihamäki, J., Tittonen, I., Oja, A. and Seppä, H. Long-term stability of single-crystal silicon microresonators, *Sensors and Actuators, A* 155, 2004, pp. 23–27.
- [44] Kaajakari, V., Kiihamäki, J., Oja, A., Seppä, H., Pietikäinen, S., Kokkala, V. and Kuisma, H. Stability of Wafer Level Vacuum Encapsulated Single-Crystal Silicon Resonators, *The 13th International Conference on Solid-State Sensors, Actuators and Microsystems*, Seoul, Korea, June 5–9, 2005.
- [45] Wibbeler, J., Pfeifer, G. and Hietschold, M. Parasitic charging of dielectric surfaces in capacitive microelectromechanical systems (MEMS), *Sensors and Actuators, A* 71, 1998, pp. 74–80.
- [46] Schröder, D.K. and Babcock, J.F. Negative bias temperature instability: Road to cross in deep submicron silicon semiconductor manufacturing, *J. Appl. Phys.* 94, 2003, pp. 1–18.
- [47] Rebeiz, G.M. *RF MEMS: theory, design, and technology*, John Wiley & Sons, 2003, ISBN 0-471-20169-3.
- [48] Rashkeev, S.N., Fleetwood, D.M., Schrimpf, R.D. and Pantelides, S.T. Proton Induced Defect Generation at the Si-SiO₂ Interface, *IEEE Trans. Nucl. Sci.* 48, 2001, pp. 2086–2092.
- [49] Liu, C.-H., Lee, M.T., Lin, C.-Y., Chen, J., Loh, Y.T., Liou, F.-T., Schueffer, K., Katsetos, A.A., Yang, Z., Rovedo, N., Hook, T.B., Wann, C. and Chen, T.-C. Mechanism of Threshold Voltage Shift (ΔV_{th}) Caused by Negative Bias Temperature Instability (NBTI) in Deep Submicron pMOSFETs, *Jpn. J. Appl. Phys.* Vol. 41, 2002, pp. 2423–2425.
- [50] van Spengen, W.M., Puers, R., Mertens, R. and De Wolf, I. A comprehensive model to predict the charging and reliability of capacitive RF MEMS switches, *J. Micronech. Microeng.* 14, 2004, pp. 514–521.
- [51] Mizsei, J. Ultra-thin insulator covered silicon: potential barriers and tunnel currents, *Solid-State Electronics*, Vol. 46, 2002, pp. 235–241.

- [52] Zafar, S., Lee, B.H., Stathis, J., Callegari, A. and Ning, T. A Model for negative Bias Temperature Instability (NBTI) in Oxide and High κ pFETs, IEEE VLSI Symp., 2004, pp. 208–209.
- [53] Nieminen, H., Ermolov, V., Silanto, S., Nybergh, K. and Ryhänen, T. Design of a Temperature-Stable RF MEM Capacitor, Journal of Microelectromechanical systems, Vol. 13, No. 5, October 2004, pp. 705–714.
- [54] <http://www.irvine-sensors.com/pdf/MS3110%20Datasheet%20USE.pdf> (22.6.2006).
- [55] Kiviranta, M. and Seppä, H. DC-SQUID electronics based on the noise cancellation scheme, IEEE Transactions on Applied Superconductivity, Vol. 5, No. 2, June 1995, pp. 2146–2148.

*Appendix V of this publication is not included in the PDF version.
Please order the printed version to get the complete publication
(<http://www.vtt.fi/publications/index.jsp>)*

Author(s) Kärkkäinen, Anna-Maija			
Title MEMS based voltage references			
Abstract <p>Microsystem technology has enabled a new field in metrology. Voltage references based on MEMS, microelectromechanical systems, are unique in two different ways. First, they are small in size and cost-efficient since they are manufactured using equipment and facilities developed for integrated circuit mass production, where a large number of components are processed on a single silicon wafer. Second, the principle of operation of a MEMS voltage reference is outstanding from the physics point of view. They are electrical references, but their stability is based on material properties of single crystal silicon which is one of the most stable materials. The level of performance of electrical instruments, which utilize voltage references as their key components, like digital multimeters, data logging systems, and calibrators, is proportional to the stability of the voltage reference.</p> <p>This dissertation provides a comprehensive description of how to make a MEMS based voltage reference. Two references, one for DC voltage and the other for AC voltage, were manufactured as well as the MEMS components for them. The components design and manufacturing, readout electronics and characterisation of the final devices are described. The focus is on the stability of the devices, which has so far been the major limiting factor exploiting commercial MEMS components in high end applications.</p> <p>The major achievement of this work was the improvement of the electrostatic stability of the AC voltage references to a level applicable in metrology. The innovations related to the stability improvement, as well as the new process developed for the components manufacturing, have general applicability in micromechanics. This work demonstrates that MEMS based voltage references can provide a competitive alternative to the conventional voltage references.</p>			
Keywords MEMS, micro electromechanical systems, DC voltage reference, AC voltage reference, electrostatic charging, pull-in voltage, long-term stability, micromachining			
ISBN 951-38-6859-1 (soft back ed.) 951-38-6860-5 (URL: http://www.vtt.fi/publications/index.jsp)			
Series title and ISSN VTT Publications 1235-0621 (soft back ed.) 1455-0849 (URL: http://www.vtt.fi/publications/index.jsp)			Project number
Date October 2006	Language English	Pages 109 p. + app. 42 p.	Price D
Name of project		Commissioned by	
Contact VTT Technical Research Centre of Finland Tietotie 3, P.O. Box 1000, FI-02044 VTT, Finland Phone internat. +358 20 722 111 Fax +358 20 722 7012		Sold by VTT Technical Research Centre of Finland P.O.Box 1000, FI-02044 VTT, Finland Phone internat. +358 20 722 4404 Fax +358 20 722 4374	

Tekijä(t)			
Nimeke MEMSiin perustuvat jännitereferenssit			
Tiivistelmä Mikroelektromeekaanisiin systeemeihin, eli MEMSiin, perustuvat jännitereferenssit ovat ainutlaatuisia sekä ominaisuuksiltaan että toimintaperiaatteeltaan. Ne ovat pieniä ja tarkkoja, ja niillä on hyvä hinta-laatusuhde. Referenssin toiminta perustuu mikromeekaanisesti valmistettuun levykondensaattoriin, jonka toinen levy on ripustettu piijousien varaan. Levyjen väliin kytketty jännite pyrkii lähentämään levyjä toisiinsa, kun taas piijousi vastustaa tätä liikettä. Voimatasapainoa levyjen välillä voidaan kuvata massa-jousi-vaimenninmallilla ja sillä on kaksi keskeistä ominaisuutta. Sähköstaattinen voima levyjen välillä on verrannollinen jännitteen neliöön, eli sitä voidaan käyttää todellisena tehollisarvomuuntimena. Lisäksi kondensaattorin ulostulojännitteellä on maksimi, jota voidaan käyttää stabiilina jännitereferenssinä, sillä sen arvo riippuu vain yksikiteisen piin materiaalivakiosta ja jousen geometriasta. Koska referenssijännite on samalla myös käänneaste, ohjauksijännitteen pienet vaihtelut eivät vaikuta referenssijännitteen arvoon ensimmäisessä kertaluvussa. Näiden ominaisuuksien ansiosta MEMS-jännitereferenssit tulevat haastamaan olemassa olevat jännitereferenssit, esimerkiksi Zenerdiodit. Väitöskirjassa tutkitaan sekä teoreettisesti että kokeellisesti kahta jännitereferenssiä, joista toinen on suunniteltu tasajännitteelle ja toinen vaihtojännitteelle. Molemmille suunniteltiin omat MEMS-komponentit. Niiden suunnittelu, valmistus ja ominaisuudet on kuvattu yksityiskohtaisesti samoin kuin referenssien lukuelektroniikat ja valmiiden laitteiden ominaisuudet. Erityisesti huomiota on kiinnitetty referenssien sähköiseen stabiilisuuteen, joka on myös nykyisin kaupallisessa tuotannossa olevien MEMS-komponenttien ongelma. Väitöstyön merkittävin saavutus on MEMS-komponenttien sähköisen stabiilisuuden parantaminen tasolle, joka mahdollistaa niiden hyödyntämisen vaativissa metrologisissa sovelluksissa. Näitä innovaatioita, samoin kuin työssä kehitettyä uutta valmistusmenetelmää, voidaan geneerisesti hyödyntää myös muihin MEMS-sovelluksiin.			
Avainsanat MEMS, micro electromechanical systems, DC voltage reference, AC voltage reference, electrostatic charging, pull-in voltage, long-term stability, micromachining			
ISBN 951-38-6859-1 (nid.) 951-38-6860-5 (URL: http://www.vtt.fi/publications/index.jsp)			
Avainnimeke ja ISSN VTT Publications 1235-0621 (nid.) 1455-0849 (URL: http://www.vtt.fi/publications/index.jsp)			Projektinumero
Julkaisu-aika Lokakuu 2006	Kieli Englanti, suom. tiiv.	Sivuja 109 s. + liitt. 42 s.	Hinta D
Projektin nimi		Toimeksiantaja(t)	
Yhteystiedot VTT Tietotie 3, PL 1000, 02044 VTT Puh. vaihde 020 722 111 Faksi 020 722 7012		Myynti VTT PL 1000, 02044 VTT Puh. 020 722 4404 Faksi 020 722 4374	

Voltage references based on MEMS, microelectromechanical systems, are unique in two different ways. First, they are small in size, stable, and cost-efficient. Second, the principle of operation of a MEMS voltage reference is outstanding from the physics point of view. They are electrical references, but their stability is based on material properties of single crystal silicon. Voltage references are fundamental building blocks in many electrical instruments like digital multimeters, data logging systems, and calibrators. MEMS components are manufactured using equipment and facilities developed for integrated circuit mass production, where a large number of components are processed on a single silicon wafer. Microsystem technology has enabled a new field in metrology.

This dissertation provides a comprehensive description of how to make a MEMS based voltage reference. Two references, one for DC voltage and the other for AC voltage, were manufactured as well as the MEMS components for them. The components design and manufacturing, readout electronics and characterisation of the final devices are described. The focus is on the stability of the devices, which has so far been the major limiting factor exploiting commercial MEMS components in high end applications.

The major achievement of this work was the improvement of the electrostatic stability of the AC voltage references to a level applicable in metrology. The innovations related to the stability improvement, as well as the new process developed for the components manufacturing, have general applicability in micromechanics. This work demonstrates that MEMS based voltage references can provide a competitive alternative to the conventional voltage references.

Tätä julkaisua myy

VTT
PL 1000
02044 VTT
Puh. 020 722 4404
Faksi 020 722 4374

Denna publikation säljs av

VTT
PB 1000
02044 VTT
Tel. 020 722 4404
Fax 020 722 4374

This publication is available from

VTT
P.O. Box 1000
FI-02044 VTT, Finland
Phone internat. +358 20 722 4404
Fax +358 20 722 4374
